UNIVERSITY OF CALIFORNIA

Santa Barbara

Miniaturizing Medicine – Strategies for Developing and Improving Point-Of-Care Biosensors

A dissertation submitted in partial satisfaction of the

requirements for the degree Doctor of Philosophy

in Materials

by

Nathan E. Ogden

Committee in charge:

Professor Kevin Plaxco, Co-Chair

Professor Craig Hawker, Co-Chair

Professor Omar Saleh

Professor Cyrus Safinya

December 2019

The dissertation of Nathan E. Ogden is approved.

_____
Omar Saleh

_____
Cyrus Safinya

_____
Craig Hawker, Co-Chair

_____
Kevin Plaxco, Co-Chair

December 2019

Miniaturizing Medicine – Strategies for Developing and Improving

Point-Of-Care Biosensors

ACKNOWLEDGEMENTS

I should begin by thanking my wonderful wife, Pritha. Besides being a lovely person, she has supported and enabled my otherwise crippling educational habit for these past six years and I am eternally grateful to her for that. I swear that I am going cold turkey after this. I would also like to thank my parents for their role in getting me hooked on education in the first place. If you think about it, this whole thing really is your fault. Last amongst my enablers, I would also like to thank Prof. Kevin Plaxco for taking me in when I was a cast-off graduate student. Thank you for taking a chance on me. I hope something good came of it.

There are also quite a few people who I would like to thank for their individual contributions. I would be remis if I did not mention Peter Mage for teaching me all about the fine art of microfluidics, which forms the foundation of the second chapter of this thesis. On that same project, I would also like to mention Dan Mamerow's contributions in testing various reagents and helping to run the experiments. Additionally, I would also like to thank Dr. Andrew Csordas for his role in teaching me about aptamers and for helping me develop (yet another) thrombin aptamer.

I would also like to thank everyone from the Plaxco lab for being a wonderfully entertaining and welcoming group of people to work with. I could not ask for better lab mates than y'all. There are a few people who deserve special mention here, however. Dr. Claudio Parolo was an early mentor for me and taught me all about how to make scaffold sensors. The third

chapter of this thesis would not have been possible if not for him. I'd also like to thank Dr. Martin Kurnik who, besides providing hours of conversation about science and obscure 70's and 80's musicians, was instrumental in teaching me everything I know about protein synthesis. If I ever need syphilis proteins ever again, you will be my first call. I'd also like to thank Dr. Alejandro Chamorro and Dr. (very soon to be Professor) Philippe Dauphin-Ducharme for allowing me to use their data to compare against my simulations. Lastly, I would like to thank Dr. Kyle Ploense for his assistance in performing *in-vivo* experiments. That material didn't make it into this thesis, unfortunately, but I appreciate it all the same. To anyone who's contributions I failed to mention, I am sorry. The fault lies not with you but rather with my terrible memory. To quote Bilbo Baggins "I don't know half of you half as well as I should like; and I like less than half of you half as well as you deserve."

VITA OF NATHAN E. OGDEN
November 2019

EDUCATION

UC Santa Barbara, Department of Materials Science — Santa Barbara, CA
Doctor of Philosophy in Materials Science

Rice University, Department of Physics and Astronomy — Houston, TX
Bachelor of Science in Applied Physics — May 2013

PUBLICATIONS

Ogden, N., Dauphin-Ducharme, P., Chamorro, A., Plaxco, K. (2019) "Towards the rational optimization of aptamers for electrochemical sensors" *(In preparation)*

Ogden, N., Kurnik, M., and Plaxco, K. (2019) "An electrochemical scaffold sensor for rapid syphilis diagnosis" *Analyst* 144.17

Parolo, C., Greenwood, A., **Ogden, N.**, Kang, D., Hawes, C., Arroyo-Curras, N., and Plaxco, K. (2019) "E-DNA scaffold sensors for the multiplexed detection of HIV-diagnostic antibodies in authentic patient samples" *Analytical Chemistry* (Submitted)

Arroyo-Curras, N., Sadeia, M., Ng, A., Fyodorova, Y., Williams, N., Afif, T., **Ogden, N.**, Andresen, R., Plaxco, K., and Lukeman, P. (2019) "An Electrochemical Biosensor Exploiting Conformational Changes in Electrode-Attached DNA Origami to Detect Hundred Nanometer-Scale Targets" *Angevandte Chemie,* (Submitted)

Kang, D., Parolo, C., Sun, S., **Ogden, N.**, Dahlquist, F., and Plaxco, K. (2018) "Expanding the Scope of Protein-Detecting Electrochemical DNA "Scaffold" Sensors*" ACS Sensors* 3.7

Haugan, H., Brown, G., Mahalingam, K., Grazulis, L., Now, G., **Ogden, N.**, and Kono, J. (2014) "Optimum growth window for InAs/GaInSb superlattice materials tailored for very long wavelength infrared detection" *Journal of Vacuum Science and Technology B* 32.2

Haugan, H., Brown, G., Elhamri, S., Mitchel W., Mahalingam K., Kim M., Noe G., **Ogden, N.**, and Kono, J. (2012) "Impact of Growth Temperature on InAs/GaInSb Strained Layer Superlattices for Very Long Wavelength Infrared Detection." *Applied Physics Letters* 101.17

Slaughter, L., Willingham, B., Chang, W., Chester, M., **Ogden, N.**, and Link, S. (2012) "Toward Plasmonic Polymers." *Nano Letters* 12.8

ABSTRACT

Miniaturizing Medicine – Strategies for Developing Point-Of-Care Biosensors

by

Nathan E. Ogden

Each moment of each day countless millions of proteins circulate through the body, performing their tasks, recognizing and binding to their targets, all with minimal crosstalk between the countless other proteins circulating alongside them. It is no wonder then, that, when faced with problems such as detecting rare molecular targets within complex backgrounds, technology developers often employ biological molecules as the foundation with which to build sensors ("biosensors") and develop processes ("bioassays"). But that is not to say that sensors and assays based on biorecognition are perfect. Bioassays, for example, are generally complex, time-consuming processes and thus they provide actionable information only after a significant time lag. Biosensors (such as blood glucose meters), in contrast, can provide real-time information, but those few that work in realistically complex sample matrices invariably rely on the specific chemical reactivity of their targets, greatly limiting the range of molecules they can detect. Motivated by these concerns, I have been exploring biosensors and bioassays that, unlike existing approaches, are simultaneously general and capable of rapidly returning answers.

The first strategy I have explored utilizes microfluidics to adapt existing, multi-step bioassays into a rapid-and-convenient point-of-care device. Specifically, taking advantage of the inherent automation potential of microfluidics I have shown it possible to automate and speed up an established, bench-top bioassay. Once fully automated, the assay can even be

used to perform continuous measurements, tracking changes in the concentration of a target protein in a clinical sample stream in real-time.

The second strategy that I explored was the development of a single-step, reagentless biosensor platform termed electrochemical DNA-based (E-DNA) sensors. This broad class of electrochemical sensors utilizes binding-induced changes in the structure or dynamics of an electrode-bound biomolecule to reagenltessly and continuously report on the concentration of its target. Specifically, this class of sensors uses DNA either as a scaffold upon which to display a recognition element (scaffold-sensors), such as an antigen, or as the recognition element itself (aptamer-based sensors). Using Monte-Carlo simulations I have examined how changing the molecular weight of a recognition element affects the performance of scaffold sensors and used this information to develop a point-of-care serological assay to help rapidly diagnose syphilis. Using a similar Monte-Carlo model I likewise optimized the performance of aptamer-based sensors by examining how modifications around the aptamer's binding pocket affect sensor performance. Together these studies are helping to bridge the gap between complex (but generalizable) bioassays and simple to use biosensors (such as blood glucose meters) which cannot readily be adapted to other targets.

TABLE OF CONTENTS

"All this science I don't understand,

It's just my job five days a week"

-Elton John

I. **Introduction**

Motivation

Biological recognition is incredibly powerful. Consider, for instance, the cytokine TNFα, an important signaling protein which is in part responsible for inducing cell death and initiating the body's inflammation response. While prompting cell death is at times essential for life, if TNFα was to bind to targets other than its intended ones, it would be disastrous. And yet TNFα performs its task day after day, year after year, in organisms all across the globe. And this is just one protein working amongst many thousands of others, each preforming its own task, binding to its own target with minimal cross-talk between them. It is no wonder then, that, when faced with problems such as detecting rare molecular targets within complex backgrounds, technology developers often employ biological molecules as the foundation with which to build sensors ("biosensors") and develop processes ("bioassays"). Whether it be measuring glucose in diabetic patients, measuring disease markers in plasma, or measuring the concentration of contaminants in food or beverages or soil or water, biological recognition plays an essential role in how we measure molecules in the modern world. That is not to say that sensors and assays based on biorecognition are perfect. Indeed, there remains much room for improvement and, as a result, it is these sorts of biosensors and bioassays which we will interest ourselves in this thesis.

Before discussing how to improve biosensors and bioassays (hereafter we will refer to the two interchangeably), it is worth asking what attributes comprise the ideal biosensor?

Arguably the most important is that a biosensor must have a low enough limit of detection to measure its target. In fact, a sensor which fails in this criterion really is no sensor at all. That is not to say, however, that the ability to measure small concentrations of target is the end all and be all of the ideal biosensor. It is easy to imagine cases where a sensor might be *too* sensitive to perform a useful function. Consider the example of a biosensor which works through the binding of a signaling protein to a target. The protein has some affinity towards its target, frequently given in terms of the dissociation constant, K_d. If we are in a situation where the amount of target is far in excess of the amount of the amount of affinity reagent (as is often the case in sensors where a limited amount of affinity reagent is conjugated to a surface), then we can think of the K_d as being the concentration of target at which half of our affinity reagents are bound. Clearly it is desirable that our hypothetical protein has a high affinity for its target (i.e., a low K_d), but only insofar as it relates to the expected amount of target present in our analyte. Too low of a K_d and we would completely saturate our sensor even at modest target concentrations, leaving it just as useless as a sensor with too high of a K_d, that does not appreciably bind its target. As a result, while many papers seek ways to push the limit of detection of their sensors, it is always worth keeping in mind that we should aim for a sensor which can perform measurements over a relevant dynamic range for a given target rather than necessarily pursuing sensitivity for its own sake.

If a properly matched dynamic range is the primary criteria for building a sensor, then selectivity is the second criteria that we should be concerned with. Consider, for instance, a non-biological based technique such as mass spectrometry. This is powerful analytic technique which allows researchers to measure picograms of material and can be used to

verify the purity of a sample and detect trace amounts of contaminants[1,2]. This ability to measure very low concentrations of target comes at a cost, however. Due to the sheer number of background molecules with overlapping signal, mass spectrometry is limited to measuring relatively pure samples. As a result, it must be paired with dilution, filtration, and generally some sort of purification, such as that achieved via gas chromatography, liquid chromatography, or capillary electrophoresis[3–5]. This makes it a fine research tool and an excellent quality control assay but leaves it poorly suited to clinical diagnostics where the expense and complication of purifying the sample oftentimes outweighs the benefits gained by high sensitivity. It is for this reason that biosensors are so attractive, since biological affinity reagents have already evolved to work in situ in the body, among the most complex of backgrounds. There are many ways to make far simpler sensors with a degree of specificity by introducing affinity reagents such as antibodies which attempt to sequester the target of interest. One example of such a sensor would be a micromechanical sensor in which an affinity reagent such as an antibody is immobilized on the surface of a cantilever[6–8]. Binding between the antibody and its target is then accompanied by a change in the weight of the cantilever. This, in turn, causes a change in the resonant frequency of the cantilever, which may be measured in order to quantify the amount of the target bound to the surface [Figure 1a]. A similar analogue with an electric readout would be a biologic field effect

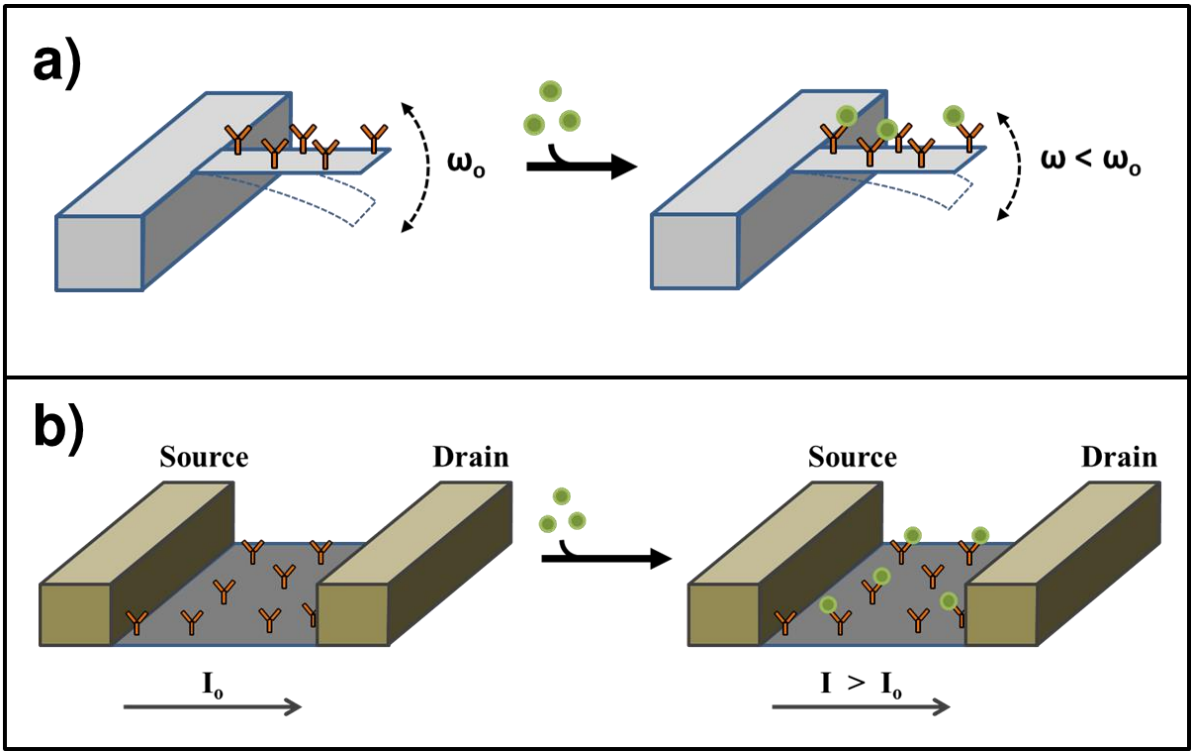

Figure 1 An illustration of two biosensing strategies relying on affinity reagents to sequester target. a) Microbalance sensors measure the resonant frequency of a lever which has been functionalized with an antibody (or other affinity reagent). The binding of target to the sensor changes the mass on the lever, which in turn changes the resonant frequency. b) A typical bio-FET sensor scheme in which a conductive source and drain are separated by a semiconductor which has been modified with an affinity reagent. Binding of the target modulates the resistance of the semiconductor, changing the amount of current which flows from the source to the drain.

transistor (bio-FET). Here affinity reagents are placed in the gate region of a field effect transistor and the binding of the target of interest modulates the resistance between the source and the drain [Figure 1b][9–11]. A fatal drawback with these sorts of sensors which rely entirely on adsorption to drive signal change is that while the presence of an affinity reagent enhances the likelihood of the target binding to the surface, it does not prevent non-specific binding. Since there is no way to discern the difference between off-target signal due to non-specific binding of biomolecules to the cantilever/transistor and signal due to the target, these sensors fail when challenged with realistically complex samples. This leaves them

unsuitable for deployment in complex media such as blood or serum since the sheer number of non-target proteins means that false signal due to unpredictable nonspecific binding events will outweigh the signal due to specific binding to the affinity reagent.

One method to avoid the problems described above is to co-opt proteins which can be adapted to generate a signal on their own rather than merely binding to its target. One of the most recognizable of such sensors is the blood glucose meter. First developed in 1962 [ref[12]], early glucose measuring devices used a colorimetric readout, but more modern blood glucose meters utilize an electrochemical readout which is simpler to use and provides a quantitative readout[13]. While there have been many advancements towards improving the reliability and accuracy of electrochemical blood glucose meters, they all have a similar method of operation[14–17]. Generally, a thin coating of glucose oxidase is applied to an electrode surface. The electrode is exposed to the analyte (typically blood drawn through a fingerpick) at which point the enzyme on the electrode surface reacts with glucose. Glucose oxidase is then re-oxidized by a mediator molecule, which generates a current which can be measured using a hand-held device. This current is proportional to the amount of enzyme being oxidized, which is in return proportional to the amount of glucose present in the blood. Since glucose oxidase is an enzyme which has already evolved to work in complex media, it is highly specific towards its target and there is negligible signal contribution from off target binding, despite the complexity of the analyte. The result is a biosensor highly specific to glucose which is small enough to fit in the palm of a patient's hand, rapid enough that a patient can immediately take corrective measures if the sensor indicates an adverse result,

and cheap enough that almost every diabetic patient in the United States owns one. In short, glucose monitors are everything that could be reasonably asked for in a biosensor.

If the blood glucose meter represents the ideal molecular sensor to which we strive, why then have we not seen similar biosensors for targets other than glucose? The answer lies within the enzyme that provides the signal transduction at the heart of the glucose sensor. We are extremely fortunate that glucose oxidase evolved the way that it did. If it were not for the convenient fact that glucose oxidase reacts with glucose in a fashion which can be detected electrochemically, then glucose monitors such as we know them would not work. Unfortunately, the list of enzymes which bind to a diagnostically relevant target and can be used to generate an electrochemically active product is incredibly short. Outside of a few niche cases, we are therefore limited to designing sensors around affinity reagents which bind to their targets but do not generate an electroactive product. The trick is then to find a way to link these binding events with a readout capable of discerning between bound and unbound reagents which does produce significant signal due to non-specific binding.

Given the challenge of creating a single-step sensor that can discern between specific and non-specific binding, it is far more common to develop complex and time-intensive procedures to perform the desired task. One of the most common assays of this sort is the enzyme linked immunosorbent assay (ELISA)[18]. As the name implies, ELISAs rely on naturally produced antibodies as their recognition element[19]. While there are many variants of ELISA assays, a representative scheme is shown in Figure 2. A technician will generally start by pipetting analyte into the wells of a 96 well plate which have been pre-coated with a

"capture" antibody. Depending on the concentration of target in the sample, some of it will bind to the capture antibody. After letting the sample incubate in the well for a pre-determined amount of time, the plate is washed and then a second "recognition" antibody is introduced. This antibody binds to whatever target has been immobilized by the capture antibody, forming a "sandwich." In some cases, the recognition antibody is labeled with an enzyme while in other cases a third, labeled, antibody is introduced which binds to the recognition antibody. In either case, the plate is washed again, and a fluorescent substrate is introduced which is catalyzed by the enzyme linked to one of the antibodies. This creates a colorimetric signal which can either be interpreted by eye or with the aid of a fluorescent plate reader. Since the immune system is naturally capable of generating antibodies against foreign bodies, it is possible to create antibodies against a wide variety of targets. The result is a sensitive and specific assay which is inherently much more generalizable than enzyme-based assays which only work in niche cases. Unfortunately, this comes at a cost. ELISAs are not easy to perform – they require a trained technician to carry out the steps of the assay. They are not quick – it can take hours of incubation time and multiple wash steps before reaching a result. Lastly, they are not portable – they require several sets of reagents (which often must be kept refrigerated) and the plate readers required to interpret the results are large and bulky. The combination of these drawbacks means that ELISAs and similar immunoassays are not performed at the point of care, but instead typically performed in specialize off-site labs. This introduces considerable delay between when a patient initially visits their doctor or caregiver and when they receive the results of the assay.

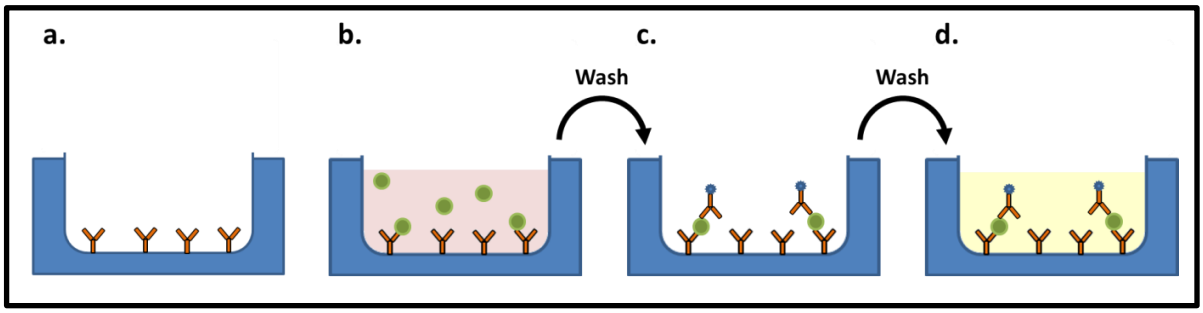

Figure 2 (a) In a typical ELISA, the wells of a microplate are coated with an antibody against the target of interest. (b) The analyte is then introduced into the well where it is allowed to incubate. The antigen eventually diffuses to the surface and binds to the antibodies coating the well. (c) The user then washes the plate and introduces a secondary antibody which forms a sandwich around the antigen. Typically this secondary antibody is either linked to an enzyme or a further enzyme linked antibody is introduced targeted towards the secondary antibody. (d) The plate is then washed again and a substrate is added which is converted by the enzyme to a fluorescent product. After allowing the sample to incubate for a set period of time, the reaction is halted and the fluorescence measured.

While the above should hardly be thought of as an exhaustive review of current biosensing strategies, it does illustrate the chief dynamic which hinders further progress in the field. There are a few commercially available point-of-care sensors, such as blood glucose meters or pulse oximeters, which fulfill all of the desired requirements for a biosensor, but they rely on specific chemistries or biomolecules which cannot be adapted to other targets. For the vast quantity of remaining targets, we are forced to rely on cumbersome assays which require a trained user to perform and can take hours to reach a result. While given enough time and resources we are currently capable of measuring almost any target in almost any analyte, there are many scenarios where both time and resources are scarce. The focus of this thesis will therefore be bridging the gap between generalizable but resource-intensive assays and niche-use but cheap, fast, and portable biosensors. We will show two approaches to solve this problem. This first, detailed in Chapter II, will be using microfluidics to adapt well-proven clinical assays to a point-of-care device. The second approach will be to

improve upon innovative electronic DNA based sensors, for which further background is given below.

Electrochemical DNA Based Sensors

In an attempt to combine the beneficial qualities of blood glucose meters, such as ease of use, rapid time to response, and small form factor, into a sensor that could be adapted to many different targets ranging from small molecules to proteins, of the Plaxco group began developing Electrochemical DNA sensors (E-DNA sensors). The first sensor in this class, published in 2003, was designed to recognize short segments of single stranded DNA or RNA[20] and was followed by several variants intended to improve on the original design[21–24]. The general method of operation for all of these sensors is that specific binding between the sensor and the target of interest changes the rate at which a redox reporter is capable of approaching the surface. For the early E-DNA sensors, a sequence that is complementary to the target sequence is modified on the 3' end with a thiol group and on the 5' end with a methylene blue molecule which serves as a redox reporter [Figure 3]. The complementary sequence is then bound to the surface of a gold electrode using a gold-thiol bond and the sensor surface is backfilled with a protective monolayer. The completed sensor can then be immersed in a solution containing the target strand. In the absence of the target sequence, the tethered DNA is flexible, and the redox reporter is able to freely approach the surface. When the electrode is interrogated with a technique such as square wave voltammetry, the redox reporter produces a measurable Faradic current. In the presence of the target sequence, however, the target and its complement form a double stranded sequence which is far more ridged than the single stranded DNA alone. This has the effect of reducing the frequency

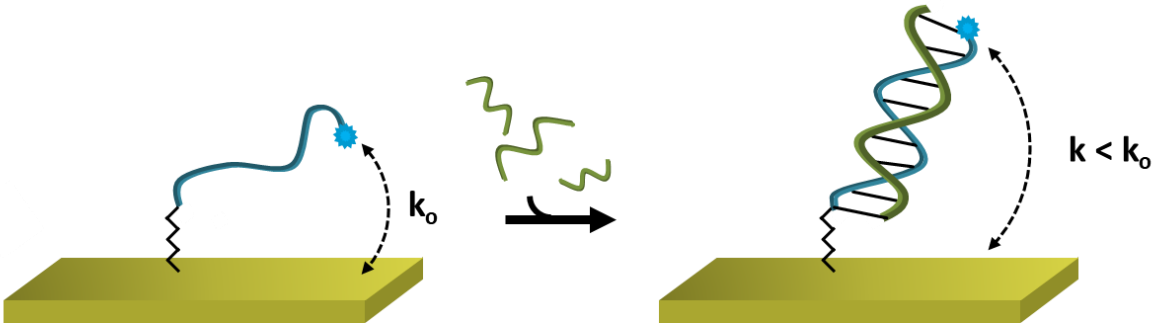

Figure 3 While there are many variants**,** in the simplest example of an E-DNA sensor, a methylene blue redox reporter modified DNA sequence is attached to an electrode surface. Due to the flexibility of single stranded DNA, the redox reporter is able to move relatively freely in the unbound state, leading to a high electron transfer rate between the reporter and the surface. When the complementary DNA strand binds to the reporter strand, it forms a double stranded DNA complex which is far more ridged, leading to a lower electron transfer rate.

with which the redox reporter is able to approach the surface, therefore reducing the measured Faradic current measured in a manner proportional to the concentration of the target DNA sequence. Because the signal change is driven by the conformational change arising from the binding of the recognition strand to its complement (as opposed to the binding of a molecule to the surface), the technique is highly specific as demonstrated by its use in blood serum, saliva, and cellular extract[22].

Electrochemical Aptamer-Based Sensors

While the original E-DNA sensors could be modified to recognize effectively any nucleic acid sequence, single stranded oligonucleotides represent only a tiny fraction of the space of interesting biosensing targets. A major set forward for E-DNA sensors was therefore the development of electrochemical aptamer-based (E-AB) sensors. Aptamers are short oligonucleotide sequences which bind selectively to a target and were discovered independently by two different groups in 1990 [ref[25,26]]. While we typically think of nucleic

acids as storing or transmitting genetic information, aptamers are functional molecules and are not found in naturally. Instead, they are purposefully developed in a laboratory setting, typically through some variation of a process known as systematic evolution of ligands by exponential enrichment (SELEX). In this process, a large library of randomly generated nucleotide sequences, typically containing on the order of 10^{15} sequences, is exposed to a target of interest, generally immobilized on some sort of solid support. While the vast majority of sequences will not bind to the target, a small fraction will. These sequences can be isolated, usually through the means of sequential washing steps, and then enriched through polymerase chain reaction. The result is a subset of the library of sequences that is biased towards sequences that bind the target. Through repeating this process several times, it is possible to narrow the initial library of trillions of sequences down to the handful of sequences capable of binding the target. These can then be individually characterized in order to find the best sequence, whether that be the one with the lowest K_d, the most selective sequence, or some combination thereof. Since aptamers are short, single stranded, oligonucleotide sequences which selectively bind to a target it is fairly straightforward to adapt them to the E-DNA platform, as first demonstrated by Xiao et al. in 2005 [ref[27]]. Subsequent publications have shown that this method is quite generalizable, with examples of E-AB sensors being used to detect targets ranging from small molecule drugs to proteins[28–31]. As with previous E-DNA sensors, E-AB sensors are resistant to spurious signals due to off-target binding because the signal change is driven by conformational changes of the aptamer upon binding to its target rather than the simple process of a molecule binding to the surface itself. Thus, not only have E-AB sensors been used in complex media, but recently they have been adapted for use in implantable sensors used to

take measurements *in vivo*[32,33]. Still, while adapting aptamers for use in E-AB sensors initially sounds trivial, this is not always the case. Often researchers find that aptamers which have been demonstrated to work well in solution perform poorly when attached to the surface of an electrode. In these cases, it becomes necessary for the researcher to make modifications to the aptamer sequence, a process which can devolve into a trial and error affair. Efforts to improve this process are described in Chapter IV.

DNA Scaffold Sensors

The last class of sensors which we will discuss in this thesis are DNA scaffold sensors. While there have been many efforts to identify aptamers for clinically useful targets, the field suffers from two key problems. First, since aptamers were only first described in the 1990's and remained a niche topic for some time after, there has been relatively little time to develop aptamers compared to the amount of time and effort which has been expended towards identifying and characterizing other biomolecules, whether that be the development of antibodies for various targets, or the identification of binding epitopes for those antibodies. The second problem facing the aptamer field is that DNA (and RNA) present a limited chemical library from which to create an affinity reagent as compared to proteins. While there have been some attempts to rectify this through the use of non-natural bases[34–37] the end result is that aptamers for some targets remain stubbornly elusive. Either it is impossible to find aptamers against them, or the aptamers are of such poor affinity that they are not practically useful for creating sensors. To circumvent this issue, the Plaxco group developed a new class of sensors known as scaffold sensors[38–40]. Instead of relying on aptamers as the recognition element, scaffold sensors are capable of displaying peptides or

small proteins as the recognition element, vastly expanding the space of measurable targets. As with the rest of the E-DNA sensors, scaffold sensors start as a single stranded, methylene blue modified, DNA sequence bound to the surface of a gold electrode. For scaffold sensors, however, this initial "anchor" strand is then bound to a complementary peptide nucleic acid sequence which then displays a short peptide epitope. Binding of a target to the epitope changes the rate of electron transfer between the methylene blue and the surface, generating a measurable signal change [Figure 4]. A further examination of the physics of these sensors as well as a demonstration of their practical utility as a diagnostic device is demonstrated in Chapter III.

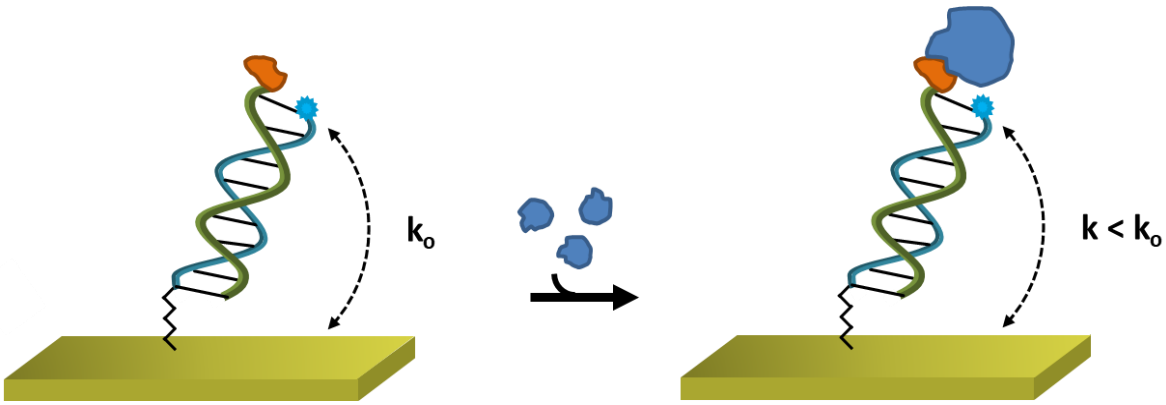

Figure 4 The recognition element of a scaffold sensor consists of a methylene blue modified anchor strand bound to the surface of an electrode. A complementary strand bearing either a short peptide or a small protein is conjugated to a complementary strand which then binds to the anchor. Binding of the target protein to the peptide reduces the efficiency with which the redox reporter is able to approach the surface, thus lowering the electron transfer rate of the sensor

References

(1) Lesur, A.; Domon, B. Advances in High-Resolution Accurate Mass Spectrometry Application to Targeted Proteomics. *PROTEOMICS* **2015**, *15* (5–6), 880–890.

(2) Smits, A. H.; Vermeulen, M. Characterizing Protein–Protein Interactions Using Mass Spectrometry: Challenges and Opportunities. *Trends in Biotechnology* **2016**, *34* (10), 825–834.

(3) Loos, G.; Van Schepdael, A.; Cabooter, D. Quantitative Mass Spectrometry Methods for Pharmaceutical Analysis. *Philos Trans A Math Phys Eng Sci* **2016**, *374* (2079).

(4) Dittrich, J.; Becker, S.; Hecht, M.; Ceglarek, U. Sample Preparation Strategies for Targeted Proteomics via Proteotypic Peptides in Human Blood Using Liquid Chromatography Tandem Mass Spectrometry. *PROTEOMICS – Clinical Applications* **2015**, *9* (1–2), 5–16.

(5) Klepárník, K. Recent Advances in Combination of Capillary Electrophoresis with Mass Spectrometry: Methodology and Theory. *ELECTROPHORESIS* **2015**, *36* (1), 159–178.

(6) Arlett, J. L.; Myers, E. B.; Roukes, M. L. Comparative Advantages of Mechanical Biosensors. *Nature Nanotech* **2011**, *6* (4), 203–215.

(7) Boisen, A.; Dohn, S.; Keller, S. S.; Schmid, S.; Tenje, M. Cantilever-like Micromechanical Sensors. *Rep. Prog. Phys.* **2011**, *74* (3), 036101.

(8) Raiteri, R.; Grattarola, M.; Butt, H.-J.; Skládal, P. Micromechanical Cantilever-Based Biosensors. *Sensors and Actuators B: Chemical* **2001**, *79* (2), 115–126.

(9) Schöning, M. J.; Poghossian, A. Bio FEDs (Field-Effect Devices): State-of-the-Art and New Directions. *Electroanalysis* **2006**, *18* (19–20), 1893–1900.

(10) Formisano, N.; Bhalla, N.; Heeran, M.; Reyes Martinez, J.; Sarkar, A.; Laabei, M.; Jolly, P.; Bowen, C. R.; Taylor, J. T.; Flitsch, S.; et al. Inexpensive and Fast Pathogenic Bacteria Screening Using Field-Effect Transistors. *Biosensors and Bioelectronics* **2016**, *85*, 103–109.

(11) Nakatsuka, N.; Yang, K.-A.; Abendroth, J. M.; Cheung, K. M.; Xu, X.; Yang, H.; Zhao, C.; Zhu, B.; Rim, Y. S.; Yang, Y.; et al. Aptamer–Field-Effect Transistors Overcome Debye Length Limitations for Small-Molecule Sensing. *Science* **2018**, *362* (6412), 319–

(12) Clark, L. C.; Lyons, C. Electrode Systems for Continuous Monitoring in Cardiovascular Surgery. *Annals of the New York Academy of Sciences* **1962**, *102* (1), 29–45.

(13) Updike, S. J.; Hicks, G. P. The Enzyme Electrode. *Nature* **1967**, *214* (5092), 986–988.

(14) Yoo, E.-H.; Lee, S.-Y. Glucose Biosensors: An Overview of Use in Clinical Practice. *Sensors (Basel)* **2010**, *10* (5), 4558–4576.

(15) Heller, A.; Feldman, B. Electrochemical Glucose Sensors and Their Applications in Diabetes Management. *Chem. Rev.* **2008**, *108* (7), 2482–2505.

(16) Cass, A. E.; Davis, G.; Francis, G. D.; Hill, H. A.; Aston, W. J.; Higgins, I. J.; Plotkin, E. V.; Scott, L. D.; Turner, A. P. Ferrocene-Mediated Enzyme Electrode for Amperometric Determination of Glucose. *Anal. Chem.* **1984**, *56* (4), 667–671.

(17) Turner, A. P.; Chen, B.; Piletsky, S. A. In Vitro Diagnostics in Diabetes: Meeting the Challenge. *Clin. Chem.* **1999**, *45* (9), 1596–1601.

(18) Lazcka, O.; Campo, F. J. D.; Muñoz, F. X. Pathogen Detection: A Perspective of Traditional Methods and Biosensors. *Biosensors and Bioelectronics* **2007**, *22* (7), 1205–1217.

(19) Engvall, E.; Perlmann, P. Enzyme-Linked Immunosorbent Assay (ELISA) Quantitative Assay of Immunoglobulin G. *Immunochemistry* **1971**, *8* (9), 871–874.

(20) Fan, C.; Plaxco, K. W.; Heeger, A. J. Electrochemical Interrogation of Conformational Changes as a Reagentless Method for the Sequence-Specific Detection of DNA. *Proc. Natl. Acad. Sci. U.S.A.* **2003**, *100* (16), 9134–9137.

(21) Xiao, Y.; Lubin, A. A.; Baker, B. R.; Plaxco, K. W.; Heeger, A. J. Single-Step Electronic Detection of Femtomolar DNA by Target-Induced Strand Displacement in an Electrode-Bound Duplex. *Proc. Natl. Acad. Sci. U.S.A.* **2006**, *103* (45), 16677–16680.

(22) Lubin, A. A.; Lai, R. Y.; Baker, B. R.; Heeger, A. J.; Plaxco, K. W. Sequence-Specific, Electronic Detection of Oligonucleotides in Blood, Soil, and Foodstuffs with the Reagentless, Reusable E-DNA Sensor. *Anal. Chem.* **2006**, *78* (16), 5671–5677.

(23) Liu, G.; Wan, Y.; Gau, V.; Zhang, J.; Wang, L.; Song, S.; Fan, C. An Enzyme-Based E-DNA Sensor for Sequence-Specific Detection of Femtomolar DNA Targets. *J. Am. Chem. Soc.* **2008**, *130* (21), 6820–6825.

(24) Lai, R. Y.; Lagally, E. T.; Lee, S.-H.; Soh, H. T.; Plaxco, K. W.; Heeger, A. J. Rapid, Sequence-Specific Detection of Unpurified PCR Amplicons via a Reusable, Electrochemical Sensor. *PNAS* **2006**, *103* (11), 4017–4021.

(25) Tuerk, C.; Gold, L. Systematic Evolution of Ligands by Exponential Enrichment: RNA Ligands to Bacteriophage T4 DNA Polymerase. *Science* **1990**, *249* (4968), 505–510.

(26) Ellington, A. D.; Szostak, J. W. In Vitro Selection of RNA Molecules That Bind Specific Ligands. *Nature* **1990**, *346* (6287), 818–822.

(27) Xiao, Y.; Lubin, A. A.; Heeger, A. J.; Plaxco, K. W. Label-Free Electronic Detection of Thrombin in Blood Serum by Using an Aptamer-Based Sensor. *Angew. Chem. Int. Ed. Engl.* **2005**, *44* (34), 5456–5459.

(28) Xiao, Y.; Piorek, B. D.; Plaxco, K. W.; Heeger, A. J. A Reagentless Signal-On Architecture for Electronic, Aptamer-Based Sensors via Target-Induced Strand Displacement. *J. Am. Chem. Soc.* **2005**, *127* (51), 17990–17991.

(29) Baker, B. R.; Lai, R. Y.; Wood, M. S.; Doctor, E. H.; Heeger, A. J.; Plaxco, K. W. An Electronic, Aptamer-Based Small-Molecule Sensor for the Rapid, Label-Free Detection of Cocaine in Adulterated Samples and Biological Fluids. *J. Am. Chem. Soc.* **2006**, *128* (10), 3138–3139.

(30) Lai, R. Y.; Plaxco, K. W.; Heeger, A. J. Aptamer-Based Electrochemical Detection of Picomolar Platelet-Derived Growth Factor Directly in Blood Serum. *Anal. Chem.* **2007**, *79* (1), 229–233.

(31) Rowe, A. A.; Miller, E. A.; Plaxco, K. W. Reagentless Measurement of Aminoglycoside Antibiotics in Blood Serum via an Electrochemical, Ribonucleic Acid Aptamer-Based Biosensor. *Anal. Chem.* **2010**, *82* (17), 7090–7095.

(32) Ferguson, B. S.; Hoggarth, D. A.; Maliniak, D.; Ploense, K.; White, R. J.; Woodward, N.; Hsieh, K.; Bonham, A. J.; Eisenstein, M.; Kippin, T. E.; et al. Real-Time, Aptamer-Based Tracking of Circulating Therapeutic Agents in Living Animals. *Science Translational Medicine* **2013**, *5* (213),

(33) Arroyo-Currás, N.; Somerson, J.; Vieira, P. A.; Ploense, K. L.; Kippin, T. E.; Plaxco, K. W. Real-Time Measurement of Small Molecules Directly in Awake, Ambulatory Animals. *PNAS* **2017**, *114* (4), 645–650.

(34) Kuwahara, M. Progress in Chemically Modified Nucleic Acid Aptamers. In *Chemical Biology of Nucleic Acids: Fundamentals and Clinical Applications*; Erdmann, V. A., Markiewicz, W. T., Barciszewski, J., Eds.; RNA Technologies; Springer: Berlin, Heidelberg, 2014; pp 243–270.

(35) Mei, H.; Liao, J.-Y.; Jimenez, R. M.; Wang, Y.; Bala, S.; McCloskey, C.; Switzer, C.; Chaput, J. C. Synthesis and Evolution of a Threose Nucleic Acid Aptamer Bearing 7-Deaza-7-Substituted Guanosine Residues. *J. Am. Chem. Soc.* **2018**, *140* (17), 5706–5713.

(36) Rangel, A. E.; Chen, Z.; Ayele, T. M.; Heemstra, J. M. In Vitro Selection of an XNA Aptamer Capable of Small-Molecule Recognition. *Nucleic Acids Res* **2018**, *46* (16), 8057–

(37) Kasahara, Y.; Irisawa, Y.; Ozaki, H.; Obika, S.; Kuwahara, M. 2′,4′-BNA/LNA Aptamers: CE-SELEX Using a DNA-Based Library of Full-Length 2′-O,4′-C-Methylene-Bridged/Linked Bicyclic Ribonucleotides. *Bioorganic & Medicinal Chemistry Letters* **2013**, *23* (5), 1288–1292.

(38) Cash, K. J.; Ricci, F.; Plaxco, K. W. An Electrochemical Sensor for the Detection of Protein−Small Molecule Interactions Directly in Serum and Other Complex Matrices. *Journal of the American Chemical Society* **2009**, *131* (20), 6955–6957.

(39) Cash, K. J.; Ricci, F.; Plaxco, K. W. A General Electrochemical Method for Label-Free Screening of Protein–Small Molecule Interactions. *Chemical Communications* **2009**, No. 41, 6222.

(40) Bonham, A. J.; Paden, N. G.; Ricci, F.; Plaxco, K. W. Detection of IP-10 Protein Marker in Undiluted Blood Serum via an Electrochemical E-DNA Scaffold Sensor. *The Analyst* **2013**, *138* (19), 5580.

II. Continuous, real-time microfluidic immunoassay

Introduction

In this chapter we discuss the development of a novel device designed to circumvent the shortcomings of traditional bioassays by taking advantage of the inherent automation potential of microfluidics. Given the massive dynamic range of the human proteome, a great deal of effort has been placed into increasing the sensitivity of modern affinity reagent based biosensors [1–3]. Lowering the limit of detection allows researchers to gain insight into the concentration of low abundance proteins, and aids in the search for biomarkers which can signal disease [4]. The common drawback of these sensors, however, is that they are purely end-point measurements. They rely on techniques that take trained users several hours to carry out and, as a result, they offer little insight into how protein concentrations may change as a function of time. Nevertheless, there are many serious conditions which could be detected, and therefore treated, more effectively if, rather than focusing purely on lowering the limit of detection, we could instead measure changes in a reporter protein's concentration in real-time. Disseminated intravascular coagulation (DIC), for instance, is a condition whose effects are characterized by widespread activation of the coagulation pathway, leading to clot formation, followed by organ failure, and eventually death[5]. Typically, this happens in patients already compromised by some other serious condition and, as a result, leads to a high mortality rate. Nevertheless, there is not currently any single laboratory test designed to diagnose DIC. Doctors are instead forced to form a diagnosis based off a scoring system which assigns point values to various physical symptoms[6]. By continuously measuring the concentration of one (or several) of the proteins involved in the

coagulation cascade, care-givers would be able to administer treatment earlier and, thus, lower the risk of fatal complications.

Recent years have seen some success in measuring protein concentration as a function of time in buffer and dilute serum using electrochemical[7,8] and optical[9] means. Unfortunately, nonspecific adsorption of proteins and cells from whole blood onto sensor surfaces leads to rapid signal degradation in many of these approaches[10]. Meanwhile, the poor optical qualities of whole blood and blood serum likewise renders fluorescent detection problematic[11,12]. As a result, many otherwise promising strategies for continuous protein monitoring are ill suited for clinical use. By combining the processing steps, washing steps, and measurement steps of a traditional immunoassay onto a single device capable of continuous readout, we can track the change of concentration of a sample protein in whole blood in real-time while avoiding many of the pitfalls which limit current techniques.

The most interesting proteins to measure in real-time would be those involved in the coagulation cascade since their concentration can change several orders of magnitude in a short span of time and the resulting changes have obvious clinical importance. As an initial proof of concept however, we have used our device to measure *in vitro* concentrations of the cytokine protein tumor necrosis factor alpha (TNFα). We chose TNFα as a preliminary target for two reasons: first, there exists a set of affinity reagents capable of forming a sandwich complex, one reagent being a monoclonal antibody and the other being a recently discovered DNA aptamer selected for its specificity in serum[13]. Second, while TNFα is naturally present in the blood stream, it typically exists at sub-picomolar concentrations[14,15],

allowing us to dope unmodified whole blood with nanomolar to micromolar concentrations of protein without having to worry about signifigant background signal arising from the protein naturally present.

Theoretical Background

Motivating Microfluidics

In order to adapt an existing benchtop assay to a point-of-care device, we will leverage microfluidics to fully automate all of the sample processing steps. This removes the need for trained technicians to operate the assay as well as removing the need for specialized lab space to analyze patient samples. The combined effect is that we can shift care from centralized lab facilities to the point of care itself, resulting in minimal lag time between when a care giver takes a sample and when the results of whatever assay being run is returned. It is worthwhile, therefore, to spend some time discussing the theoretical background of microfluidics in greater detail. What, for example, defines microfluidics as opposed to "macro"-fluidics? Besides the obvious advantage of handling small samples sizes, what advantages does microfluidics confer over a larger system? And finally, how can we adapt the steps of a traditional benchtop assay, such as the mixing and separating reagents, to a fully automated system?

Defining Microfluidics

The simplest definition of "microfluidics" would be any fluidic device which holds microliter volumes of reagents. This definition, however, does little to communicate the physical properties which set microfluidics apart from any other regime of fluid mechanics. In order to understand the physics of microfluidics, we can first start with the Navier-Stokes equation, which arises from Newton's second law of motion as applied to fluids and describes the velocity field of a Newtonian fluid as it is acted upon by a set of forces such as shear forces and pressure differentials:

$$\rho \frac{\partial \vec{u}}{\partial t} = \nabla \vec{\sigma} + \vec{\mathrm{f}} = -\nabla \mathrm{p} + \eta \nabla^2 \vec{\mathrm{u}} + \vec{\mathrm{f}}$$

Here ρ is the density of the fluid, u is the velocity $\vec{\sigma}$ represents the force per unit area exerted by surfaces, f represents body forces (i.e. forces which are exerted on the entirety of the fluid), and η is the shear viscosity. While the Navier-Stokes equation is capable of fully describing any arbitrary fluid system, it lacks an analytic solution outside of a few specialized cases. As a result, while highly useful for numerical simulations, it provides little intuition into the behavior of a system. If we wish to gain an understanding of the behavior of some arbitrary system without resorting to highly detailed numerical modeling (we do), then it becomes useful to instead define dimensionless parameters which can capture a snapshot of the behavior of a system without requiring extensive calculations.

The parameter most associated with microfluidics is the Reynolds number[16–18]. This dimensionless parameter describes the ratio between the inertial and viscous forces on a fluid:

$$Re = \frac{\rho U_o L_o}{\eta}$$

where U_o is an average characteristic velocity of the system, L_o is a characteristic length, and as above ρ is the density of the fluid and η is the shear viscosity. In our typical day-to-day experience, we are accustomed to fluidic systems dominated by inertial effects ($Re > 1$). Examples of such systems would be water flowing through large diameter pipes, rivers, streams, or virtually any other fluid system which we interact with on a day-to-day basis. In such systems, we expect that inertia will cause a fluid in motion will stay in motion while turbulence will randomly mix and disrupt the flow in a chaotic fashion. Microfluidics,

conversely, can be thought of as the regime where this no longer holds true. If the characteristic length scale is small enough relative to the fluid viscosity to where the Reynolds number is much less than 1, then the behavior of the system changes completely[19]. In this regime, the behavior of the system is entirely dominated by forces currently acting on the system – either viscous forces or pressure differentials actively pumping liquid through the channel. Instead of the turbulent mixing flow which we are accustomed to, here instead we see completely laminar flow. As a result, flow through the system is (almost) completely reversible. The only mixing which takes place is through diffusion, a process which typically takes orders of magnitude longer than turbulent mixing.

Advantages of Microfluidics

Now that we have defined what constitutes the microfluidic regime, the next question is why we should care. What advantages does being in a system dominated by viscous forces confer? The answer to this question is control. Because we do not have to worry about turbulent mixing, it is possible to exert a great deal of control over our system. For example, rather than attempting to solve the Navier-Stokes equation for a system, it is possible to reduce the problem to something analogous to Kirchhoff's circuit laws for electronics[20]. We can convert the traditional circuit equation

$$\Delta V = IR$$

where ΔV is the voltage differential across a circuit, I is the current and R is the resistance, to an analogous "microfluidic circuit" equation:

$$\Delta P = QR_h$$

where ΔP is the pressure differential, Q is the flow rate, and R_h is the hydrodynamic resistance, which can be calculated based off the channel geometry as well as the fluid viscosity. Using this technique, it is possible to create microfluidic "circuits" with complex junctions where, instead of attempting to numerically solve the Navier-Stokes equation, the user can instead calculate approximate behavior. As one example, microfluidics have been used to create highly reproducible droplet generators[21–24]. These devices typically take the form of a four-way junction where one inlet contains a reagent and two perpendicular inlets contain a non-miscible liquid such as mineral oil. At the junction, droplets are created as the reagent stream is encapsulated by the oil streams. Each droplet can be used as a mini-reaction chamber where the amount of reagents introduced as well as the amount of time the reaction is allowed to take place can be passively controlled by the design of the mixer itself[25]. Because there is no turbulence and all of the flow parameters satisfy Kirchhoff's laws, the entire process is inherently automated and reproducible.

It is also possible to take advantage of Kirchhoff's laws in order to sort particles inside of microfluidic chambers. If we create a microfluidic junction where two smaller channels split off of a main channel, it is easy to calculate the flow rate through each of the smaller channels and, since flow through microfluidic systems is laminar, it is trivial to predict which outlet a particle traveling in the main channel will exit towards. Particle sorters such as this have been shown to work in microfluidic chambers via magnetophoresis, acoustophoresis, electrophoresis, or other techniques[26–28]. For more complex devices, it is also possible to create microfluidic valves to further control flow and to isolate reagents from one another until some pre-determined time[29].

Adapting Benchtop Assays

As discussed above, microfluidics is a powerful tool for controlling the behavior of fluids (and particles suspended in those fluids). It is not too difficult to imagine how it would be possible to take advantage of this fact to adapt a benchtop assay to a single "lab-on-a-chip" device. If we consider the example of a user wishing to perform an immunoassay on some sort of solid support, the user would likely perform the following steps:

1. Mix the solid support (with some sort of capture reagent conjugated to the surface) with the sample
2. Wash
3. Mix in a labeled reagent
4. Wash
5. Measure the resulting signal

Since microfluidics gives us a great deal of control over the behavior of our system and we do not have to worry about turbulent mixing, it is easy to imagine a device which breaks this process down into a few discrete chambers, each performing their allotted task in sequence. The only major issue we can expect is with the mixing steps. Almost any assay will require some set of reagents to be mixed together at some point during the process. As previously discussed, however, the very thing that characterizes microfluidics is that there is no turbulent mixing inside of a microfluidic channel. In order to automate an assay, it is therefore necessary to somehow disrupt the laminar flow. Luckily, this problem has already

been solved by the Whitesides group amongst others[30,31]. By introducing a series of raised herringbone patterns decorating one side of a microfluidic channel, they were able to locally disrupt laminar flow through the chamber, allowing them to mix two inlets much more efficiently than by relying on diffusion alone. This gives us the last component necessary to automate an assay. We can now easily imagine a device where reagents on a solid support are introduced, mixed with the sample, allowed to incubate, and then sorted out of the sample into a washing buffer where they can be analyzed.

Results

Device Design

Our goal is to take full advantage of microfluidics in order to create a chip which can passively automate a complex assay. In this specific case, we have designed a device which utilizes magnetic microbeads as a solid support for performing an on-chip fluorescence-based sandwich assay. The setup is shown in Figure 1a. To summarize, fluid from the sample inlet is continuously mixed with a reagent mixture containing antibody-functionalized beads and a phycoerythrin (PE) dye labeled affinity reagent. The resulting mixture incubates on chip inside the mixing stage, forming a sandwich complex with the target protein on the surface of the magnetic beads. It should be noted that the incubation/mixing stage of the device is not long enough for the antibody-modified microbeads to reach equilibrium with their surroundings (barring some unrealistically slow

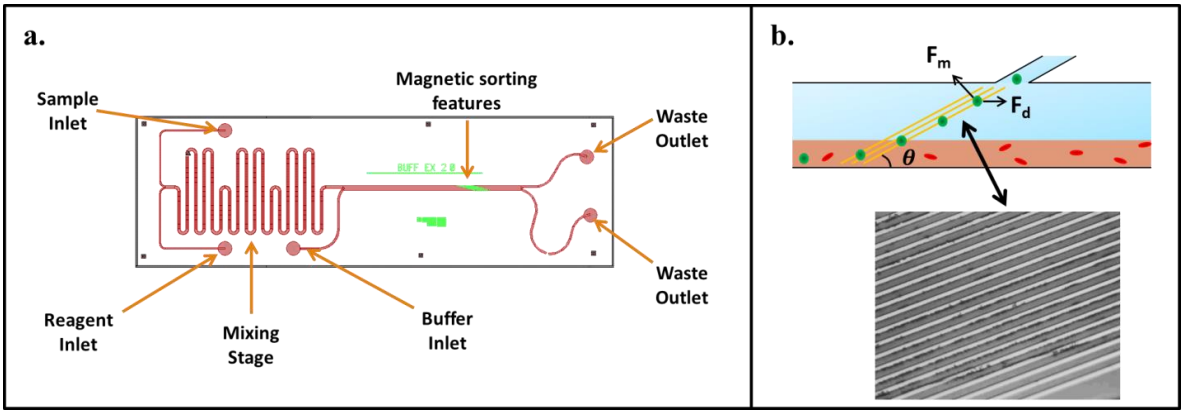

Figure 5. (a) A schematic showing the major features of the real time immunoassay chip. The sample and reagents are introduced at the appropriate inlets on the left side of the device where they then flow through a mixing stage. After mixing and incubation, we use a buffer suitable for fluorescent imaging to push the sample/reagent mixture to the top of the channel. Microfabricated nickel strips then pull the magnetic beads from the sample mixture into the imaging buffer where their fluorescence can be measured. We utilize two waste outlets so that the results can be verified on a flow cytometer after collection. (b) We use microfabricated nickel strips to divert paramagnetic beads from the sample solution into an imaging buffer. When placed on top of a neodymium magnet, the nickel strips create a strong, localized magnetic field. This, in turn, causes a force normal to the direction of the strips to divert beads from one buffer to another.

flow rate). Rather, we are taking advantage of the highly reproducible flow behavior inside microfluidic channels to ensure that the beads are all exposed to the sample for the same amount of time. After leaving the mixing stage, a buffer inlet forces the blood/reagent mixture to one side of the microfluidic channel. Due to the laminar nature of microfluidic flow, there is minimal mixing between the optically clear buffer and the sample mixture. The sample then passes over a number of microfabricated ferromagnetic strips (MFS). These are nickel strips 10 μm wide which have been deposited onto the glass backing wafer and run at an angle relative to the channel. When placed onto a permanent magnet, such as a neodymium magnet, the nickel strips create a large, localized magnetic field[32–34]. We can take advantage of this to displace the magnetic beads into an optically favorable buffer for analysis. While similar "buffer exchange" devices have been used to perform end-point measurements [35–38], our device is unique in that we use kinked MFS to deflect and temporarily trap the magnetic beads [Figure 1b]. The physics of this temporary trapping are relatively straightforward. If we consider a spherical particle traveling in a microfluidic device, there is typically only one force we need consider, that of the fluidic drag:

$$\overrightarrow{F_d} = 6\pi\eta r(\overrightarrow{v_f} - \overrightarrow{v_p})$$

where $\overrightarrow{F_d}$ is the drag force, η is the fluid viscosity, r is the radius of a spherical particle, $\overrightarrow{v_f}$ is the fluid velocity and $\overrightarrow{v_p}$ is the velocity of the particle. We see that a particle traveling in a microfluidic device will accelerate until it reaches the same velocity as the surrounding medium after which there will be no further net force. Upon reaching the MFS, however, there will be a counteracting magnetic force:

$$\overrightarrow{F_m} = m\nabla\vec{\mathrm{B}} = \frac{4\pi}{3}Mr^3\nabla\vec{B}$$

where m is the magnetic moment of the particle, $\nabla\vec{B}$ is the magnetic field gradient, M is the magnetization, and r is again the radius of the particle. We see from this that the magnetic force will act perpendicular to the MFS strips. If the strips are at some angle (θ) relative to the flow in the device, a magnetic particle will therefore be deflected out of its path and move along the MFS as long as

$$|F_m| > |F_d|\sin(\theta)$$

We can take advantage of this to separate the (now fluorescently labeled) magnetic beads from the optically unfavorable blood/reagent mixture. In order to image the particles, however, we must stop or slow them down long enough to accurately measure their brightness. Here again we can use the MFS structures. By placing a kink at the end of the strips perpendicular to the direction of the flow, we now have a situation where the particles will be trapped so long as

$$|F_m| > |F_d|$$

$$\frac{4\pi}{3} M r^3 \nabla\vec{B} > 6\pi\eta r\overrightarrow{v_f}$$

Since the magnetic field is highly localized, only particles near the nickel strips themselves will feel the effects of the magnetic field. As more and more particles build up behind the trapped beads, however, the drag force acting on the clog will continue to increase linearly with the size of the clog. The net effect of these two phenomena is that small clusters of beads will become temporarily trapped by the magnetic force counteracting the drag force. Eventually, depending on the flow rate inside the device, the buildup of particles behind the trapped beads will result in the drag force being greater than the magnetic force, pushing the entire cluster past the strips. We can take advantage of these kinked-MFS strips to "pause" a cluster of beads in place long enough to accurately image them with a CCD camera before

releasing them and refreshing the beads in the frame. As the footage is taken by the camera, the computer passes it to a real-time analysis program, allowing us to continuously quantify the fluorescent signal with virtually no lag time. Due to the nature of the microfluidic design, this entire process is inherently automated and requires minimal user input.

Measuring *in vitro* TNFα concentration

We first compared the results of our on-chip measurements against an analogous benchtop assay. Similar devices in the literature tend to incorporate multiple 'washing' steps where the magnetic beads are directed into a buffer stream in between protein capturing steps and labeling steps[35–38]. This increases the complexity of the device by necessitating additional fluidic inlets and results in a lower overall incubation time since large portions of the chip must be dedicated to additional sample processing. The proposed design eliminates these steps by incubating the antibody conjugated magnetic beads with the fluorescently labeled aptamer in the sample of interest at the same time. As a result, we need to know the effects of forming a sandwich complex in a high protein background without washing steps in between. We prepared serial dilutions of TNFα in PBS buffer ranging from 100 nM to 10 pM. For the on-chip measurements, we then pumped the TNFα solution through the device at a rate of 0.8 ml/hr. Simultaneously, we pumped a reagent mixture containing 500 nM of PE-labeled anti-TNFα aptamer and a 1:500 dilution (~$1x10^5$ beads/mL) of antibody-coated paramagnetic beads (Dynabeads M-450) through the device at a rate of 1.2 mL/hr. Given the dimensions of the microfluidic channel, this flow rate corresponds to an incubation time of approximately 30 s. For each concentration of TNFα, we collected the sorted beads at the outlet and measured their fluorescence on a flow cytometer (BD FACSVerse). Between

runs, the chip was thoroughly washed with PBS buffer and allowed to equilibrate for approximately 5 min at the new TNFα concentration before performing further measurements [Figure 2]. Despite the short incubation time, we see the expected binding isotherm, indicating that we can use our device to perform quantitative measurements of proteins in a complex background.

In order to perform real-time measurements, we need to be able to perform these measurements continuously. In order to do so, we developed an algorithm to measure bead fluorescence in real time inside of the device using a CCD camera attached to a fluorescent microscope. We compared the fluorescence results of samples prepared in our device and

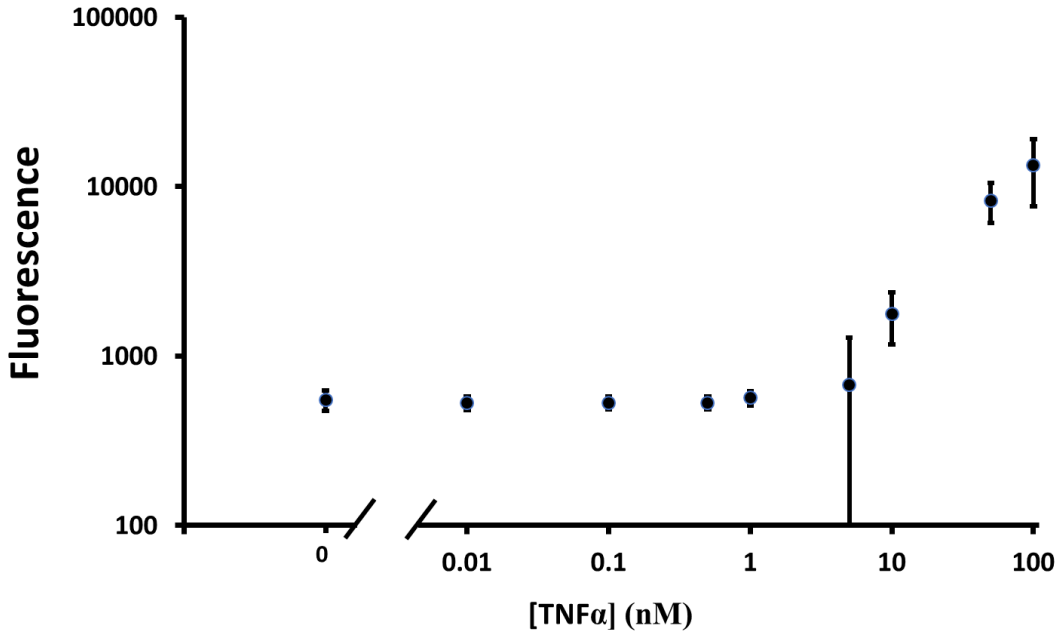

Figure 2. Using our device, we were able to construct a binding isotherm for TNFα. We flowed whole blood spiked with varying concentrations of TNFα through the device in conjunction with our reagent mixture, which contained antibody labeled microbeads as well as fluorescently labeled aptamer. After incubating for approximately 30 seconds, the MFS features passively sorted the now fluorescently labeled beads from the background medium, which were then collected at the outlet and analyzed with a flow cytometer.

measured with our algorithm to that of samples prepared on a more traditional benchtop setup and measured with a flow cytometer. We prepared the on-chip samples as above, this time spiking the blood with concentrations ranging from 10 pM to 100 nM. From this measurement, we determined that the analysis program could detect fluorescence at concentrations as low as 100 pM [Figure 3a]. Below this, the program could not effectively differentiate the beads from the background fluorescence. To validate our algorithm, we then compared the mean fluorescence of our traces evaluated with the algorithm to bead fluorescence measured with flow cytometry. We mixed various dilutions of TNFα spiked with the reagent mixture at a ratio of 1:1.5 and incubated for 30 min, then washed the beads with a PBS buffer. This mimicked the reagent ratios found in the device albeit with a much longer incubation time and more effective washing steps. After preparing the beads, we measured the median bead fluorescence at each TNFα concentration using a flow cytometer (BD FACSVerse). Our results show a linear correlation between the data gathered using our chip after a short incubation and the results gathered using a commercial device after 30 min of equilibration [Figure 3b].

Having determined that our device could perform quantitative measurements at a reasonable sensitivity, we then sought to demonstrate the ability of our device to perform long term measurements of dynamic protein concentration changes. As before, we pumped reagents into the device using a Harvard Apparatus pump at 1.2 mL/hr. In order to vary the protein concentration as a function of time, we switched to a peristaltic pump to draw blood from open topped containers and pump into the device at a rate of 0.8 mL/hr. We doped whole blood with either 5 nM or 100 nM of TNFα and then switched inputs every 30 min, the

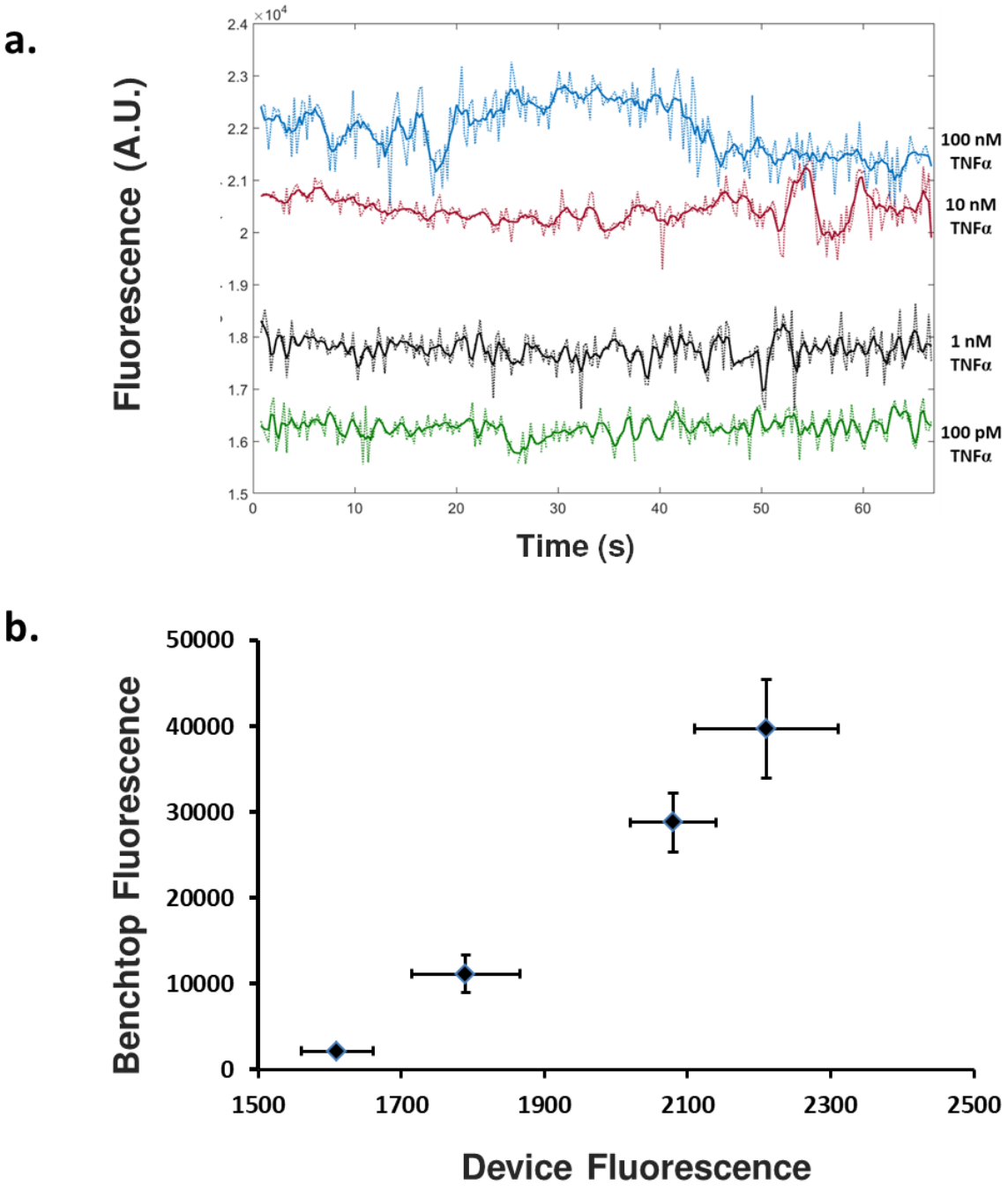

Figure 3. (a) To test the sensitivity of our device and detection algorithm, we doped whole blood with varying concentrations of TNFα. We found that under ideal conditions we could detect concentrations as low as 100 pM of TNFα. Below this, the detection algorithm frequently missed beads or confused them with the background. The dotted lines represent the raw data while the solid lines represent a rolling average. (b) We then verified our results by comparing the fluorescence measured with our device/image detection algorithm with results from a comparable benchtop assay measured with a commercial flow cytometer

entire time monitoring the resulting on-chip fluorescence signal using our image detection program. The results of these measurements are shown in Figure 4. For such long measurements it became necessary to bin the data each minute and measure the average fluorescence of these bins in order to minimize the effect small clots and spurious beads becoming trapped in the device and incubating for longer than desired. We see that there is an approximately 5 min delay between the concentration changes and the resulting measurements. This is likely attributable to the dead volume from the various fluidic connections between the blood reservoir and the device coupled with a low overall flow rate. Additionally, we see that the system started to become unstable after ~85 min. At this point a large blood clot began blocking the channel and forcing us to halt further measurements. Despite these issues, we can see a clear differentiation between the low-TNFα and high-TNFα blood, giving us an unparalleled ability to measure protein concentration changes in complex media in real time.

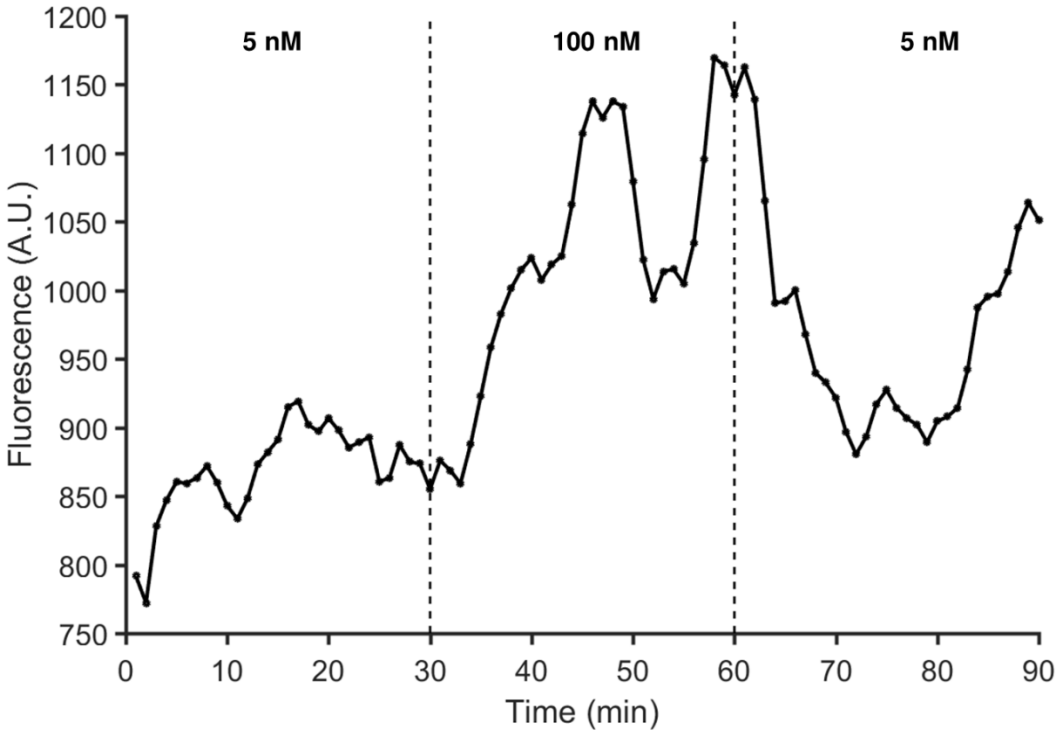

Figure 4. We varied the concentration of TNFα in whole blood over a period of approximately 90 minutes and continuously measured the average fluorescence. Whole blood was pumped into the device from one of two open-top containers using a peristaltic pump. After a half-hour, tubing was quickly switched from the low TNFα to high TNFα container. At one hour, the source was switched back. In order to mitigate the effect of clots and trapped beads on our data, we divided our data into 1-minute bins and averaged the fluorescence of each bin. After ~ 80 min a clog in the device disrupted the flow of beads through the channel, resulting in the termination of the experiment.

Materials and Methods

Microfluidic devices:

The microfluidic device necessary to carry out these operations was fabricated using standard soft lithography techniques [39,40]. To briefly summarize, a mold was created by spinning SU8 2050 photoresist onto a clean silicon wafer and subsequently baked at 95^0C for 6 minutes. After exposing the first SU8 layer, a second layer of SU8 2015 was then spun onto the wafer surface. This layer is used to form the raised herringbone patterns necessary for the mixing stage of the device. The wafer was then baked again at 95^0C for 6 minutes. At this point, the outline of the channels was clearly visible through the thin layer of SU8 2015, and so we could align a second photomask with the channels and perform a second exposure for the same time and intensity as the first. The wafer was then baked at 95^0C for a third time before being immersed in a solution of SU8 developer. Analysis using a Dektak profilometer showed the channels to be 40 μm high and 500 μm wide. The MFS structures were fabricated by first spinning AZ 5214 photoresist onto a glass wafer. 10 μm wide MFS patterns were formed with a photomask by exposing the wafer to 7 mW/cm^2 of UV light for 5 seconds. The wafer was then baked at 115^0C for 2 minutes before performing a second exposure at 7 mW/cm^2 for 1 min. Afterwards, the wafer was developed in a 4:1 dilution of AZ 400K developer for 35 seconds. The wafer was washed and residual organic matter was removed using an ozone oven. 200 Å of titanium was deposited on the surface via electron beam deposition, followed by 1800 Å of nickel to serve as the ferromagnetic layer. The undeveloped areas of photoresist were then stripped by submerging the wafer in an acetone bath, leaving only the MFS features behind. In addition to the MFS, we deposited nickel

alignment marks at the same time in order to assist with aligning the microfluidic channels with the MFS and permanent magnet.

To create the channels themselves, we poured polydimethylsiloxane (PDMS) on the mold and placed the wafer under vacuum to degas the PDMS. The wafer was then cured at 80^0C for 2 hours. In order to create a permanent bond between the PDMS and backing wafer, each set of channels was peeled off of the mold and placed in a Novascan PSD ozone system for 10 minutes along with a MFS backing wafer. The channels were then aligned manually with the MFS features and were left overnight to bond.

Analysis program:

In order to measure the fluorescence of each magnetic bead, we wrote a MATLAB program to analyze bead brightness in real time [Figure 5]. The beads are imaged with a Leica DM4000B upright microscope with an attached CCD camera (Hamamatsu). As a first step, the program connects to the camera and allows the user to adjust the exposure time and resolution. The program then requests the user select two "regions of interest" to analyze. The first region contains one or more MFS and will be where the bead fluorescence is analyzed. The second region of interest is a control region and should not contain any MFS strips where beads might get trapped. This region is used to calculate a background fluorescence which is later subtracted from the bead fluorescence. After selecting the regions of interest, the program then begins to search for beads using MATLAB's built in circular Hough transform function. This is a standard image processing technique. Briefly, a Hough transforms works by first analyzing the gradient of the image in order to identify edges (i.e. regions where there is a sudden shift from the dark background to a brighter

foreground feature such as an MFS or a fluorescent bead). For each edge pixel, the algorithm then evaluates whether its neighboring edge pixels fit the definition of a circle. If enough pixels fit the definition of a circle to pass some user-defined threshold, the algorithm then returns the *(x,y)* value corresponding to the center of the circle as well as its radius.

After the circle detection algorithm returns these values for all circles detected within the region of interest, the program then constructs a digital "mask", which is a matrix the same size as the measurement region of interest as selected by the user, but with values of 1 for every area where beads were recognized by the Hough transform and values of 0 otherwise.

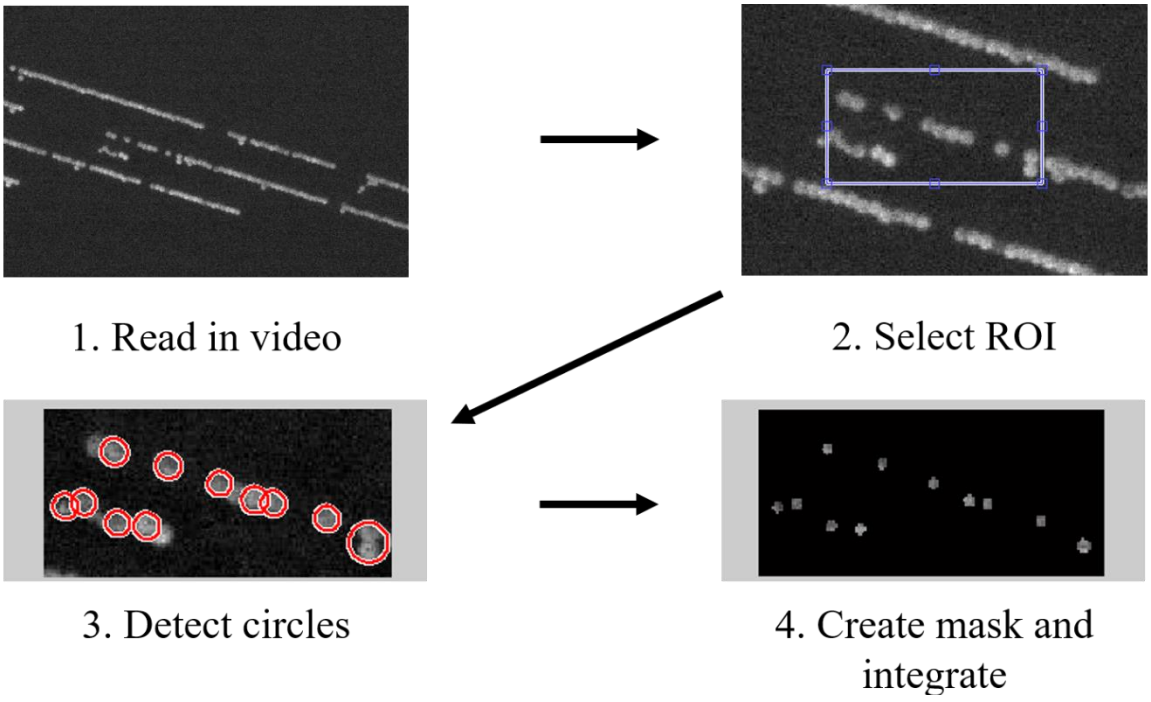

Figure 5. The analysis program works by feeding in video frames and analyzing a small region of interest selected by the user. The program searches for circles in this region (corresponding to fluorescent beads), and then creates a digital mask which is laid over the frame. The pixel values of the masked frame are integrated and then divided by the number of beads present to form an average "brightness-per-bead", which is then reported to the main program. After finishing with one frame, the program then moves on to the most recent frame available from the camera, allowing it to analyze the data in real time at a frame rate of approximately 2 frames per second.

We then produce a filtered image by multiplying the matrix representing the current camera frame by the mask. This returns a filtered image matrix with non-zero pixel values corresponding to the brightness of each bead where circles were detected and values of zero otherwise. The program then sums all of the values of this filtered image and divides by the number of detected beads in order to give an average "brightness-per-bead" for a given camera frame.

We noticed that when running the device for longer periods of time, ultra-bright beads would begin to appear, preventing the circle detection algorithm from recognizing other, less bright beads. Presumably, this was due to beads becoming temporarily trapped in the device and therefore incubating in the presence of target much longer than their companion beads before eventually working their way free. We used several strategies to prevent this phenomenon from distorting the reported data. First, the program only calculates the brightness-per-bead if two or more beads are detected. Second, the program keeps a bin of the brightness values of the most recent 50 beads. If, for a given frame, the average brightness-per-bead is more than three times the standard deviation of the binned beads away from the average brightness of the binned beads, the values of the current frame are considered an outlier and are not reported to the main program (although they are recorded in the bead brightness bin, meaning that if a large change is sustained it will be reported within a few frames of when it began). Finally, for time periods greater than an hour, the program reports the average fluorescence value over a minute-long period. While this lowers our time resolution, it greatly helps alleviate the effect of noise on the system.

Fluidic operation:

Prior to running each experiment, the microfluidic chip was placed atop a ½"x ¼"x ⅛" neodymium magnet. We then prepared a fresh batch of both the reagent and buffer solutions. For the reagent solution, a 1:500 dilution of antibody functionalized 4.5 µm magnetic beads (Dynabeads) was prepared in a PBS buffer. To this was added 500 nM of biotinylated affinity reagent (IDT) as well as 10 mg/ml BSA and 500 nM of SAPE. The imaging buffer solution consisted of 2.5 mg/ml BSA in a solution of PBS and 0.25% tween-20. Both the imaging buffer and reagent solutions were then loaded into syringes and interfaced with the device using 0.02" tygon tubing (Cole-Parmer). The reagent mixture was pumped at 1.2 ml/hr using a Harvard Apparatus syringe pump. The imaging buffer was likewise pumped with a Harvard Apparatus syringe pump. The optimal flow rate was determined at the beginning of each experiment. Depending on the precise alignment of the magnet with the fluidic channel, we found that this rate typically ranged between 4.5 ml/hr and 5 ml/hr.

Human whole blood preparation:

For measuring doped protein levels in blood, human whole blood treated with sodium citrate anticoagulant was ordered from Bioreclamation LLC. Whole blood was refrigerated at 4°C until use. Before use, blood was warmed to room temperature and then passed through a 40-mm pore cell strainer (Thermo Fisher Scientific) to remove any clots or aggregates which may have formed. Concentrated target (TNFα or F1.2) was then doped into the blood at the desired levels.

Discussion

While there has been considerable success in recent years in creating new and highly sensitive immunoassays, the long and complicated sample processing steps necessary to make these assays work means that they are unable to offer insight into dynamic systems. This is unfortunate considering that there are many conditions which could be better diagnosed and monitored by measuring the time dependent change of the concentration of moderate-to-high abundance proteins. In this work, we have attempted to address this deficiency by designing a microfluidic chip capable of performing continuous, real-time, concentration measurements of medium to high abundance proteins directly in whole blood.

While our device/analysis program is unable to reach the same limits of detection as traditional bioassays, it is capable of extremely fast measurements, allowing it to track concentration in real time. With a maximum time resolution of two measurements per second over short periods and a time resolution of one measurement per minutes over time periods extending over one hour, our device offers unprecedented time resolution for tracking concentration changes in medium to high abundance proteins. Furthermore, these measurements are fully automated and are performed on undiluted whole blood. Along with being fully automated, the system is also modular, meaning that the user need only swap out the affinity reagents used in order to measure a different target. Additionally, the system is agnostic to the type of affinity reagent used (aptamers vs monoclonal antibodies vs polyclonal antibodies), making it much more flexible than other systems. We hope in the future to expand on this work to both increase the stability of the system over long time

periods and to swap out the reagents in order to measure more clinically relevant targets, such as proteins involved in the coagulation pathway.

References

(1) Janssen, K. P. F.; Knez, K.; Spasic, D.; Lammertyn, J. Nucleic Acids for Ultra-Sensitive Protein Detection. *Sensors (Basel)* **2013**, *13* (1), 1353–1384.

(2) Sano, T.; Smith, C. L.; Cantor, C. R. Immuno-PCR: Very Sensitive Antigen Detection by Means of Specific Antibody-DNA Conjugates. *Science* **1992**, *258* (5079), 120–122.

(3) Vogelstein, B.; Kinzler, K. W. Digital PCR. *PNAS* **1999**, *96* (16), 9236–9241.

(4) Brody, E. N.; Gold, L.; Lawn, R. M.; Walker, J. J.; Zichi, D. High-Content Affinity-Based Proteomics: Unlocking Protein Biomarker Discovery. *Expert Rev. Mol. Diagn.* **2010**, *10* (8), 1013–1022.

(5) Levi, M. Disseminated Intravascular Coagulation. *Crit. Care Med.* **2007**, *35* (9), 2191–2195.

(6) Bakhtiari, K.; Meijers, J. C. M.; de Jonge, E.; Levi, M. Prospective Validation of the International Society of Thrombosis and Haemostasis Scoring System for Disseminated Intravascular Coagulation. *Crit. Care Med.* **2004**, *32* (12), 2416–2421.

(7) Xiao, Y.; Lubin, A. A.; Heeger, A. J.; Plaxco, K. W. Label-Free Electronic Detection of Thrombin in Blood Serum by Using an Aptamer-Based Sensor. *Angew. Chem. Int. Ed. Engl.* **2005**, *44* (34), 5456–5459.

(8) Willner, I.; Zayats, M. Electronic Aptamer-Based Sensors. *Angew. Chem. Int. Ed. Engl.* **2007**, *46* (34), 6408–6418.

(9) Hamaguchi, N.; Ellington, A.; Stanton, M. Aptamer Beacons for the Direct Detection of Proteins. *Anal. Biochem.* **2001**, *294* (2), 126–131.

(10) Castner, D. G.; Ratner, B. D. Biomedical Surface Science: Foundations to Frontiers. *Surface Science* **2002**, *500* (1–3), 28–60.

(11) Roggan, A.; Friebel, M.; Do Rschel, K.; Hahn, A.; Mu Ller, G. Optical Properties of Circulating Human Blood in the Wavelength Range 400-2500 Nm. *J Biomed Opt* **1999**, *4* (1), 36–46.

(12) Nachabé, R.; Evers, D. J.; Hendriks, B. H. W.; Lucassen, G. W.; van der Voort, M.; Wesseling, J.; Ruers, T. J. M. Effect of Bile Absorption Coefficients on the Estimation of Liver Tissue Optical Properties and Related Implications in Discriminating Healthy and Tumorous Samples. *Biomed Opt Express* **2011**, *2* (3), 600–614.

(13) Wang, J.; Yu, J.; Yang, Q.; McDermott, J.; Scott, A.; Vukovich, M.; Lagrois, R.; Gong, Q.; Greenleaf, W.; Eisenstein, M.; et al. Multiparameter Particle Display (MPPD): A Quantitative Screening Method for the Discovery of Highly Specific Aptamers. *Angewandte Chemie International Edition* **2017**, *56* (3), 744–747.

(14) Damas, P.; Reuter, A.; Gysen, P.; Demonty, J.; Lamy, M.; Franchimont, P. Tumor Necrosis Factor and Interleukin-1 Serum Levels during Severe Sepsis in Humans. *Crit. Care Med.* **1989**, *17* (10), 975–978.

(15) Damas, P.; Ledoux, D.; Nys, M.; Vrindts, Y.; De Groote, D.; Franchimont, P.; Lamy, M. Cytokine Serum Level during Severe Sepsis in Human IL-6 as a Marker of Severity. *Ann. Surg.* **1992**, *215* (4), 356–362.

(16) Zhang, J.; Yan, S.; Yuan, D.; Alici, G.; Nguyen, N.-T.; Warkiani, M. E.; Li, W. Fundamentals and Applications of Inertial Microfluidics: A Review. *Lab on a Chip* **2016**, *16* (1), 10–34.

(17) Squires, T. M.; Quake, S. R. Microfluidics: Fluid Physics at the Nanoliter Scale. *Rev. Mod. Phys.* **2005**, *77* (3), 977–1026.

(18) Stone, H. A.; Stroock, A. D.; Ajdari, A. Engineering Flows in Small Devices: Microfluidics Toward a Lab-on-a-Chip. *Annual Review of Fluid Mechanics* **2004**, *36* (1), 381–411.

(19) Purcell, E. M. Life at Low Reynolds Number. 10.

(20) Oh, K. W.; Lee, K.; Ahn, B.; Furlani, E. P. Design of Pressure-Driven Microfluidic Networks Using Electric Circuit Analogy. *Lab Chip* **2012**, *12* (3), 515–545.

(21) Teh, S.-Y.; Lin, R.; Hung, L.-H.; Lee, A. P. Droplet Microfluidics. *Lab Chip* **2008**, *8* (2), 198–220.

(22) Xu, J. H.; Li, S. W.; Tan, J.; Wang, Y. J.; Luo, G. S. Preparation of Highly Monodisperse Droplet in a T-Junction Microfluidic Device. *AIChE Journal* **2006**, *52* (9), 3005–3010.

(23) Thorsen, T.; Roberts, R. W.; Arnold, F. H.; Quake, S. R. Dynamic Pattern Formation in a Vesicle-Generating Microfluidic Device. *Phys. Rev. Lett.* **2001**, *86* (18), 4163–4166.

(24) Nisisako, T.; Torii, T.; Higuchi, T. Droplet Formation in a Microchannel Network. *Lab Chip* **2002**, *2* (1), 24–26.

(25) Song, H.; Chen, D. L.; Ismagilov, R. F. Reactions in Droplets in Microfluidic Channels. *Angewandte Chemie International Edition* **2006**, *45* (44), 7336–7356.

(26) Iv, C. W. S.; Reyes, C. D.; López, G. P. Microfluidic Cell Sorting: A Review of the Advances in the Separation of Cells from Debulking to Rare Cell Isolation. *Lab Chip* **2015**, *15* (5), 1230–1249.

(27) Voldman, J. Electrical Forces for Microscale Cell Manipulation. *Annu. Rev. Biomed. Eng.* **2006**, *8* (1), 425–454.

(28) Zborowski, M.; Chalmers, J. J. Rare Cell Separation and Analysis by Magnetic Sorting. *Anal. Chem.* **2011**, *83* (21), 8050–8056.

(29) Ng, J. M. K.; Gitlin, I.; Stroock, A. D.; Whitesides, G. M. Components for Integrated Poly(Dimethylsiloxane) Microfluidic Systems. *ELECTROPHORESIS* **2002**, *23* (20), 3461–3473.

(30) Nguyen, N.-T.; Wu, Z. Micromixers—a Review. *J. Micromech. Microeng.* **2004**, *15* (2), R1–R16.

(31) Stroock, A. D.; Dertinger, S. K. W.; Ajdari, A.; Mezić, I.; Stone, H. A.; Whitesides, G. M. Chaotic Mixer for Microchannels. *Science* **2002**, *295* (5555), 647–651.

(32) Adams, J. D.; Kim, U.; Soh, H. T. Multitarget Magnetic Activated Cell Sorter. *PNAS* **2008**, *105* (47), 18165–18170.

(33) Inglis, D. W.; Riehn, R.; Austin, R. H.; Sturm, J. C. Continuous Microfluidic Immunomagnetic Cell Separation. *Appl. Phys. Lett.* **2004**, *85* (21), 5093–5095.

(34) Smistrup, K.; Hansen, O.; Bruus, H.; Hansen, M. F. Magnetic Separation in Microfluidic Systems Using Microfabricated Electromagnets—Experiments and Simulations. *Journal of Magnetism and Magnetic Materials* **2005**, *293* (1), 597–604.

(35) Phurimsak, C.; Tarn, M. D.; Peyman, S. A.; Greenman, J.; Pamme, N. On-Chip Determination of C-Reactive Protein Using Magnetic Particles in Continuous Flow. *Anal. Chem.* **2014**, *86* (21), 10552–10559.

(36) Sasso, L. A.; Aran, K.; Guan, Y.; Ündar, A.; Zahn, J. D. Continuous monitoring of inflammation biomarkers during simulated cardiopulmonary bypass using a microfluidic immunoassay device – a pilot study. *Artif Organs* **2013**, *37* (1), E9–E17.

(37) Sasso, L. A.; Ündar, A.; Zahn, J. D. Autonomous Magnetically Actuated Continuous Flow Microimmunofluorocytometry Assay. *Microfluid Nanofluidics* **2010**, *9* (2–3), 253–265.

(38) Peyman, S. A.; Iles, A.; Pamme, N. Mobile Magnetic Particles as Solid-Supports for Rapid Surface-Based Bioanalysis in Continuous Flow. *Lab Chip* **2009**, *9* (21), 3110–3117.

(39) Xia, Y.; Whitesides, G. M. Soft Lithography. *Angewandte Chemie International Edition* **1998**, *37* (5), 550–575.

(40) Rapid Prototyping of Microfluidic Systems in Poly(dimethylsiloxane) | Analytical Chemistry

III. An electrochemical scaffold sensor for rapid syphilis diagnosis

Introduction

In the previous chapter, we introduced a microfluidic device designed for real-time monitoring of protein concentrations. While designed as a point-of-care device, this system still requires a continuous supply of reagents as well as extensive instrumentation (such as a fluorescent microscope, computer, and various pumps to operate the fluidics), and thus is better suited to a hospital setting where the space requirements and upfront cost are less of an issue. For many applications, such as disease diagnostics however, continuous measurements are unnecessary and instead the more important factor is the portability of the system, the cost, as well as the time to response. After all, the more rapidly a disease is diagnosed, the sooner treatment can be initiated, which improves both compliance and outcomes, and therefore renders it desirable to achieve diagnosis within the timeframe of a single patient/clinician interaction[1]. This is particularly true for infectious diseases, as single-visit diagnosis allows for the treatment of patients who would otherwise be lost to follow up, enabling healthcare providers to intervene immediately to change behaviors and limit transmission[2–5]. Accomplishing this, however, necessitates diagnostic tools that are simple enough to use at the point of care and are capable of returning answers within minutes rather than hours, attributes that the current, largely laboratory-centered approaches to molecular diagnostics fail to achieve[6].

The potential value of improved point-of-care diagnostics is illustrated by the "gold-standard" approach for diagnosing syphilis, a disease for which the incidence rate has more than doubled in the United States during the past decade[7]. The current standard of care for

syphilis diagnosis involves two serological tests performed in sequence. The first, the "nontreponemal" test, detects the presence of cardiolipids associated with cell damage and is used to determine whether a patient has an active infection[8–10]. The second, "treponemal" test, detects antibodies specifically indicative of exposure to pathogenic bacteria from the Treponema genus such as Treponema pallidum pallidum, the causative agent of syphilis[11]. This two-pronged approach[12] is employed because the specificity of the two individual tests is poor; other underlying illnesses or pregnancy can cause false positives in the non-treponemal test and antibodies remaining from past exposure (rather than ongoing infection) can cause false positives in the treponemal test[13,14]. However, while the two-pronged approach improves clinical specificity, it slows down diagnosis. Specifically, while the non-treponemal test can be performed rapidly at the point of care using assays such as the rapid plasma reagin test, the treponemal test relies on traditional serological assays (e.g., hemagglutination, Western blotting, or enzyme linked immunosorbent assays), thus necessitating specialized lab facilities[15,16]. Given this, a rapid treponemal test capable of being deployed at the point of care could help to limit the spread of syphilis by eliminating the gap between a patient's initial visit and a positive diagnosis, allowing clinicians to intervene immediately.

Motivated by the general need for improved, point-of-care serological tests, we have recently developed a general platform for rapid (< 10 min), convenient measurement of the concentration of specific antibodies in unprocessed serum [Figure 1] and have adapted it here to the treponemal test. Electrochemical DNA (E-DNA) biosensors have already proven to be a versatile platform for detection of analytes in complex media such as serum[17–19].

Here we use a modification of the E-DNA scaffold platform[20], which is comprised of a nucleic acid duplex ("scaffold") bound to the surface of an electrode via a flexible linker. On the distal end of this scaffold, a redox reporter is conjugated to one end of the DNA backbone, while a recognition element, such as an antigenic protein, is bound to the other. Binding of an antibody to the recognition element reduces the efficiency with which the redox reporter approaches the electrode surface, resulting in a change in electron transfer rate that can rapidly and conveniently be measured using standard electrochemical approaches.

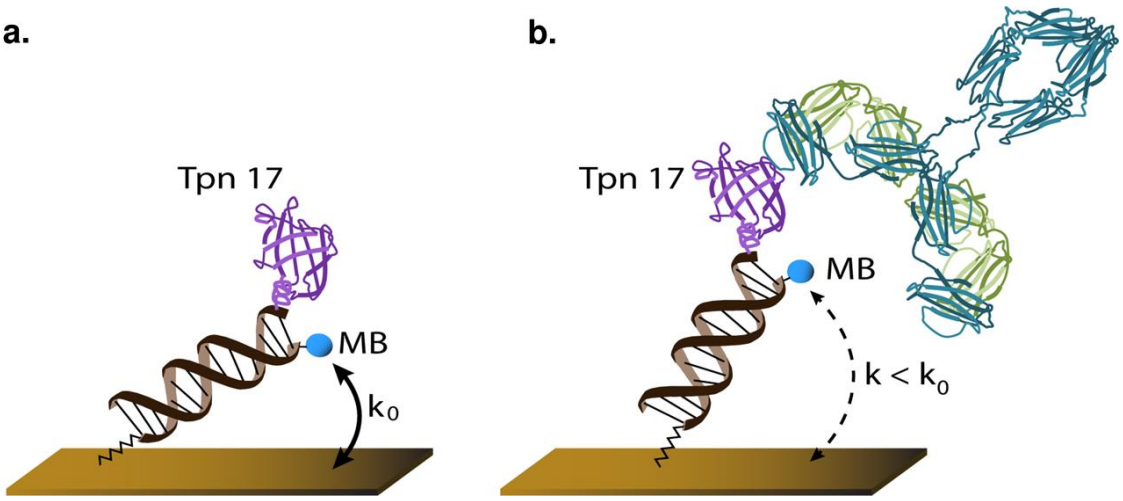

Figure 1. (a) E-DNA scaffold sensors are comprised of a nucleic acid "scaffold" bound to the surface of a gold electrode via a flexible linker (Cash et al., 2009). The distal end of the scaffold is modified with a redox reporter (here methylene blue; MB), and a nitrilotriacetic acid (NTA) that, in the presence of copper, tightly binds a hexa-his tag on the antigen (here TpN17). (b) Binding of the target antibody to the recognition element reduces the efficiency with which the redox reporter approaches the surface of the electrode, reducing the electron transfer rate and, in turn, the current observed when the sensor is interrogated using square wave voltammetry.

Results

The first step in fabricating antibody-detecting scaffold sensors is the identification of an appropriate antibody-recognizing epitope or antigen. All previous examples of sensors in this class employed relatively short (< 18 amino acid) linear epitopes or low molecular weight haptens as these recognition elements[20–23]. Due to the difference in size between the recognition peptide and corresponding antibody these have the advantage of producing large signal gain (relative change in signal upon the addition of saturating target)[24]. They nevertheless suffer from two potentially significant limitations. First, not all antigens involve linear epitopes, reducing the generality of the approach. Second, not all patients seroconvert (i.e., generate detectable antibodies) against any given epitope. In contrast, the use of full-length or near-full-length antigens as recognition elements supports the simultaneous presentation of multiple linear and conformational epitopes, which should improve clinical sensitivity by expanding the range of diagnostically relevant antibodies that can be detected and increasing the likelihood that the patient will have seroconverted for one of the epitopes present.

In order to help determine the maximum possible size of our affinity reagent, we developed a Monte Carlo simulation of a scaffold sensor, allowing us to explore the effect of recognition element size on signal gain. The model generates a set number of scaffold conformations and, for each conformation in our ensemble, we individually rebuild the DNA scaffold in order to sample many independent conformations. To build each new scaffold the position of the first base pair is defined by randomly choosing a rotational angle, ρ, from the evenly distributed range 0 and 2π and an angle, θ, the angle between the axis and the surface, which is randomly

selected from a Gaussian distribution centered on 0; the width of the Gaussian we employ defines the flexibility of the linker connecting the scaffold to the surface [Figure 2a]. The center of the base pair is then placed 6 Å from the origin along this vector, corresponding to the length of the carbon linker attaching the anchor strand to the surface. The position of the DNA backbone is then determined via appropriate coordinate transfers. For each subsequent base, new angles, ρ_i and θ_i, (relative to the coordinates of the previous base) are randomly selected. The rotational angle, ρ_i, is selected from a Gaussian distribution centered on the average rotational angle between DNA base pairs (0.6178 radians)[25] with a standard deviation of 0.0125, while the bend angle, θ_i, is selected from a distribution centered on 0 with a standard deviation of $\frac{\pi}{60}$. A sphere representing the center of the next DNA base pair is placed 3.38 Å (the per-base translation of DNA) away along this vector and the position of the backbone again determined. The program tracks the overall bend and twist angles and uses them to convert from the local coordinates (spherical coordinates calculated for each new base relative to the previous base) to a global Cartesian coordinate calculated relative to an origin located at the attachment point of the anchor to the surface. This is accomplished by first converting from local spherical coordinates of the n^{th} base to local Cartesian coordinates relative to the $(n\text{-}1)^{th}$ base:

$$\overrightarrow{r_n}' = [L_B \sin(\theta_n)\cos(\rho_n), L_B \sin(\theta_n)\sin(\rho_n), L_B \cos(\theta_n)]'$$

where $\overrightarrow{r_n}'$ is the 3x1 matrix the location of the n^{th} base given in local Cartesian coordinates relative to the previous base's reference frame, and L_B is the length per base of double stranded DNA. We then define two rotational matrices used to convert between the local Cartesian coordinates and global coordinates:

$$R_\theta = \begin{bmatrix} \cos(\Delta\theta) & 0 & \sin(\Delta\theta) \\ 0 & 1 & 0 \\ -\sin(\Delta\theta) & 0 & \cos(\Delta\theta) \end{bmatrix}$$

$$R_\rho = \begin{bmatrix} \cos(\Delta\rho) & -\sin(\Delta\rho) & 0 \\ \sin(\Delta\rho) & \cos(\Delta\rho) & 0 \\ 0 & 0 & 1 \end{bmatrix}$$

where $\Delta\rho$ and $\Delta\theta$ are given by:

$$\Delta\rho = \sum_{i=1}^{n-1} \rho_i$$

$$\Delta\theta = \sum_{i=1}^{n-1} \theta_i$$

From this, we can determine the position of the nth base in global coordinates centered at the origin, which is then:

$$\overrightarrow{r_n} = R_\theta R_\rho \overrightarrow{r_n}' + \sum_{i=1}^{n-1} \vec{r_i}$$

This process is reiterated 27 times to create our scaffold (27 bases being the length of the scaffold currently employed in our experiments). Upon reaching the final base pair the position of the methylene blue reporter is defined by placing a sphere 7 Å away (to account for the size of the methylene blue and its linker) normal to one of the backbone chains. The "protein" is then simulated by attaching a variable radius sphere 3 Å away (to account for the length of the his-tag) from the opposite backbone. To simulate a flexible attachment from the scaffold to the protein we define an angle, ϕ, defined as the angle of the linker relative to the vector of the last base pair, which is randomly selected from a Gaussian distribution of varying standard deviation. For comparison with our experimental data we converted these radii into molecular weights according to the following formula[26]:

$$R_g = 7.78(M)^{0.37}$$

To build our conformational ensembles, we next determined the energy of each conformation, which is comprised of the internal energy of the DNA and any interaction with the surface. The internal energy is given by:

$$U_{bend} = \sum_{k=2}^{n} \frac{\frac{k_b T}{2} L_p}{3.38} (1 - u_k \cdot u_{k-1})$$

$$U_{twist} = \sum_{k=2}^{n} \frac{k_b T}{2} \kappa (\rho_k - \bar{\rho})^2$$

Here L_p is the persistence length of double-stranded DNA (approximated to be 53.5 nm), u_k is the unit vector defining the kth base relative to the previous base, κ is the twist force constant for double-stranded DNA (203.49 radians^{-2})[25], and $(\rho_k - \bar{\rho})$ is the difference between the rotation angle of the kth base and the average rotational angle of double-stranded DNA. Interactions with the surface are defined by a hard-wall approach in which the energy of these interactions is zero for conformations that do not overlap with the monolayer and infinity if there is any overlap between the protein and the monolayer. The monolayer is simulated as an exclusion layer 9.25 Å from the surface. Using this potential, we used Monte Carlo approaches to simulate 1,000,000 conformations for each set of parameters (i.e., for each discrete value of θ, ϕ, and protein radius) to generate our ensembles.

Per Uzawa et al.[27] we calculated a weighted mean effective electron transfer rate (k_{eff}) for each ensemble according to:

$$k_{eff} = \frac{1}{n} \sum_{i=1}^{n} P_i \cdot k_i(z)$$

here n is the number of scaffolds with non-zero probability of occurring, P_i is the probability that the i[th] scaffold is in its current conformation as determined by Maxwell Boltzmann statistics, and $k_i(z)$ is a distance dependent electron transfer rate. The latter is given by a 1-D tunneling equation with a length constant of 1.2 $Å^{-1}$ [ref[28]].

Simulations of the scaffold sensor suggest that the dependence of the baseline peak current on molecular weight stems from simple geometric exclusion. Specifically, we see that the signal change begins to saturate when the weight of the attached recognition element corresponds to a radius of ~3.5 nm, which is roughly equivalent to the width of the dsDNA scaffold (~2 nm) plus the length of the methylene blue linker (~1 nm) [Figure 2]. We find that, besides the molecular weight of the attached protein, the simulated rate of electron transfer is also strongly dependent on the linker flexibility of the linker connecting the protein to the scaffold (ϕ), and the flexibility of the linker connecting the scaffold to the surface (θ) [Figure 2b, 2c]. Plots of relative estimated electron transfer rate versus recognition element molecular weight trace out shapes similar to those seen in experimental results[24]. The current suppression seen at the plateau, however, does not depend on the linker flexibility [Figure 2d], but rather is a function of the flexibility of the linker connecting the recognition element to the scaffold. This occurs because more flexible recognition elements can move to avoid colliding with the surface, an effect that presumably explains why the sensors we have characterized here, which use a highly flexible his-tag linker, plateau at lower signal suppression (~35% versus upwards of 50%) than the signal suppression we have previously seen in sensors employing shorter, less flexible linkers[20–22].

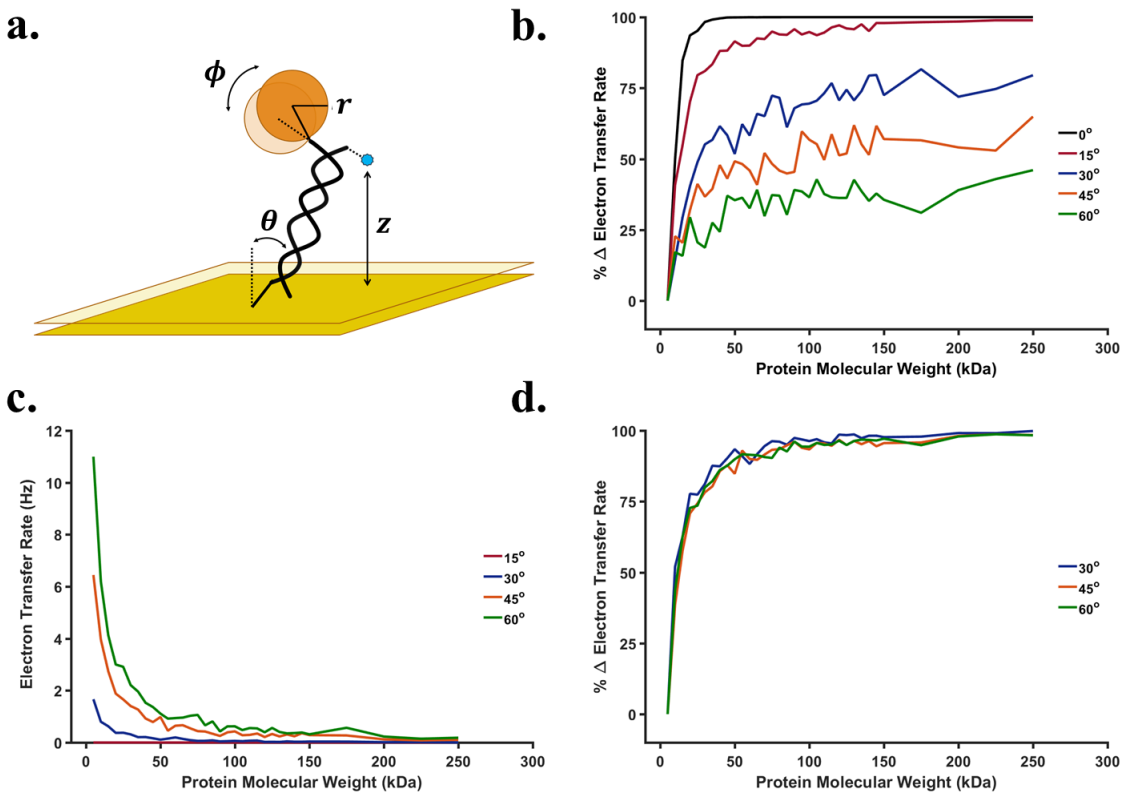

Figure 2. (a) To help understand the behavior of E-DNA scaffold sensors, we have developed a simple model employing three parameters, the flexibility of the linker connecting the DNA to the surface ($\boldsymbol{\theta}$), the flexibility of the linker connecting the protein to the scaffold ($\boldsymbol{\phi}$), and the radius of the attached protein ($\boldsymbol{r}$). (b) The estimated change in electron transfer rate relative to an unmodified scaffold is a strong function of the recognition element size as well as the flexibility of the linker connecting it to the scaffold (where the angle given is the width of the distribution that $\boldsymbol{\phi}$ adopts. (c) We see that the electron transfer rate is also strongly depended on the flexibility of the linker connecting the scaffold to the surface. (d) If we look at the change in electron transfer rate relative to an unmodified scaffold, however, we see that changing the surface linker flexibility does not affect the shape of the molecular weight gain curve.

The above results suggest that, while the signal change induced by target binding will fall as the recognition element increases in size, there is nevertheless "room" to exploit larger recognition elements than the largest we have previously employed. As their antibody-recognizing elements, most commercial treponemal assays employ a combination of up to four full-length T. pallidum membrane proteins ranging in size from 15 to 47 kDa[29]. According to our simulation results, we do not expect proteins larger than ~25 kDa to be useful

as part of scaffold sensors due to the small expected signal change between the unbound state and the antibody bound state. Fortunately, ELISAs employing TpN17 as their sole antigen, however, have been shown to achieve good clinical sensitivity and specificity for the diagnosis of syphilis[30]. Because this antigen is much larger than the largest epitopes previously employed in sensors of this class, we expected the resulting sensor to produce only relatively small gain and peak current, reducing the signal-to-noise ratio[24]. In response we pursued two, complementary methods of improving gain and signaling current. First, we engineered our recombinant TpN17 protein to include only the part of TpN17 corresponding to a previously reported crystal structure[31], reducing the protein's molecular weight to 15 kDa. Second, we explored several methods of improving the scaffold's electron transfer rate, which should lead to improved peak currents[24]. We expect from our simulations that increasing the flexibility of the linker between the scaffold and the surface should increase the current, even if it does not lead to larger signal changes upon binding. In order to verify this, we investigated three constructs differing in scaffold flexibility: (1) the relatively rigid, fully-double-stranded DNA scaffold we have used previously; (2) a peptide-nucleic-acid (PNA)/DNA hybrid scaffold, which we assume is more flexible based off of the conformational flexibility of PNA[32]; and (3) a double stranded DNA scaffold attached to the SAM via a flexible, 18-unit polyethylene glycol (PEG) linker. At each step of the fabrication process, we interrogated the sensors with square wave voltammetry, measured the peak current, and compared the magnitude of the current between constructs as normalized by the surface area of the sensing electrode [Figure 3].

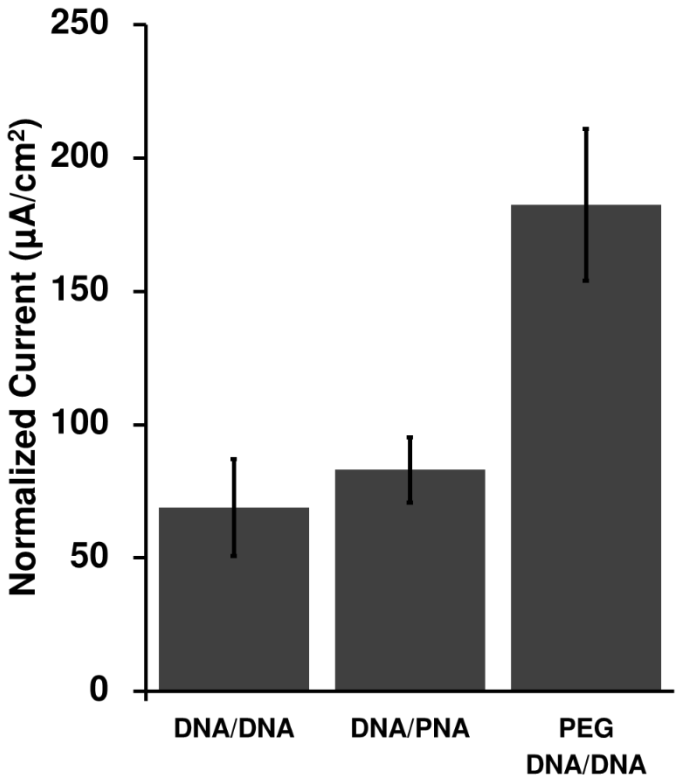

Figure 3. Here we compare the signaling of three sensor architectures varying in scaffold flexibility: a fully-double-stranded DNA scaffold (DNA/DNA), a DNA/peptide-nucleic-acid (PNA) scaffold, and a double stranded scaffold connected to the surface via a flexible polyethylene glycol (PEG) linker. The PEG DNA/DNA scaffold provides approximately twice the current (for a given sized sensor) as our previously employed, DNA/DNA scaffold, and thus we have employed it here. For each construct, we measured the peak current of nine individually fabricated electrodes and normalized each by the surface area of the individual electrode.

While the PNA/DNA scaffold provided a slightly higher peak current than the double stranded DNA scaffold, the PEG linker scaffold easily outperformed both, producing more than twice the peak current of the double-stranded DNA scaffold. Based on these results and on the ease of its fabrication we employed the PEG linker scaffold in our subsequent experiments.

When tested using monoclonal anti-TpN17 antibodies we see a monotonic relationship between signaling current and antibody concentration. To see this, we first established a baseline current in buffer solutions (i.e., without antibodies present), followed by titration with monoclonal antibodies and recording the signal change after a 20 min equilibration at each concentration [Figure 4a]. Fitting the titration curve to a Langmuir isotherm yielded a dissociation constant of 3 nM with the signal change saturating at a gain of ~13% after addition of effectively saturating (20 nM) antibody [Figure 4b]. Having established that we could detect monoclonal antibodies in buffer, we next challenged the sensor against anti-TpN17 monoclonal antibodies spiked into healthy (sero-negative) human serum. One of the chief challenges working in such a complex media is combatting non-specific adsorption of material to the surface of the sensor, which can cause anomalous signal changes resulting in baseline drift. To minimize such effects, we diluted the serum 20-fold with 1 M NaCl. After

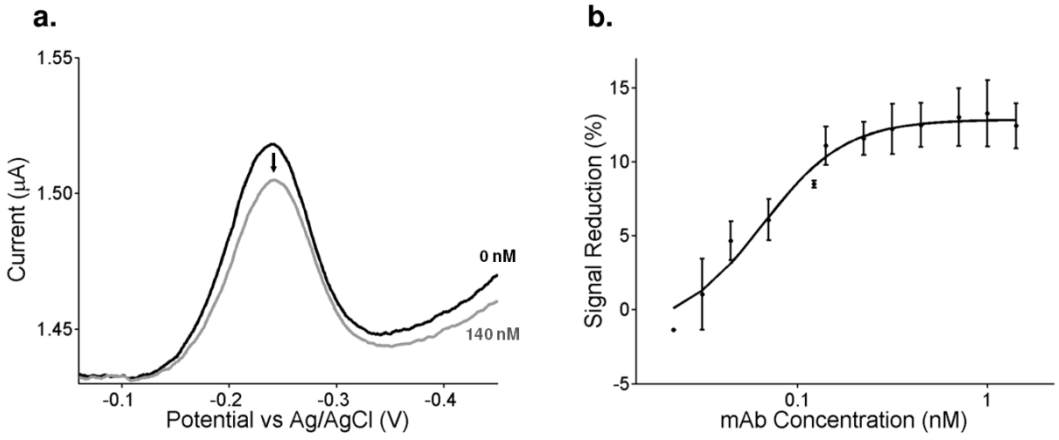

Figure 4. We accomplish antibody detection through electrochemical interrogation of the sensor. (a) To determine the concentration of antibody present in our sample, we measure the magnitude of the peak methylene blue current. Here we show the electrochemical response curves in the presence and absence of target, which we then use to form a binding curve. In order to account for any difference in current not due to the reduction of methylene blue, we used linear baseline subtraction normalize between measurements. (b) Upon the addition of increasing concentrations of monoclonal antibody, we observe a binding curve that is well fit by the expected Langmuir isotherm (R^2 = 0.98). The error bars represent the standard deviation of three independently fabricated electrodes.

the addition of 100 nM monoclonal antibody the sensor effectively equilibrated within 5 min and the signal remained stable thereafter [Figure 5]. The signal gain we observe under these conditions, however, is lower than that seen in buffer. As expected, in the absence of an antibody challenge the sensors exhibited no significant signal change.

As a demonstration of the clinical sensitivity and specificity of our platform we next challenged the platform with differentiating between syphilis-positive and syphilis-negative human serum samples. To do this we first confirmed the status of four commercially sourced, putatively syphilis-positive human samples and four equivalent syphilis-negative human samples using a commercially available ELISA [Figure 6a]. One of the syphilis-positive patients, identified as patient 4, only responded weakly to the ELISA. Nevertheless,

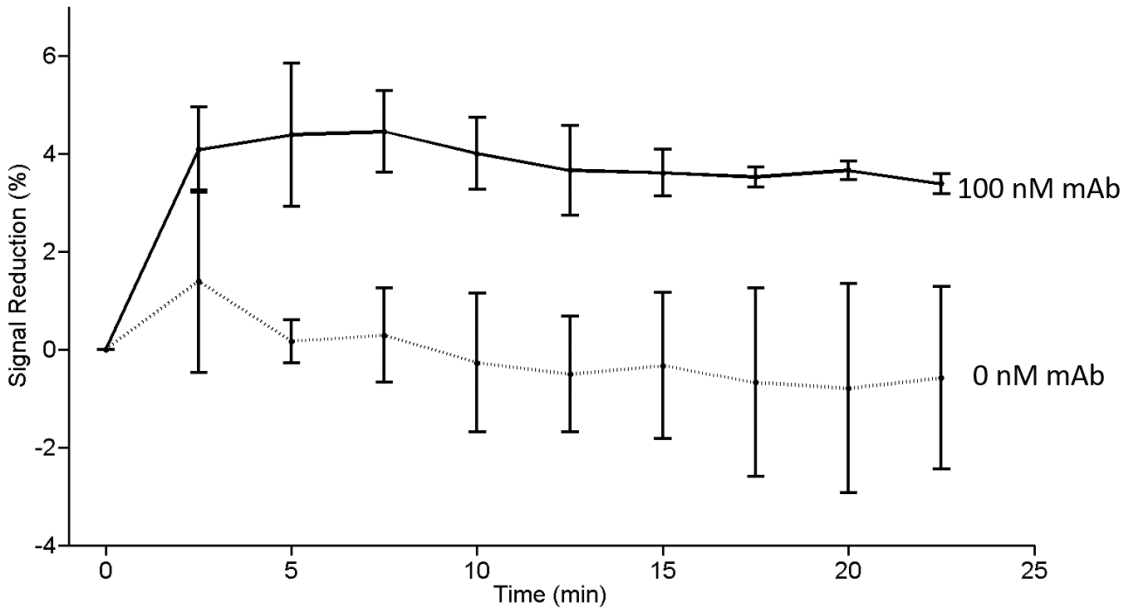

Figure 5. The sensor rapidly detects monoclonal antibody added to 1:20 diluted syphilis-negative human serum. Shown is the signal change seen in the absence and presence of a monoclonal anti-TnP17 antibody. The error bars represent the standard deviation of three independently fabricated electrodes.

the sample absorbance was still above the cutoff threshold determined using the calibration samples included in the kit. This was likely a result of the patient having a low antibody titer, although without further information from the ELISA manufacturer regarding the components of their kit this is speculative. We then measured each of the eight samples using our electrodes in order to compare to the ELISA. For each of the patients we prepared electrodes and sample dilutions as described above. We then placed the electrodes into the sample and performed an immediate baseline current measurement followed by a second measurement after 10 min. In every case the signal change between these two measurements differentiated the syphilis-positive samples from the negative samples with good statistical significance [Figure 6b], including in the case of the weakly reactive by ELISA patient 4.

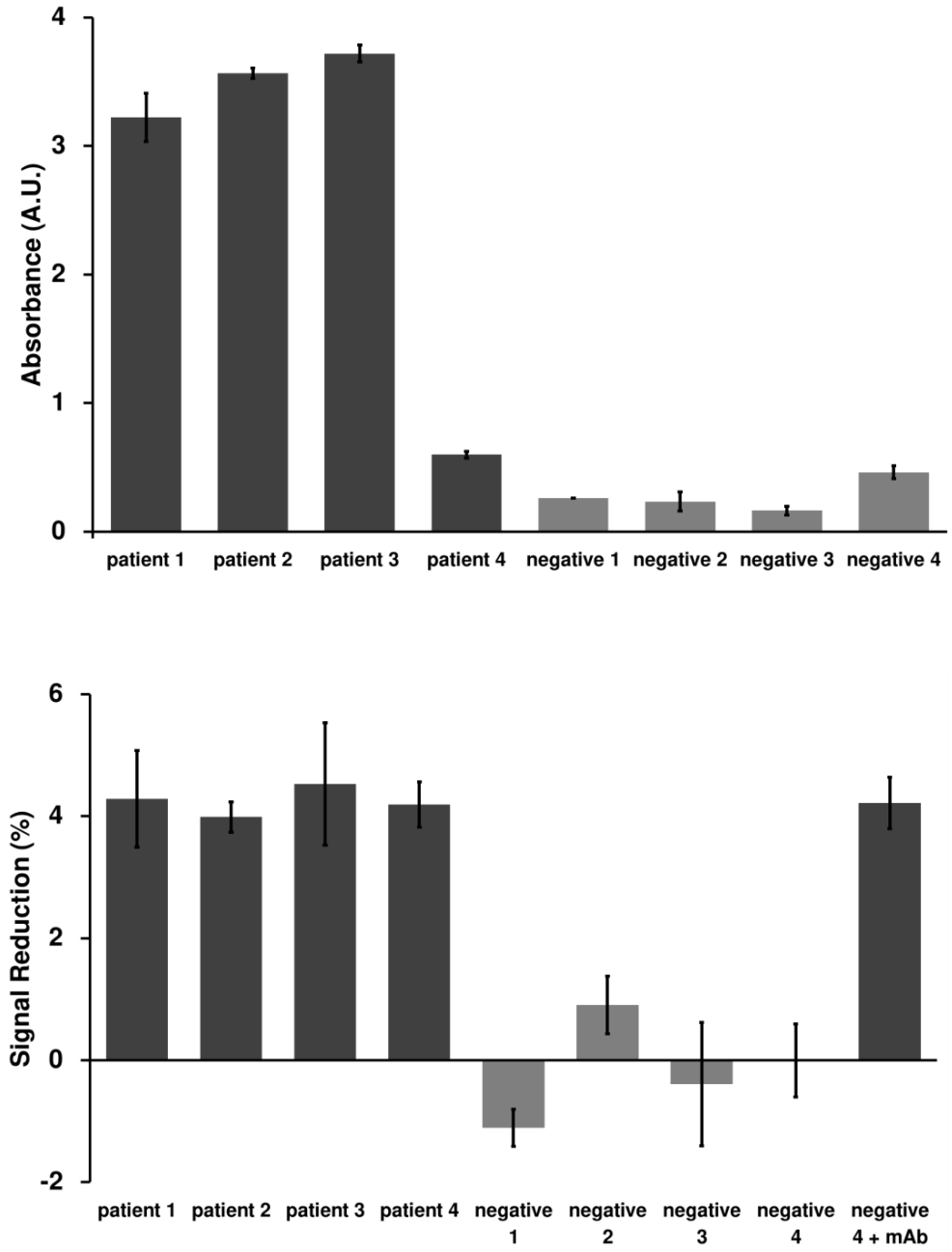

Figure 6. The E-DNA platform can detect endogenous anti-syphilis antibodies in syphilis-positive human serum with clinical sensitivity comparable to that of a commercial ELISA. (a) We performed an ELISA on human serum samples according to the manufacturer's instructions in order to verify the infection status of our samples and controls. While patient four responded relatively weakly for a positive sample and negative four responded strongly for a negative sample, both fell within the appropriate cutoff values as defined by the standard samples provided in the ELISA kit. Error bars represent the standard deviation of three measurements. (b) We then measured the same four patients and four negative controls utilizing our scaffold sensor and were able to detect antibodies in all four samples, including a low-titer sample (patient 4). A positive control comprised of 100 nM monoclonal antibody spiked into a negative sample (negative 4) presents, as expected, as positive. The values presented represent the signal change after 10 min exposure, while the error bars represent the standard deviation of five independently manufactured sensors.

Materials and Methods

Gene design, overexpression, and protein purification:

We retrieved the nucleotide sequence encoding residues 33-156 of Treponema pallidum TpN17 (residue numbering from UniProt entry P29722) from the European Nucleotide Archive (accession ID M74825). We introduced a hexahistidine tag and two serine residues on the amino terminus for purification purposes, substituted Cys58 with Ser (leaving a unique cysteine at position 42), and codon optimized for overexpression in Escherichia coli, yielding the gene sequence:

ATGCACCACCACCACCACCACAGCAGCGGCAAGGCGAAAGCGGAGAAGGTGGA
ATGCGCGCTGAAAGGTGGCATTTTCCGTGGTACCCTGCCGGCGGCGGACAGCCC
GGGTATTGATACCACCGTGACCTTTAACGCGGACGGCACCGCGCAGAAGGTTGA
GCTGGCGCTGGAAAAGAAAAGCGCGCCGAGCCCGCTGACCTACCGTGGTACCT
GGATGGTTCGTGAGGACGGCATCGTGGAACTGAGCCTGGTTAGCAGCGAGCAA
AGCAAGGCGCCGCACGAGAAAGAACTGTACGAACTGATTGATAGCAACAGCGT
GCGTTATATGGGTGCGCCGGGTGCGGGCAAGCCGAGCAAAGAGATGGCGCCGT
TCTATGTTCTGAAGAAAACCAAGAAATAA.

Codon optimization, synthesis, subcloning into a pET-3a vector using 5′ Nde1 and 3′ BamH1 restriction sites, and sequencing of the final construct was performed by a commercial vendor (GenScript, USA).

We transformed the expression construct into E. coli BL21(DE3) cells (New England Biolabs, USA) using standard heat shock. Gene overexpression was for 5 h in lysogeny broth with 100 μg/mL of carbenicillin at 37°C, 220 rpm, induced by addition of 0.5 mM isopropyl β-D-1-thiogalactopyranoside at OD600 > 0.5. Cells were harvested by centrifugation and resuspended in 20 mM sodium phosphate, 40 mM imidazole, 500 mM NaCl, pH 7.4. Protein purification was at 4° C. Cells were lysed by ultrasonication in presence of DNase (Sigma-Aldrich, USA) and RNase (Roche, Switzerland). Cell debris was removed by centrifugation at 11,000 rpm for 1 h. TpN17 was purified from the 0.2-μm-filtered supernatant on a HisTrap HP column (GE Life Sciences, USA), eluting the protein via a linear imidazole gradient up to 500 mM. Pure TpN17 fractions were identified on SDS-PAGE gels by SafeStain staining (Thermo Fisher, USA) and dialyzed into 1x phosphate buffered saline (PBS), pH 7.4 (Sigma-Aldrich, USA), and protein concentration was determined by UV/visible spectroscopy.

Sensor fabrication:

Gold disc electrodes (2 mm diameter) were first mechanically polished in both a 1 μm diamond and a 0.05 μm aluminum oxide slurry, followed by electrochemical cleaning by successive cycling in both 0.5 M NaOH and 0.5 M H2SO4. An anchor DNA strand which had been thiol and methylene blue (MB) modified (HS(CH2)6-CAG TCA GTC AGT CAG TCA GTC AGT-MB)) was reduced in a 10 mM TCEP solution for 1 h before being diluted to a working concentration of 16 nM in 1xPBS. The DNA sequence used for the anchor strand is the same as our group has used previously for other scaffold-type sensors20-24. We originally chose this sequence because it was predicted not to interact with itself, thus

preventing binding of the complement strand, and our group's success using this sequence as an anchor strand supports this prediction. Electrodes were incubated in the DNA anchor solution for 1 h and then rinsed briefly with deionized water. We next coated any remaining exposed gold on the electrode with a protective alkane-thiol monolayer by immersing them in a 10 mM solution of 6-mercapto-1-hexanol overnight at 4° C.

Successful deposition of both the monolayer and anchor strand was confirmed by placing the electrodes in a 1x PBS solution and measuring the methylene blue reduction peak with square wave voltammetry using a 25 mV, 60 Hz, signal. A nitrilotriacetic acid (NTA)-modified complimentary DNA strand was then diluted to 100 nM and the electrodes incubated in this solution for 30 min. Binding of the complementary DNA was verified by measuring the reduction in magnitude of the MB peak. Following this, TpN17 was bound to the assembled scaffold using a His-NTA complex. The electrodes were incubated in a 100 µM $CuSO_4$ solution in 1x PBS for 15 min. After this, a 15 µL drop of 10 µM His-tagged TpN17 was placed on the tip of the electrode and incubated for 45 min. The resulting sensors were rinsed, and the attachment of the protein verified by again scanning using square wave voltammetry.

Electrochemical measurements:

Comparative measurements of the anchor strands were performed in 1x PBS buffer. We prepared three electrodes for each of our constructs (DNA/DNA, PEG-DNA/DNA, DNA/PNA). Prior to depositing the anchor strand, we determined the surface area of each electrode by immersing the electrodes into 0.05 M H_2SO_4 and measuring the area the gold

oxide reduction peak. After depositing the anchor strands and forming the alkane-thiol monolayer, we used square wave voltammetry (60 Hz, 25 mV signal) to measure the methylene blue reduction peak of each construct, using a linear baseline subtraction to account for any current difference between the more positive and more negative sides of the potential window. We then measured the signal reduction after adding in the complementary NTA-labeled oligonucleotide for each electrode as well as the signal reduction due to the addition of the TpN17 protein. Finally, we added 100 nM of mouse monoclonal anti-TpN 17 antibodies (Clone B1707M, Catalog # MBS319589, MyBioSource, USA) in order to verify that the signal change due to saturating antibody concentrations remained constant amongst all of the sensor constructs.

As with the anchor strand measurements, we performed the antibody titrations in 1x PBS. We began by measuring the baseline methylene blue peak current for three electrodes. Monoclonal antibodies were then added every subsequent 20 min and the reduction in peak current measured. In order to verify that the signal change was not due to degradation of the sensor over time, three additional electrodes were prepared and measurements in 1x PBS (without the addition of antibodies) were performed contemporaneously with the titration measurements.

For measurements of clinical samples, human serum samples for both healthy and syphilis positive patients were obtained from a commercial source (Bioreclamation IVT, USA). The infection status of each of the positive patients was confirmed via a rapid plasma regain test by the vendor. Serum measurements were performed by first diluting samples into their

appropriate buffers and then placing sensors in a dilute serum solution and immediately beginning to scan using square wave voltammetry at a 25 mV amplitude and 30 Hz. ELISAs (Zeus Scientific, USA) were purchased and measurements performed according to manufacturer's instructions.

Discussion

Here we have shown that an E-DNA scaffold sensor employing a near-full-length antigen as its recognition element can detect diagnostically relevant antibodies at clinically relevant concentrations in human serum samples. Despite the relatively large size of the antigenic protein it employs, this new treponemal test easily differentiates syphilis positive human serum samples from those of healthy control patients in as little as ten minutes via a simple assay that requires no reagents other than the dilution buffer. The clinical sensitivity of the test compares favorably to that a commercially available ELISA, one of the current gold standards for serological diagnosis of syphilis, while taking a fraction of the time (minutes as opposed to hours) and being far less complex (far fewer steps) to perform.

Given that not all patients will produce antibodies against any single epitope and that many antibodies recognize conformational rather than linear epitopes, the use of a folded antigen as our recognition element expands the potential range of diseases that can be diagnosed using sensors in this class and opens the door for a more general platform which can be used to adapt established clinical assays into point-of-care tests. This increase in generality, however, comes at the cost of signal gain. Working in buffer solutions we have previously established that recognition elements up to ~25 kDa in size can produce appreciable signal change upon binding. While our results in buffer are in line with this observation, our results from serum samples lead us to believe that biofouling and the associated loss in signal change might reduce the maximum possible size of the recognition element for scaffold sensors operating in complex media closer to 15 kDa, although a more rigorous study of this

effect would be needed. Even with this restriction in mind, this proof of principle opens the door to a wide range of potentially useful full-length and near full-length antigen E-DNA sensors based off of this platform, and the precise molecular-weight-limit is likely to depend on the specific geometry of the antibody-antigen complex.

References

(1) Gift, T.; Pate, M.; Hook, E.; Kassler, W. Ovid: The Rapid Test Paradox: When Fewer Cases Detected Lead to More Cases Treated: A Decision Analysis of Tests for Chlamydia trachomatis.

(2) Huang, W.; Gaydos, C. A.; Barnes, M. R.; Jett-Goheen, M.; Blake, D. R. Comparative Effectiveness of a Rapid Point-of-Care Test for Detection of *Chlamydia Trachomatis* among Women in a Clinical Setting. *Sexually Transmitted Infections* **2013**, *89* (2), 108–114.

(3) Swain, G. R.; McDonald, R. A.; Pfister, J. R.; Gradus, M. S.; Sedmak, G. V.; Singh, A. Decision Analysis: Point-of-Care Chlamydia Testing vs. Laboratory-Based Methods. *Clinical Medicine & Research* **2004**, *2* (1), 29–35.

(4) Huppert, J.; Hesse, E.; Gaydos, C. A. What Is the Point? How Point-of-Care Sexually Transmitted Infection Tests Can Impact Infected Patients: *Point of Care: The Journal of Near-Patient Testing & Technology* **2010**, *9* (1), 36–46.

(5) Gaydos, C.; Hardick, J. Point of Care Diagnostics for Sexually Transmitted Infections: Perspectives and Advances. *Expert Review of Anti-infective Therapy* **2014**, *12* (6), 657–672.

(6) Cortez, K. J.; Greenwald, M. A. Current Trends in Donor Testing to Detect Syphilis Infection. *Current Infectious Disease Reports* **2014**, *16* (9).

(7) Syphilis - 2016 STD Surveillance Report

(8) Morshed, M. G.; Singh, A. E. Recent Trends in the Serologic Diagnosis of Syphilis. *Clinical and Vaccine Immunology* **2015**, *22* (2), 137–147.

(9) Soreng, K.; Levy, R.; Fakile, Y. Serologic Testing for Syphilis: Benefits and Challenges of a Reverse Algorithm. *Clinical Microbiology Newsletter* **2014**, *36* (24), 195–202.

(10) Falcone, V. H.; Stout, G. W.; Jr., M. B. M. Evaluation of Rapid Plasma Reagin (Circle) Card Test. *Public Health Reports (1896-1970)* **1964**, *79* (6), 491.

(11) Ratnam, S. The Laboratory Diagnosis of Syphilis. *Can J Infect Dis Med Microbiol* **2005**, *16* (1), 45–51.

(12) Sexually Transmitted Diseases Treatment Guidelines 2010. *59*, 116.

(13) Larsen, S. A.; Steiner, B. M.; Rudolph, A. H. Laboratory Diagnosis and Interpretation of Tests for Syphilis. *CLIN. MICROBIOL. REV.* **1995**, *8*, 21.

(14) Seña, A. C.; White, B. L.; Sparling, P. F. Novel *Treponema Pallidum* Serologic Tests: A Paradigm Shift in Syphilis Screening for the 21st Century. *Clinical Infectious Diseases* **2010**, *51* (6), 700–708.

(15) Park, B. G.; Yoon, J. G.; Rim, J. H.; Lee, A.; Kim, H.-S. Comparison of Six Automated Treponema-Specific Antibody Assays. *Journal of Clinical Microbiology* **2016**, *54* (1), 163–167.

(16) Dicker, L. W.; Mosure, D. J.; Steece, R.; Stone, K. M. Testing for Sexually Transmitted Diseases in U.S. Public Health Laboratories in 2004: *Sexually Transmitted Diseases* **2007**, *34* (1), 41–46.

(17) Schoukroun-Barnes, L. R.; Macazo, F. C.; Gutierrez, B.; Lottermoser, J.; Liu, J.; White, R. J. Reagentless, Structure-Switching Electrochemical Aptamer-Based Sensors. *Annu Rev Anal Chem (Palo Alto Calif)* **2016**, *9* (1), 163–181.

(18) Cao, C.; Zhang, F.; Goldys, E. M.; Gao, F.; Liu, G. Advances in Structure-Switching Aptasensing towards Real Time Detection of Cytokines. *TrAC Trends in Analytical Chemistry* **2018**, *102*, 379–396.

(19) Mettakoonpitak, J.; Boehle, K.; Nantaphol, S.; Teengam, P.; Adkins, J. A.; Srisa-Art, M.; Henry, C. S. Electrochemistry on Paper-Based Analytical Devices: A Review. *Electroanalysis* **2016**, *28* (7), 1420–1436.

(20) Cash, K. J.; Ricci, F.; Plaxco, K. W. An Electrochemical Sensor for the Detection of Protein−Small Molecule Interactions Directly in Serum and Other Complex Matrices. *Journal of the American Chemical Society* **2009**, *131* (20), 6955–6957.

(21) Cash, K. J.; Ricci, F.; Plaxco, K. W. A General Electrochemical Method for Label-Free Screening of Protein–Small Molecule Interactions. *Chemical Communications* **2009**, No. 41, 6222.

(22) White, R. J.; Kallewaard, H. M.; Hsieh, W.; Patterson, A. S.; Kasehagen, J. B.; Cash, K. J.; Uzawa, T.; Soh, H. T.; Plaxco, K. W. Wash-Free, Electrochemical Platform for the Quantitative, Multiplexed Detection of Specific Antibodies. *Analytical Chemistry* **2012**, *84* (2), 1098–1103.

(23) Bonham, A. J.; Paden, N. G.; Ricci, F.; Plaxco, K. W. Detection of IP-10 Protein Marker in Undiluted Blood Serum via an Electrochemical E-DNA Scaffold Sensor. *The Analyst* **2013**, *138* (19), 5580.

(24) Kang, D.; Parolo, C.; Sun, S.; Ogden, N. E.; Dahlquist, F. W.; Plaxco, K. W. Expanding the Scope of Protein-Detecting Electrochemical DNA “Scaffold” Sensors. *ACS Sensors* **2018**, *3* (7), 1271–1275.

(25) Olson, W. K.; Gorin, A. A.; Lu, X.-J.; Hock, L. M.; Zhurkin, V. B. DNA Sequence-Dependent Deformability Deduced from Protein–DNA Crystal Complexes. *PNAS* **1998**, *95* (19), 11163–11168.

(26) Smilgies, D.-M.; Folta-Stogniew, E. Molecular Weight–Gyration Radius Relation of Globular Proteins: A Comparison of Light Scattering, Small-Angle X-Ray Scattering and Structure-Based Data. *J Appl Cryst* **2015**, *48* (5), 1604–1606.

(27) Uzawa, T.; Cheng, R. R.; White, R. J.; Makarov, D. E.; Plaxco, K. W. A Mechanistic Study of Electron Transfer from the Distal Termini of Electrode-Bound, Single-Stranded DNAs. *J. Am. Chem. Soc.* **2010**, *132* (45), 16120–16126.

(28) Bard, A. *Electrochemical Methods: Fundamentals and Applications*, 2nd ed.; Wiley.

(29) Malm, K.; Andersson, S.; Fredlund, H.; Norrgren, H.; Biague, A.; Månsson, F.; Ballard, R.; Unemo, M. Analytical Evaluation of Nine Serological Assays for Diagnosis of Syphilis. *Journal of the European Academy of Dermatology and Venereology* **2015**, *29* (12), 2369–2376.

(30) Marangoni, A.; Sambri, V.; Accardo, S.; Cavrini, F.; D'Antuono, A.; Moroni, A.; Storni, E.; Cevenini, R. Evaluation of LIAISON Treponema Screen, a Novel Recombinant Antigen-Based Chemiluminescence Immunoassay for Laboratory Diagnosis of Syphilis. *Clinical and Vaccine Immunology* **2005**, *12* (10), 1231–1234.

(31) Brautigam, C. A.; Deka, R. K.; Liu, W. Z.; Norgard, M. V. Insights into the Potential Function and Membrane Organization of the TP0435 (Tp17) Lipoprotein from Treponema Pallidum Derived from Structural and Biophysical Analyses. *Protein Science* **2015**, *24* (1), 11–19.

(32) Eriksson, M.; Nielsen, P. E. Solution Structure of a Peptide Nucleic Acid–DNA Duplex. *Nature Structural Biology* **1996**, *3* (5), 410.

IV. Towards the rational optimization of aptamers for electrochemical sensors

Introduction

Aptamers are short (typically 20 to 70 bases), oligonucleotides that are capable of binding to a non-nucleic acid target such as a protein or small molecule[1,2]. Typically, they have regions of self-complementary bases which help define a three-dimensional structure able to bind to the target of interest[3–5]. In the absence of target, however, the three-dimensional structure is often unstable, leading to a phenomenon where aptamers can undergo large conformational changes between the "bound" and "unbound" states. A major recent advance in sensing has been to take advantage of these conformational changes to couple target binding with an easily measurable output[6–13]. One such method is to modify the aptamer with a redox active "reporter", such as methylene blue (MB), and then tether the aptamer to an electrode. In the unbound state, the aptamer is unfolded and the redox reporter is far from the surface, resulting in slow electron transfer when interrogated. In the presence of target, however, the

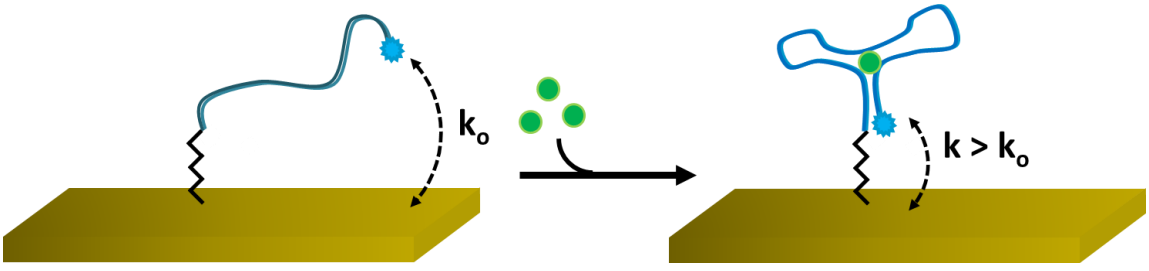

Figure 1. Cartoon schematic showing the basic operation of an electronic aptamer based sensor. In the absence of target, the aptamer is in an unstructured state and the average electron transfer rate between the methylene blue molecule and the surface is low. In the presence of target, however, the aptamer's structure is stabilized, bringing the methylene blue closer to the surface and increasing the electron transfer rate. This change in electron transfer rate can be measured using standard electrochemical methods such as square wave voltammetry or chronoamperometry

three-dimensional structure is stabilized, locking the redox reporter into a position closer to the surface and thereby increasing the electron transfer rate [Figure 1].

While this modification strategy sounds simple in concept, not all aptamers are amenable to being transformed into a sensor in such a fashion. It is, therefore, common practice upon receiving a new aptamer sequence to then "engineer" it for use as a sensor[14,15]. Depending on the structure of the folded state, it may be necessary to move the redox reporter to different locations along the aptamer in order to maximize the difference in electron transfer rate between the two states. Alternatively, a researcher might find that the folded state is stable when conjugated to the surface, reducing the signal change seen upon target binding. In this case, a researcher may choose to truncate complementary regions in the aptamer in order to destabilize it or to split the aptamer in two connected with a flexible linker[16–18]. As another strategy, a researcher might attempt to add non-complementary bases before or after complementary regions in order to shift the entire aptamer away from the surface[15]. This may be done for several reasons, including attempting to engineer a larger difference in electron transfer rate between the bound and unbound states, attempting to move the binding pocket away from the surface and therefore give it greater access to the analyte, and attempting to minimize disruptive surface effects on the aptamer. A major challenge when developing aptamer-based sensors is therefore determining which modifications to make to the aptamer in order to maximize the difference between the electron transfer rates of the bound and unbound states without sacrificing affinity for the target.

While “engineering” implies a careful and scientific approach, in reality this process is semi-(or fully) empirical. Specifically, there has been little effort to systematically explore and understand the physical effects of any of these modifications. Rather, individual researchers typically just order and test a variety of constructs then select the best performing varient. While this may make sense on an individual level, it would be preferable in the long term to construct a predictive model capable describing the effects of aptamer modifications on sensor behavior. Unfortunately, developing a complete model of an aptamer interacting with its target is an difficult. Given the vast diversity of possible aptamer targets, including everything from small molecule drugs weighing a few dozen daltons to proteins weighing nearly one hundred kilodaltons, there is no single computational method appropriate for simulating the interaction of a generic aptamer with its target. Indeed, if such a model was available, it would be possible to perform aptamer selection completely *in-silico,* rendering traditional methods entirely unnecessary. Here, instead, we will focus on the much more acheivalbe task of isolating one possible modification strategy, in this case the addition of non-complementary bases on the 3’ and 5’ ends of the aptamer, and simulating the resulting effect on the electron transfer rate of the aptamer in its bound and unbound states.

Results

In order to compare the bound versus the unbound states, we have constructed a kinetic Monte Carlo model of a "generic" aptamer system. The model divides our simulation into two separate programs, one which addresses the behavior of the unfolded state and one which addresses the behavior of the folded state. In doing so, we can compare the behavior of the aptamer in the absence of any target and in the presence of saturating amount of target. Here we are making the implicit assumption that the folded structure is sufficiently unstable in the absence of target that no aptamers are in this conformation unless stabilized by the target. Likewise, we assume that the folded state is sufficiently stable such that in the presence of saturating amounts of target the bound state will retain its structure over time periods significantly longer than the amount of time being simulated (the timescale of the simulations, which is defined by the slower electron transfer rate, is typically of the order of seconds). While with real sensors we will never experience a situation where *all* of the aptamers on a surface are in the bound or unbound conformations, optimizing the difference in electron transfer rate between these two states remains the best way to maximize signal gain. Additionally, despite not entirely representing the conditions on the sensor surface, these assumptions are in good agreement with empirical observations of the aptamer systems which our lab has encountered thus far. For instance, one available aptamer explored by our group is an aptamer against the chemotherapy drug doxorubicin. If we interrogate a surface bound doxorubicin aptamer with square wave voltammetry, can graph a Lovric plot showing the peak electric charge versus the applied frequency, which gives us a rough estimate of the distribution of electron transfer frequencies for the doxorubicin

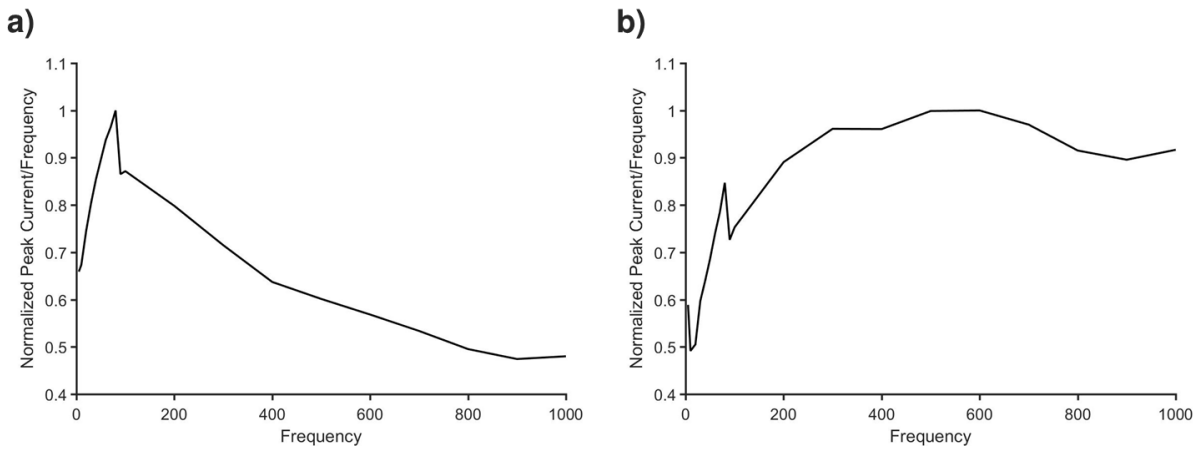

Figure 2 Lovric plots of the doxorubicin aptamer show the distribution of electron transfer rates in our system. Shown here are plots in the absence of target (a) and presence of saturating amounts of target (b). We see two distinctly different distributions, indicating that each state has distinct electron transfer behavior. It should be noted that the sudden signal drop around 100 Hz is due to an equipment artifact.

aptamer [Figure 2]. After adding 100 µM of doxorubicin, we can clearly see that both the bound and unbound states have distinctly different peak electron transfer rates. This indicates that there is minimal contribution from unfolded and folded states respectively and that we may safely divide our task into two separate programs.

We gain several advantages by dividing the simulation into models of the two distinct states, chiefly in being able to greatly simplify each model. First, we do not need to add specific logic to address the interaction of the target with the aptamer. This is a poorly studied field and, to our knowledge, there are only a few DNA aptamer/target pairs which have been studied with crystallography[19–24]. Thus, due to our dividing of the models, we can avoid all uncertainties related to whether the target interacts with the bound or unbound stage, what specific orientation of the target relative to the aptamer is needed in order to bind, et cetera, while still being able to extract useful information for optimizing other aspects of the aptamer design. This simplification also allows us to avoid explicitly modeling base-pair

interactions, a time and resource intensive task with little bearing on the modification strategy being considered. Instead, we can "fix" the conformation of certain base pairs to ensure they are properly hydrogen bonded. We then assume that the rest of the bases do not interact.

With our general strategy in mind, we begin by examining the simpler problem, modeling the unbound, unfolded state. This consists of a single strand of DNA anchored to a surface and with a redox reporter conjugated to the last base. We will use a similar Monte Carlo approach as described in the previous chapter, albeit with modifications to reflect our current system. To initialize the system, we start the simulation in the lowest possible energy state, a strand of DNA of length ***n*** bases that extends straight up from the surface. For a set number of steps, we apply a small deviation to the position of each of the ***n*** bases and calculate the energy associated with such a deviation. These deviations are made in spherical coordinates relative to the reference frame of the base previous and the magnitude is chosen such that the bend energy equilibrates around $\frac{3}{2}k_BT$. Here we model the DNA as a freely jointed chain which has a bending energy given by:

$$E_{FJC} \cong k_BT\left(\frac{L_p}{L_b}\right)(1-\cos(\phi))$$

where L_p is the persistence length of single stranded DNA (~2.2 nm), L_b is the length per base (~0.676 nm) [ref[25]] and ϕ is the bend angle between two bases. If the change in energy associated with the move is less than zero, the deviation for that base is accepted, while if the energy is greater than zero the change is accepted with a probability

$$P = e^{\frac{\Delta E}{k_BT}}$$

We then update the global position of all the bases based off of the spherical coordinates of each base calculated relative to the previous base. This process proceeds in much the same fashion as described in the previous chapter. We model the self-assembled monolayer on the surface of our electrode as a hard exclusion zone lying on the z = 0 plane. After updating the positions, we check that all the bases lie above this plane and, if not, we attempt to resolve this conflict by relaxing the most recent deviation to the system. The program recalculates the positions with a deviation 95% of the magnitude of the original deviation and then rechecks for bases lying below the monolayer. This process is repeated iteratively until no conflicts are observed. Once we have achieved this, we calculate the effects of the electric potential of the surface on the DNA. Here we treat the electric potential as a decaying exponential due to screening of the applied voltage by electrolytes in solution:

$$V(z) = V_0 e^{-\frac{z}{\kappa}}$$

where V_0 is the voltage at the surface, equal to the reduction potential of methylene blue (-0.35 V), and κ is the Debye length in a 150 mM electrolyte solution (~0.785 nm). We then calculate a $\Delta U_{electrostatic}$ for each base based off the proposed position of the DNA bases compared to the starting position of the DNA bases. Based off this second energy calculation, we then use the Monte Carlo algorithm to reevaluate whether to accept or reject the change in position.

Once we have iterated through each DNA base in this fashion, we have completed one step in the Monte Carlo algorithm and have a new conformation for our DNA. These Monte Carlo steps do not inherently give us any information about the amount of time which has elapsed, however, making it impossible to calculate an electron transfer rate. In order to

account for this, we introduce the "kinetic" portion of our kinetic Monte Carlo algorithm. In order to do so, we assign time values to each of our steps by measuring the distance that the terminal base has traveled. We then use the diffusion equation to calculate the approximate amount of time it would take to diffuse such as distance:

$$< \Delta x^2 > = 6D\Delta t$$

where *D* is the length dependent diffusion rate of single stranded DNA as empirically measured by Robertson et al.[26]:

$$D = 3.096 * 10^{-8}(N_{bases})^{-0.571}$$

here the diffusion rate is given in units of $\frac{nm^2}{s}$ and N_{bases} is the length of the single stranded DNA. We then can determine whether an electron was transferred between the redox reporter and the surface by calculating the distance between the last base (which we assume to hold the redox reporter) and the surface. We calculate the probability of an electron being transferred as the amount of time elapsed multiplied by the probability of an electron being transferred in that conformation according to a 1-D long distance tunneling equation:

$$P_{eT} = k_{eT}\Delta t = 4400e^{-1.2*z_{redox}}\,\Delta t$$

where we have chosen the prefactors for the tunneling equation in accordance with experimental values for methylene blue in 150 mM phosphate buffered saline[27].

For the structured, bound aptamer state, we use a modified version of the single stranded DNA algorithm. Instead of inputting a single overall aptamer length, we now have two inputs, a "stem" length and a "tail" length corresponding to the number of bases added at the 3' or 5' end before and after the double stranded region of the structured aptamer. It should be noted that the model does not explicitly address the structure of the "loop" portion of the

aptamer. We believe this to be an acceptable generalization because, since the loop portion of the aptamer must begin and end connected to the same double stranded portion of the aptamer, the final position of the methylene blue is not affected by the conformation of the loop or the interaction of the target with the aptamer. Thus, we only have to simulate the region around the stem of the aptamer and can avoid explicitly simulating the loop. To demonstrate this experimentally, we once again turn to measuring the electron transfer rate of the doxorubicin aptamer, this time with varying lengths of poly-thymine introduced in the loop portion of the aptamer. After inserting either 10 or 30 thymine bases in the loop portion of the aptamer, we see that the electron transfer rate of the bound state stays the same while the electron transfer rate of the unbound state decreases as the aptamer is made longer [Figure 3]. This simplification allows us to avoid explicitly addressing the interaction of the target with the binding pocket in our simulation. Instead, we proceed in much the same fashion as the single stranded simulation up to the length of the stem portion. Once the algorithm reaches the final ‘stem” base, it then calculates the position of a complementary base, which is assigned as the position of the first “tail” base. The algorithm then continues; now calculating distances in the opposite direction, until it reaches the final “tail” base. In doing so, we can calculate the position of the final base, and therefore the redox reporter, without explicitly calculating the position of the loop. The diffusion constant is calculated as the harmonic mean between the diffusion constant of a section double stranded DNA whose length corresponds to the length of the unmodified aptamer and the diffusion constant of the single stranded additions made to the aptamer before and after the stem-loop.

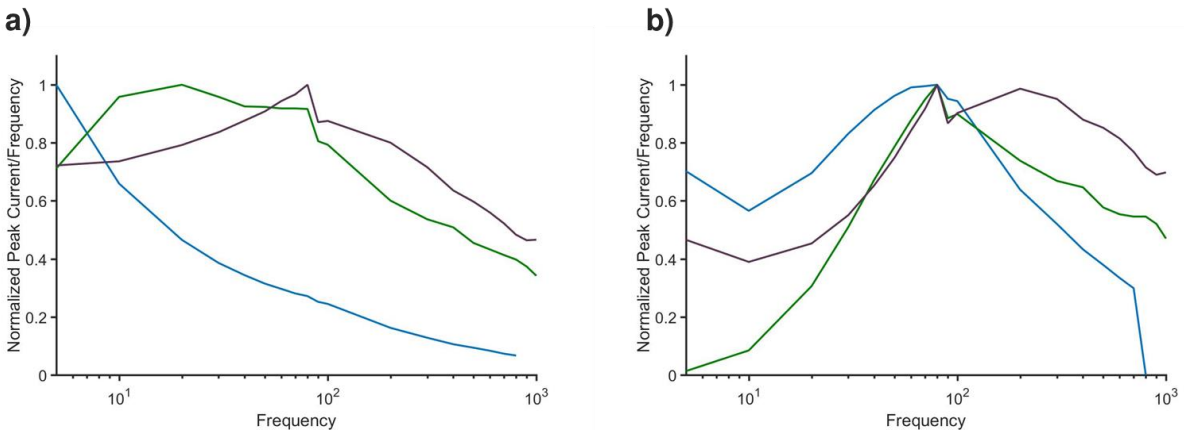

Figure 3 (a) Lovric plots of the doxorubicin aptamer with varying lengths of poly-T inserted in the loop portion of the aptamer show that in the absence of target the electron transfer rate slows as the aptamer is lengthened. Here purple is the native aptamer, green is the aptamer with 10 thymine bases inserted, and blue is the aptamer with 30 thymine bases inserted. (b) While changing the loop portion of the aptamer predictably causes large changes in the electron transfer rate, in the folded state we see little difference between the native aptamer (purple), the aptamer with 10 poly-T (green), and with 30 poly-T (blue).

We find that our Monte Carlo model is able to correctly predict the relationship between the electron transfer rate for varying lengths of single stranded DNA. We predict that the electron transfer rate should scale with the length of the aptamer with a power law dependence of -1.61 ± 0.39 while experimental data shows a power law dependence of -2.2 ± 0.3 [ref[28]]. These results are within the margin of error of one another, indicating that our model is able to sufficiently describe the behavior of the open state [Figure 4].

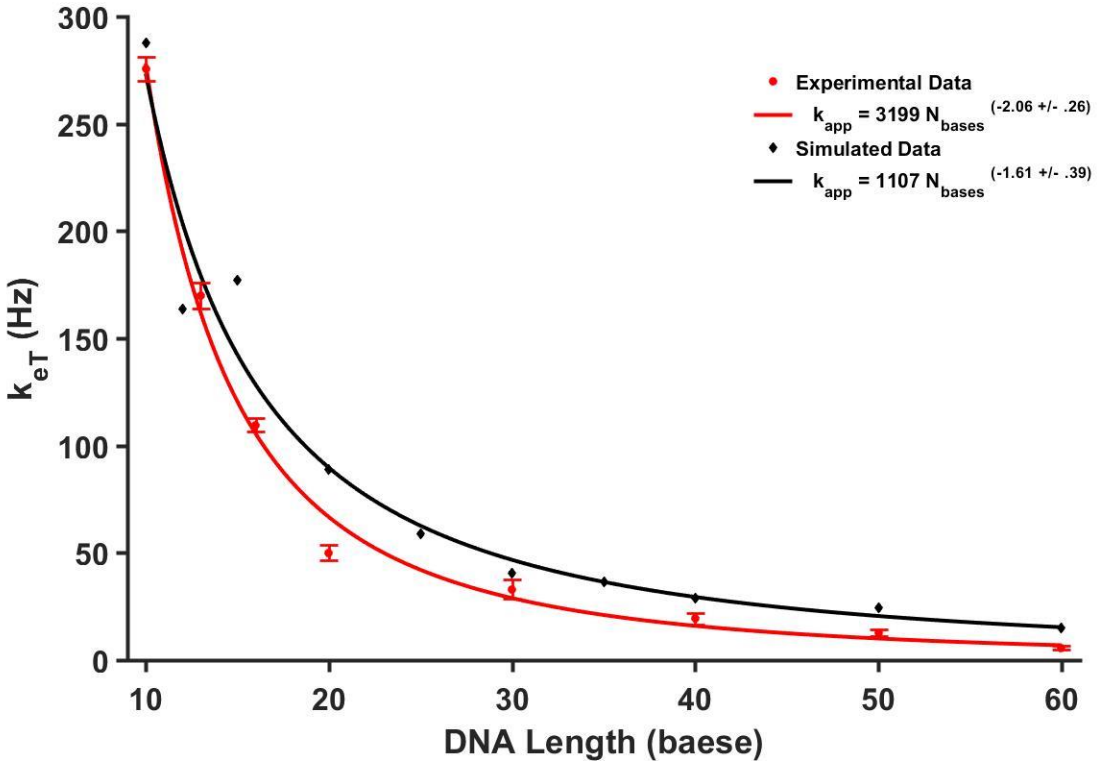

Figure 4 A comparison of the simulated electron transfer rate (black) with data measured via chronoamperometry (red) shows good agreement between our model and experimental results for unstructured, unbound, DNA

For the closed state of the "aptamer", we chose to investigate the effects of adding bases before and after the stem portion of the aptamer. This one of several strategies employed in engineering aptamers in an attempt to improve signal gain. The expectation is that while this will move the binding pocked farther from the surface, potentially allowing the aptamer to better bind with its target, it will also lead to slower electron transfer in the bound state. Since the signal change is dependent on the difference between the states, however, it is possible to achieve better overall performance despite slower rates in the closed state as long as the electron transfer rate of the open state decreases more quickly than that of the closed state. Specifically, we will examine one modification strategies in which we add bases both

before and after the stem with the goal of balancing out the detrimental effect of adding bases before the stem.

From the simulations, we see a noticeable difference between the symmetric and asymmetric cases. Plotted below is the simulated electron transfer rate for the unfolded state versus the electron transfer rate of asymmetrically and symmetrically modified aptamers with a 25-base loop [Figure 5]. As further bases are added around the stem, it increases the length of the aptamer in the unfolded state as well. It is therefore possible to gain a rough estimate of the performance of an aptamer construct by drawing a vertical line at a given total base length and taking the difference between the electron transfer rate of the unfolded state and one of the two competing folded states. Because the model assumes one base is present after the stem loop, we see that initially the symmetric and asymmetric cases are the same and only differ slightly due to noise arising from the random fluctuations due to the nature of the Monte Carlo simulation. As the number of additional bases grows, however, we see that the electron transfer rate of the asymmetric case falls off more rapidly than the symmetric case, likely due to the symmetric case allowing for more states where the redox reporter is able to approach the surface. Eventually, however, the gap between the asymmetric and symmetric

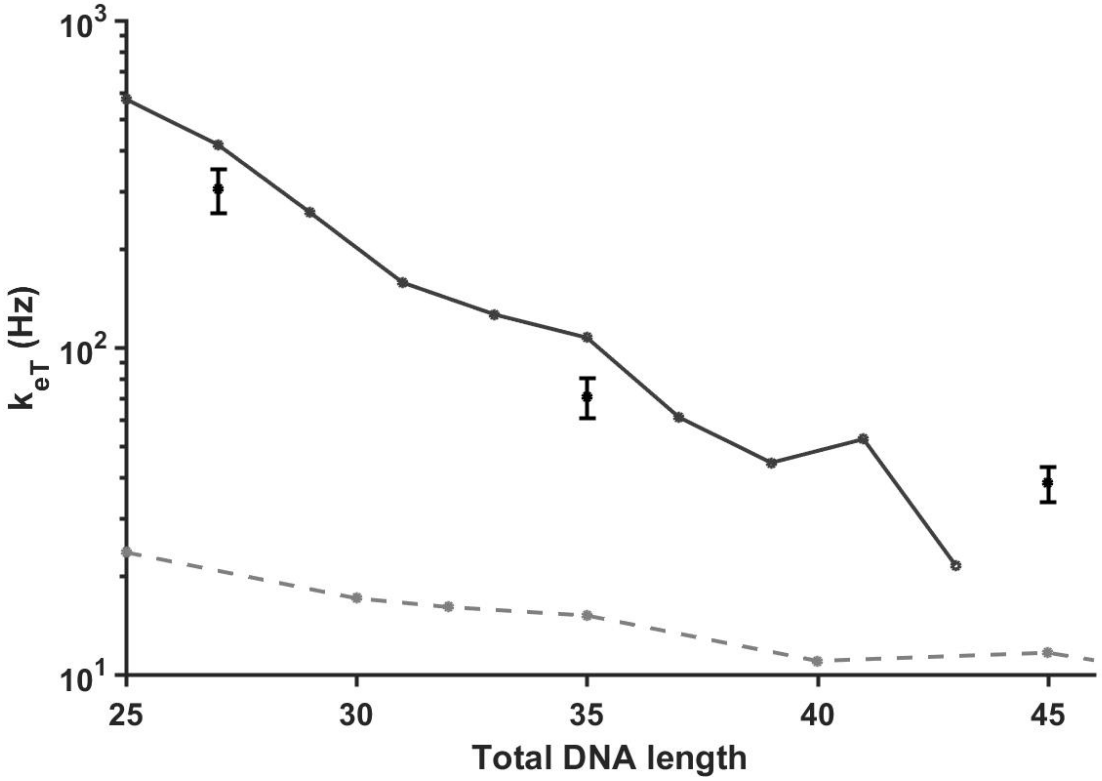

Figure 5. As we add bases to the stem loop, we see that regardless of modification strategy the electron transfer rate of the closed state falls off faster than the electron transfer rate of the open state. Here the dotted line represents the simulated electron transfer rate of an aptamer in the unbound state, while the solid line represents the electron transfer rate of the bound state. Experimental date is shown as solid dots where the error bars represent the uncertainty of the exponential decay fit.

states narrows before vanishing all together after adding approximately 16 bases to the original stem-loop. It is worth noting that the electron transfer rate of both cases decreases faster than that of the unfolded aptamer, indicating that all modifications of this sort will have a negative effect on the observed signal change. If a researcher wishes to perform such a modification on their construct for reasons other than changing the electron transfer rate (such as moving the binding pocket away from the electrode surface), then this model advises that such modifications should be kept as short as possible in order to minimize the negative effect they will have on the electron transfer rate.

In order to confirm the accuracy of our model, we ordered a series of stem-loop DNA constructs to stand in for a generic "aptamer". Each construct maintained the same 25-base "structured" region consisting of 5 complementary bases forming the stem with 15 non-complementary bases forming the loop. The sequence itself was chosen off past studies which have shown this sequence to be highly stable at room temperature[29]. We then added varying numbers of thymine bases on either the 3' or on the 3' and 5' ends of the stem in a manner consistent with simulated structure from our Monte Carlo model. We measured the electron transfer rate for each sequence using chronoamperometry and compared it against the electron transfer rate of the simulated model [Figure 5]. We found our experimental results to be in good agreement with the simulations, thus validating our approach.

Materials and Methods

Simulations:

Simulations were performed using a custom MATLAB script the details of which are given above. The code itself is provided in Appendix B. For each data point, the program was allowed to run until it measured 100 electron transfer events, at which point it reported the total elapsed time. The electron transfer rate was then simply calculated as the number of electrons transferred divided by the elapsed time.

Electrode fabrication:

To confirm the results of our simulation, we performed electrochemical measurements of the electron transfer rate of a step-loop construct. We began by polishing 2 mm diameter gold disc electrodes in a 1 μm diamond slurry followed by polishing in a 0.05 μm aluminum oxide slurry. The electrodes were then electrochemically cleaned by successive cycling in both 0.5 M NaOH and 0.5 M H2SO4. For doxorubicin measurements, we used an aptamer with the following sequence as the parent aptamer: 5' - ACC ATC TGT GTA AGG *n*T GGT AAG GGG TGG T – 3' where *n*T represents varying lengths of poly-thymine. To simulate aptamers in their folded conformation, we conjugated closed stem loops with various modifications made to the 3' and 5' end to our electrodes. The various constructs all contained a thiol group and a methylene blue (MB) modification and followed the same sequence (*n*T- TCG CGC GAT CGG CGT TTT AGC GCG T-*n*T) where *n*T represents varying lengths of poly-thymine. Constructs were reduced in a 10 mM TCEP solution for 1 h then diluted to a concentration of 100 nM in 1xPBS. This sequence was chosen because it

has previously been shown to form stable stem-loops. We incubated the electrodes in the stem-loop solution for 1 h and then rinsed briefly with deionized water. To protect the surface of the electrode, we then immersing them in a 10 mM solution of 6-mercapto-1-hexanol overnight at 4° C, coating any remaining exposed gold on the electrode with an alkane-thiol monolayer.

Electrochemical measurements:

We used Lovric plots were to illustrate the difference between the electron transfer behavior of the bound versus unbound states. To perform these measurements, we scanned electrodes with square wave voltammetry (using a custom script written for a CH instruments potentiostat) for a set number of frequencies and then extracted the peak current observed at each. The Lovric plots were then constructed by dividing the peak current by the frequency being measured. While these measurements are easy to perform and analyze, due to the low frequency resolution of the Lovric plots, we chose to use chronoamperometry to better determine the electron transfer rate of the stem-loop constructs for comparing to our model. For these measurements, after successfully modifying the gold electrodes, we performed a cyclic voltammetry sweep from -0.1 V to -0.4 V in order to confirm the presence of the methylene blue modified DNA on the surface and to determine the precise voltages to be used during the chronoamperometry portion of the experiment. We then began the chronoamperometry sweep with the methylene blue in a fully oxidized state before jumping to a reducing potential as determined by the cyclic voltammetry scan and measuring the resulting current decay. Due to limitations of the instrument, in order to capture the full current decay we performed three measurements at varying sensitivities and used a custom

MATLAB script to reconstruct the full decay [Figure 5]. To reduce noise, each measurement was repeated 50 times and the average current decay was used to extract the electron transfer rate. We fit the portion of the decay corresponding to the methylene blue reduction to a single exponential decay, allowing us to extract the electron transfer rate for each stem-loop construct.

Conclusion

Adapting aptamers to be used in sensors is a laborious and expensive task which depends largely on trial and error. In an attempt to help streamline this task, we have developed a Monte Carlo model which simulates the electron transfer rate of a generic aptamer and examines how modifications to the aptamer might affect the difference in electron transfer rates between the bound and unbound states. To validate our model, we examined how the addition of poly-thymine at the 3' and 5' ends of an aptamer influences the performance of the resulting sensor. Our simulation shows that the addition of poly-thymine reduces the electron transfer rate of the bound state by a larger degree than that of the unbound state. This indicates that such a modification strategy would not improve the performance of a sensor, but rather would actually make it worse. This is backed up by experimental evidence which shows that for a stem-loop construct with varying lengths of poly-thymine added around the 3' and 5' ends we see a similar effect, albeit with far fewer data points to define the shape of the curve.

As electrochemical DNA based sensors mature, it will become increasingly important to understand the physics behind how they work in order to better optimize them for specific applications. While experimental evidence will always be necessary to validate computational models, to perform the full equivalent experiment to our simulations, we would have had to design, purchase, and evaluate approximately 20 DNA sequences. Such a task would have taken weeks to months to complete as opposed to the few hours required to run our program. Thus, while models such as ours cannot entirely replace benchtop

measurements, they can be used to help identify promising paths forwards and help avoid wasting time and resources on unrewarding or unlikely to succeed strategies.

References

(1) Ellington, A. D.; Szostak, J. W. In Vitro Selection of RNA Molecules That Bind Specific Ligands. *Nature* **1990**, *346* (6287), 818–822.

(2) Tuerk, C.; Gold, L. Systematic Evolution of Ligands by Exponential Enrichment: RNA Ligands to Bacteriophage T4 DNA Polymerase. *Science* **1990**, *249* (4968), 505–510.

(3) Dunn, M. R.; Jimenez, R. M.; Chaput, J. C. Analysis of Aptamer Discovery and Technology. *Nat Rev Chem* **2017**, *1* (10), 1–16.

(4) Wilson, D. S.; Szostak, J. W. In Vitro Selection of Functional Nucleic Acids. *Annu. Rev. Biochem.* **1999**, *68*, 611–647.

(5) Jiang, F.; Kumar, R. A.; Jones, R. A.; Patel, D. J. Structural Basis of RNA Folding and Recognition in an AMP–RNA Aptamer Complex. *Nature* **1996**, *382* (6587), 183–186.

(6) Xiao, Y.; Lubin, A. A.; Heeger, A. J.; Plaxco, K. W. Label-Free Electronic Detection of Thrombin in Blood Serum by Using an Aptamer-Based Sensor. *Angew. Chem. Int. Ed. Engl.* **2005**, *44* (34), 5456–5459.

(7) Xiao, Y.; Piorek, B. D.; Plaxco, K. W.; Heeger, A. J. A Reagentless Signal-On Architecture for Electronic, Aptamer-Based Sensors via Target-Induced Strand Displacement. *J. Am. Chem. Soc.* **2005**, *127* (51), 17990–17991.

(8) Baker, B. R.; Lai, R. Y.; Wood, M. S.; Doctor, E. H.; Heeger, A. J.; Plaxco, K. W. An Electronic, Aptamer-Based Small-Molecule Sensor for the Rapid, Label-Free Detection of Cocaine in Adulterated Samples and Biological Fluids. *J. Am. Chem. Soc.* **2006**, *128* (10), 3138–3139.

(9) Rowe, A. A.; Miller, E. A.; Plaxco, K. W. Reagentless Measurement of Aminoglycoside Antibiotics in Blood Serum via an Electrochemical, Ribonucleic Acid Aptamer-Based Biosensor. *Anal. Chem.* **2010**, *82* (17), 7090–7095.

(10) Ferapontova, E. E.; Gothelf, K. V. Effect of Serum on an RNA Aptamer-Based Electrochemical Sensor for Theophylline. *Langmuir* **2009**, *25* (8), 4279–4283.

(11) Ferapontova, E. E.; Olsen, E. M.; Gothelf, K. V. An RNA Aptamer-Based Electrochemical Biosensor for Detection of Theophylline in Serum. *J. Am. Chem. Soc.* **2008**, *130* (13), 4256–4258.

(12) Zayats, M.; Huang, Y.; Gill, R.; Ma, C.; Willner, I. Label-Free and Reagentless Aptamer-Based Sensors for Small Molecules. *J. Am. Chem. Soc.* **2006**, *128* (42), 13666–13667.

(13) Zuo, X.; Song, S.; Zhang, J.; Pan, D.; Wang, L.; Fan, C. A Target-Responsive Electrochemical Aptamer Switch (TREAS) for Reagentless Detection of Nanomolar ATP. *J. Am. Chem. Soc.* **2007**, *129* (5), 1042–1043.

(14) Feagin, T. A.; Maganzini, N.; Soh, H. T. Strategies for Creating Structure-Switching Aptamers. *ACS Sens.* **2018**, *3* (9), 1611–1615.

(15) J. White, R.; A. Rowe, A.; W. Plaxco, K. Re-Engineering Aptamers to Support Reagentless, Self-Reporting Electrochemical Sensors. *Analyst* **2010**, *135* (3), 589–594.

(16) Huizenga, D. E.; Szostak, J. W. A DNA Aptamer That Binds Adenosine and ATP. *Biochemistry* **1995**, *34* (2), 656–665.

(17) Stojanovic, M. N.; de Prada, P.; Landry, D. W. Fluorescent Sensors Based on Aptamer Self-Assembly. *J. Am. Chem. Soc.* **2000**, *122* (46), 11547–11548.

(18) Schoukroun-Barnes, L. R.; Wagan, S.; White, R. J. Enhancing the Analytical Performance of Electrochemical RNA Aptamer-Based Sensors for Sensitive Detection of Aminoglycoside Antibiotics. *Anal. Chem.* **2014**, *86* (2), 1131–1137.

(19) Kelly, J. A.; Feigon, J.; Yeates, T. O. Reconciliation of the X-Ray and NMR Structures of the Thrombin-Binding Aptamer d(GGTTGGTGTGGTTGG). *Journal of Molecular Biology* **1996**, *256* (3), 417–422.

(20) Choi, S.-J.; Ban, C. Crystal Structure of a DNA Aptamer Bound to *Pv*LDH Elucidates Novel Single-Stranded DNA Structural Elements for Folding and Recognition. *Scientific Reports* **2016**, *6*, 34998.

(21) Das, K.; Balzarini, J.; Miller, M. T.; Maguire, A. R.; DeStefano, J. J.; Arnold, E. Conformational States of HIV-1 Reverse Transcriptase for Nucleotide Incorporation vs Pyrophosphorolysis—Binding of Foscarnet. *ACS Chem. Biol.* **2016**, *11* (8), 2158–2164.

(22) Huang, R.-H.; Fremont, D. H.; Diener, J. L.; Schaub, R. G.; Sadler, J. E. A Structural Explanation for the Antithrombotic Activity of ARC1172, a DNA Aptamer That Binds von Willebrand Factor Domain A1. *Structure* **2009**, *17* (11), 1476–1484.

(23) Russo Krauss, I.; Merlino, A.; Randazzo, A.; Novellino, E.; Mazzarella, L.; Sica, F. High-Resolution Structures of Two Complexes between Thrombin and Thrombin-Binding Aptamer Shed Light on the Role of Cations in the Aptamer Inhibitory Activity. *Nucleic Acids Res* **2012**, *40* (16), 8119–8128.

(24) Kato, K.; Ikeda, H.; Miyakawa, S.; Futakawa, S.; Nonaka, Y.; Fujiwara, M.; Okudaira, S.; Kano, K.; Aoki, J.; Morita, J.; et al. Structural Basis for Specific Inhibition of Autotaxin by a DNA Aptamer. *Nature Structural & Molecular Biology* **2016**, *23* (5), 395–401.

(25) Chi, Q.; Wang, G.; Jiang, J. The Persistence Length and Length per Base of Single-Stranded DNA Obtained from Fluorescence Correlation Spectroscopy Measurements Using Mean Field Theory. *Physica A: Statistical Mechanics and its Applications* **2013**, *392* (5), 1072–1079.

(26) Robertson, R. M.; Laib, S.; Smith, D. E. Diffusion of Isolated DNA Molecules: Dependence on Length and Topology. *PNAS* **2006**, *103* (19), 7310–7314.

(27) Uzawa, T.; Cheng, R. R.; White, R. J.; Makarov, D. E.; Plaxco, K. W. A Mechanistic Study of Electron Transfer from the Distal Termini of Electrode-Bound, Single-Stranded DNAs. *J. Am. Chem. Soc.* **2010**, *132* (45), 16120–16126.

(28) Dauphin-Ducharme, P.; Arroyo-Currás, N.; Adhikari, R.; Somerson, J.; Ortega, G.; Makarov, D. E.; Plaxco, K. W. Chain Dynamics Limit Electron Transfer from Electrode-Bound, Single-Stranded Oligonucleotides. *J. Phys. Chem. C* **2018**, *122* (37), 21441–21448.

(29) Watkins, H. M.; Vallée-Bélisle, A.; Ricci, F.; Makarov, D. E.; Plaxco, K. W. Entropic and Electrostatic Effects on the Folding Free Energy of a Surface-Attached Biomolecule: An Experimental and Theoretical Study. *J. Am. Chem. Soc.* **2012**, *134* (4), 2120–2126.

Appendix A: Real-time video analysis

```
% Code for performing real-time analysis of fluorescence in microfluidic
% channel (Chapter II)
function [dat,top_dat,time,background] = vid_analysis8(numbframe,numbroi)
close all
%Initialize Camera
delete(imaqfind);
vidobj = videoinput('hamamatsu',1,'MONO16_1344x1024');
src = getselectedsource(vidobj);
%Set initial values
set(src,'ExposureTime',0.2)
set(vidobj, 'FramesPerTrigger', 1);
set(vidobj, 'TriggerRepeat', Inf);
triggerconfig(vidobj, 'manual');

%Take a snap shot to set ROI
preview(vidobj);
rawsnap = getsnapshot(vidobj);
snap = imadjust(rawsnap);
imshow(snap);
[matrix_of_roi] = selectROImask(snap,numbroi);
backgroundroi = selectbackground(rawsnap,snap);

%Start live(-ish) video analysis
start(vidobj);
[dat,top_dat,time,background] =
analyze_frames(vidobj,matrix_of_roi,numbframe,numbroi,backgroundroi);
stop(vidobj);
end


%ROI function
function [matrix] = selectROImask(movie_frame_in,num)
%Specify Region of Interest
ROI_img = imshow(movie_frame_in);
matrix = zeros(num,4);
%Zoom in (press enter to finish zooming)
zoom on;
waitfor(gcf,'CurrentCharacter',char(13))

%Select a rectangular region (double click to select)
rec_selec = imrect;
chec = wait(rec_selec);
pos = getPosition(rec_selec);

matrix(1,1) = pos(1); %Xmin
matrix(1,2) = pos(2); %Ymin
matrix(1,3) = matrix(1,1)+pos(3); %Xmax
matrix(1,4) = matrix(1,2)+pos(4); %Ymax

for ii = 2:num
    rec_selec = imrect;
    position = wait(rec_selec);
```

```
    matrix(ii,1) = position(1); %Xmin
    matrix(ii,2) = position(2); %Ymin
    matrix(ii,3) = matrix(ii,1)+pos(3); %Xmax
    matrix(ii,4) = matrix(ii,2)+pos(4); %Ymax
    %ii = ii+1;
end
close all
end

function backbrightroi = selectbackground(~,adjusted_frame_in)
ROI_img = imshow(adjusted_frame_in);
zoom on;
waitfor(gcf,'CurrentCharacter',char(13))
backbrightroi = zeros(1,4);
%Select a rectangular region (double click to select)
rec_selec = imrect;
chec = wait(rec_selec);
pos = getPosition(rec_selec);
backbrightroi(1,1) = pos(1); %Xmin
backbrightroi(1,2) = pos(2); %Ymin
backbrightroi(1,3) = backbrightroi(1,1)+pos(3); %Xmax
backbrightroi(1,4) = backbrightroi(1,2)+pos(4); %Ymax
end


function [all_centers,radii,beads] =
o_detect_outliers(videoframe,modframe)
    %Modified version of o_detect which removes outliers and returns same
radius for all. Output includes
    %all circle detect data and the average brighness
    [centers,~] = imfindcircles(videoframe,[6
13],'ObjectPolarity','bright','Sensitivity',0.90,'Method','TwoStage');
    [centers2,~] = imfindcircles(videoframe,[6
11],'ObjectPolarity','dark','Sensitivity',0.80,'Method','TwoStage');

    %Establish coordinate grid
    [x,y]= meshgrid(1:size(modframe,2),1:size(modframe,1));

    %create array to hold bead brightness data
    all_centers = cat(1,centers,centers2);
    dimens = size(all_centers);
    numtotal = dimens(1);
    beads = zeros(1,numtotal);
    radii = zeros(1,numtotal);

    if numtotal <= 1
        beads(beads==0) = NaN;
        radii = zeros(1,numtotal) + 7;

    else

        for jj=1:numtotal;
            mask_temp = zeros(size(modframe));
            xc = all_centers(jj,1);
            yc = all_centers(jj,2);
```

```
            radii(jj) = 7;
            mask_temp = (x-xc).^2 + (y-yc).^2 < 49;
            filt = videoframe.*uint16(mask_temp);
            beads(jj) = sum(sum(filt));
        end
    end
end



function
[corrected_avgbright,corrected_topval,corrected_times,background4later] =
analyze_frames(objinput,roi_matrix,numframes,numroi,backroi)

%Reserve some memory
avgbright = zeros(numframes,1);
avgtopvalues = zeros(numframes,1);
times = zeros(numframes,1);
captionFontSize = 14;
bead_buffer = zeros(50,1);
bead_buffer(bead_buffer==0)=NaN;
background4later = zeros(numframes,1);
%Cycle through frames
ii=2;
waitfor(gcf,'CurrentCharacter',char(13))
while double(get(gcf,'CurrentCharacter'))~=27
 tic
    %Filter out everything but ROI and find the edges
    trigger(objinput);
    big_img = getdata(objinput);
    ymin1 = roi_matrix(1,2);
    ymax1 = roi_matrix(1,4);
    xmin1 = roi_matrix(1,1);
    xmax1 = roi_matrix(1,3);
    originalImage = big_img(ymin1:ymax1,xmin1:xmax1);
    for jj = 2:numroi
        ymin = roi_matrix(jj,2);
        ymax = roi_matrix(jj,4);
        xmin = roi_matrix(jj,1);
        xmax = roi_matrix(jj,3);
        temp_img = big_img(ymin:ymax,xmin:xmax);
        originalImage = cat(2,originalImage,temp_img);
        %jj = jj+1;
    end

    %Measure background signal for later normalization
    backymin = round(backroi(1,2));
    backymax = round(backroi(1,4));
    backxmin = round(backroi(1,1));
    backxmax = round(backroi(1,3));
    backgroundimg = big_img(backymin:backymax,backxmin:backxmax);
    backbright = mean(mean(backgroundimg));
    background_bead = pi*49*backbright;
    %backmin = background_bead-500;
    backmax = background_bead+600;
```

```
    % Create figure and show original feed
    set(gcf, 'units','normalized','outerposition',[0 0 1 1]);
    drawnow;
    subplot(2, 3, 2)
    dup = imadjust(originalImage);
    imshow(dup)
    caption = sprintf('Video feed');
    title(caption, 'FontSize', captionFontSize);
    axis image;

    subplot(2, 3, 1)
    dup2 = imadjust(big_img);
    imshow(dup2);
    caption = sprintf('Full video feed');
    title(caption, 'FontSize', captionFontSize);
    %Show masked video feed
    maskedImage = originalImage;
    subplot(2, 3, 4)
    imshow(backgroundimg)
    caption = sprintf('Background feed');
    title(caption, 'FontSize', captionFontSize);

    %Show circle detection done on masked video feed and calculate
brightness
    finaldup = maskedImage;
    subplot(2, 3, 5)
    imshow(dup)
    caption = sprintf('Analysis program');
    title(caption, 'FontSize', captionFontSize);
    [cent,radi,values] = o_detect_outliers(originalImage,finaldup);
    numbercircles = length(values);
    values = rot90(values,-1);

    if numbercircles == 0
        avgbright(ii) = NaN;
    else
        %Eliminate beads found to be within threshold value of background

        values(values<backmax) = NaN;
        backgroundIndex = find(isnan(values));
        radi(backgroundIndex) = 1;
        %Take beads found to be above background and add them to bead
        %history. If beads are found to be above 3 STD from avg history,
        %ignore for now
        bead_buffer = vertcat(bead_buffer(numbercircles:50),values);
        buffermean = nanmean(bead_buffer);
        bufferstd = nanstd(bead_buffer);
        outlierIndex = find(abs(bead_buffer-buffermean) > 3*bufferstd);
        outlierIndex = outlierIndex - 51 + numbercircles;
        actualindex = outlierIndex(outlierIndex>0);
        %values
        values(actualindex) = NaN;
        %values
        radi(actualindex) = 1;
        avgbright(ii) = nanmean(values);
        avgbright(ii) = avgbright(ii)-background_bead;
```

```
        h = viscircles(cent,radi);

        %Take top half of values (experimental...)
        numNaN = sum(isnan(values));
        numbeads = length(values) - numNaN;
        num2count = ceil(numbeads/2);
        sortedvalues = sort(values,'descend');
        topvalues = sortedvalues(1:num2count);
        avgtopvalues(ii) = mean(topvalues) - background_bead;
    end

    elapsedtime = toc;
    times(ii) = times(ii-1)+elapsedtime;
    subplot(2,3,6)
    plot(times(2:ii),avgbright(2:ii))
    background4later(ii) = background_bead;
    ii=ii+1;
end

%Shift data over one value to get rid of annoying avg_bright = 0 at t = 0
corrected_avgbright = avgbright;
corrected_topval = avgtopvalues;
corrected_topval(1) = avgtopvalues(2);
corrected_avgbright(1) = avgbright(2); %fix starting value is 0 later...
background4later(1) = background4later(2); %ditto...
corrected_times = times./60;
end
```

Appendix B: Monte-Carlo simulation of scaffold sensor

```
function [mol_weight,cur] = func_MC_dna4(yy,flexangle,protang)
%Inputs are yy    ==> number of DNA strands to simulate (usually between
50000
%                    to 100000
%           angle ==> angle in radians by which the DNA can vary from
%                     perpendicular
%
%Outputs are mol_weight ==> a string containing molecular weights
%            cur        ==> the current at each MW

disp
'=========================================================================
'
disp '                        Anchor Strand Simulation
'
disp
'=========================================================================
'


cur = zeros(1,37);
mol_weight = zeros(1,37);
%Cycle through molecular weights from 5 to 150
for uu = 1:30
    disp 'Current MW: '
    mol_weight(uu) = 5*uu
    disp 'Current current: '
    cur(uu) = MC_current_calc(yy,mol_weight(uu),flexangle,protang);
end

%Also do MW = 200 kDa and 250 kDa
disp 'Current MW: '
mol_weight(31) = 160
disp 'Current current: '
cur(31) = MC_current_calc(yy,mol_weight(31),flexangle,protang);
disp 'Current MW: '
mol_weight(32) = 170
disp 'Current current: '
cur(32) = MC_current_calc(yy,mol_weight(32),flexangle,protang);
disp 'Current MW: '
mol_weight(33) = 180
disp 'Current current: '
cur(33) = MC_current_calc(yy,mol_weight(33),flexangle,protang);
disp 'Current MW: '
mol_weight(34) = 190
disp 'Current current: '
cur(34) = MC_current_calc(yy,mol_weight(34),flexangle,protang);
disp 'Current MW: '
mol_weight(35) = 200
disp 'Current current: '
cur(35) = MC_current_calc(yy,mol_weight(35),flexangle,protang);
disp 'Current MW: '
```

```
mol_weight(36) = 225
disp 'Current current: '
cur(36) = MC_current_calc(yy,mol_weight(36),flexangle,protang);
disp 'Current MW: '
mol_weight(37) = 250
disp 'Current current: '
cur(37) = MC_current_calc(yy,mol_weight(37),flexangle,protang);

%Plot results...
plot(mol_weight,cur)
end



function avg_current = MC_current_calc(aa,MW,angle,protangle)

%Set aside some memory and define constants
Lp = 534; %Persistance length of dsDNA
num = 27; %Number of bases
beadwidth = 3.01; %ANGSSTROMS! DOUBLE CHECK VALUES!
r = beadwidth/2;
avgw = .6178; %THIS IS AVERAGE TWIST IN RADIANS
l = 3.38; %BEAD TO BEAD LENGTH (Angstroms)
kb = 1; %SUBSTITUTE BOLTZMANS CONST
T = 300; %TEMPERATURE
totalenergy = zeros(1,aa);
finalz = zeros(1,aa);
protein_location = zeros(1,aa);
probability_config = zeros(1,aa);
k_eT = zeros(1,aa);
prob_eT = zeros(1,aa);
numAA = MW/.110;
%Rg = .395*(numAA)^(0.6) + 7.257;
Rg = 7.78.*MW.^(.37);

parfor ii = 1:aa

    utracker = 0;
    wtracker = 0;

    %Give the DNA an initial position and angle due to carbon-carbon
    %bonds linking it to the surface
    shiftu = (angle)*randn;
    shiftw = 2*pi*rand;
    initialw = shiftw;
    rotate_u = [cos(shiftu),0,sin(shiftu);0,1,0;-
sin(shiftu),0,cos(shiftu)];
    rotate_w = [cos(initialw),-
sin(initialw),0;sin(initialw),cos(initialw),0;0,0,1];
    positions =
[6*sin(shiftu)*cos(shiftw),6*sin(shiftu)*sin(shiftw),6*cos(shiftu)];

    %Now calculate the actual positions of the backbone
    baseposition = [10,0,0];
    otherbase = [-10,0,0];
```

```
    corrected_base_pos = rotate_w*(rotate_u*baseposition');
    corrected_other_base = rotate_w*(rotate_u*otherbase');
    actual_base_pos = corrected_base_pos' + positions;
    actual_other_base = corrected_other_base' + positions;
    %shift_comp_w = 0;
    bendenergy = zeros(1,num-1);
    twistenergy = zeros(1,num-1);
    Uelectrostatic = zeros(1,num-1);
    %electrostaticenergy = zeros(1,num);


    %Generate positions for each of the base pairs
    for jj = 2:num
        %Choose a random bending angle and rotation angle
        rand_u = (pi/60)*randn;
        rand_w = 0;
        base_rand_w = avgw + 0.0125*avgw*randn;

        %Calculate cartesian coordinates of jjth bead in reference frame
of jj-1 bead
        rotated_ref_pos =
[l*sin(rand_u)*cos(rand_w),l*sin(rand_u)*sin(rand_w),l*cos(rand_u)];
        base_ref_pos = [10*cos(shiftw),10*sin(shiftw),0];
        comp_base_ref_pos = [10*cos(-shiftw+pi),10*sin(-shiftw+pi),0];

        %Calculate rotation matricies needed to shift n-1 bead frame to
default frame
        rotate_u = [cos(shiftu),0,sin(shiftu);0,1,0;-
sin(shiftu),0,cos(shiftu)];
        rotate_w = [cos(initialw),-
sin(initialw),0;sin(initialw),cos(initialw),0;0,0,1];

        %Apply rotation matricies to go from bead frame to default frame
        corrected_ref_pos = rotate_w*(rotate_u*rotated_ref_pos');
        corrected_base_pos = rotate_w*(rotate_u*base_ref_pos');
        corrected_comp_base = rotate_w*(rotate_u*comp_base_ref_pos');

        %And then get everything from (0,0,0) frame
        pos_previous = positions(:,:,jj-1);
%         comp_pos_previous = actual_base_pos(:,:,jj-1);
%         otherbase_previous = actual_other_base(:,:,jj-1);
        actual_pos = corrected_ref_pos' + pos_previous;
        comp_actual_pos = corrected_base_pos'+actual_pos;
        comp_base_pos = corrected_comp_base' + actual_pos;

        %Record position, twist, bend for bead jj
        positions = cat(3,positions,actual_pos);
        actual_base_pos = cat(3,actual_base_pos,comp_actual_pos);
        actual_other_base = cat(3,actual_other_base,comp_base_pos);



        %Keep track of overall shift in reference frame for next bead
        shiftu = shiftu+rand_u;
        shiftw = shiftw+base_rand_w;
```

```
        utracker(jj) = rand_u;
        wtracker(jj) = rand_w;

        %Calculate energy of bead jj in terms of kT's
        bendenergy(jj-1) = (Lp/l)*(1-cos(rand_u));
        %twistenergy(jj-1) = 0;
        twistenergy(jj-1) = 0.5*203.49*(base_rand_w-avgw)^2;
        Uelectrostatic(jj) = 0;%0.001*(38.63)*(2.053)*exp(-
comp_base_pos(3)/7)+(38.63)*(2.053)*exp(-comp_actual_pos(3)/7);
        %This is the electrostatic energy between each base and the
surface, normalized by kT, given all of the shit in
        %your lab notebook from 1/16/18 (page 26). Includes salt screening
        %for 150mM salt (i.e. 1x PBS)
    end

    %Add the protein on the end of the DNA chain. Right now we are not
    %considering bend energy or twist energy here. Note that the protein
    %position is given in the 'positions' variable and is attached to the
    %backbone

    rand_uAA = (protangle)*rand;
    rand_wAA = 0.25*avgw*randn;
    backbone_pos_previous = actual_base_pos(:,:,num);
    rotated_ref_pos =
[(l+Rg)*sin(rand_uAA)*cos(rand_wAA),(l+Rg)*sin(rand_uAA)*sin(rand_wAA),(l+
Rg)*cos(rand_uAA)];
    prot_rotate_u = [cos(shiftu),0,sin(shiftu);0,1,0;-
sin(shiftu),0,cos(shiftu)];
    prot_rotate_w = [cos(shiftw),-
sin(shiftw),0;sin(shiftw),cos(shiftw),0;0,0,1];
    prot_corrected_ref_pos =
prot_rotate_w*(prot_rotate_u*rotated_ref_pos');
    actual_pos = prot_corrected_ref_pos' + backbone_pos_previous;
    positions = cat(3,positions,actual_pos); %Access to the protein
location is in the 'positions' variable at index num+1

    %Now consider the placement of the methylene blue (which should be
    %normal to the last AA on the anchor strand and ~7 angtroms away

    uMB = pi/2;
    wAA = 0;
    MB_pos_previous = actual_other_base(:,:,num);
    rotated_ref_pos =
[7*sin(uMB)*cos(wAA),7*sin(uMB)*sin(wAA),7*cos(uMB)];
    rotate_u = [cos(shiftu),0,sin(shiftu);0,1,0;-
sin(shiftu),0,cos(shiftu)];
    rotate_w = [cos(shiftw),-
sin(shiftw),0;sin(shiftw),cos(shiftw),0;0,0,1];
    corrected_ref_pos = rotate_w*(rotate_u*rotated_ref_pos');
    actual_pos = corrected_ref_pos' + MB_pos_previous;
    positions = cat(3,positions,actual_pos); %Access to the MB location is
in the 'positions' variable at index num+2

     x = positions(:,1,:,:);
     y = positions(:,2,:,:);
     z = positions(:,3,:,:);
```

```
     zz = z(num+1); %This is z-location of protein


     %Check to see if the protein is in contact with the monolayer and
     %calculate energies
     if zz<(Rg+9.24) %9.24 is approx the length of mercaptohexanol in
Angstroms
         totalenergy(ii) = NaN;
         finalz(ii)= z(num);
         zMB = z(num+2);
         protein_location(ii) = zz;
         probability_config(ii) = 0;
         k_eT(ii) = NaN;
     else
        totalenergy(ii) = sum(bendenergy) + sum(twistenergy);
        finalz(ii) = z(num);
        zMB = z(num+2);
        if zMB<9.25
            zMB = 9.25;
        end
        protein_location(ii) = zz;
        probability_config(ii) = exp(-totalenergy(ii));
        k_eT(ii) = 4400*(exp(-(zMB-9.24)*(1.2)));
     end
end

%Go through and normalize the probability function
totalprob = sum(probability_config);
normal_prob = probability_config./totalprob;


%for each configuration, find the probability of electron transfer

for zzz = 1:aa
    prob_eT(zzz) = k_eT(zzz)*normal_prob(zzz);
end
avg_current = nansum(prob_eT);
end
```

Appendix C: Monte-Carlo simulation of aptamer-based sensors

```
%Function to calculate electron transfer rate of ssDNA
function [keT_observed,count_yes,MBpos,keT,positions,delE_average_history]
= MCss_DNA_3(nsteps,lengthDNA)
count_yes = 0;
count_no = 0;
T = 300; %Temp in kelvin
Lb = .676; %length per base in nanometers of ssDNA
Lp = 2.223; %persistence length of ssDNA in nm
MBpos = zeros(nsteps,1);
keT = zeros(nsteps,1);
magnitude_bend_shift = 1;
magnitude_twist_shift = 1;
delE_average_history = zeros(1,nsteps);
time = 0;
electrons_transfered = 0;
diff_const = (3.096e8)*(lengthDNA)^(-.571); % nm^2/s taken from Lukacs et
                                            % al J. Bio. Chem. 1999
(initial value) and Robertson
                                            % et al. PNAS 2006 (for the
                                            % length dependence)

%Create initial ssDNA complex standing straight up
delE_history = [];


xpos = zeros(lengthDNA,1);
ypos = zeros(lengthDNA,1);
zpos = zeros(lengthDNA,1);

for jj = 1:lengthDNA
    zpos(jj) = jj*Lb;
end
bend = zeros(lengthDNA,1);
twist = zeros(lengthDNA,1);

%start changing the structure
positions = [xpos,ypos,zpos];

for kk = 1:nsteps
    pos_old = positions(lengthDNA,:);
    delE_total  = 0;
    for ll = 1:lengthDNA

        %Choose random bend/twist
        delta_rand_bend = (randn-.5)*magnitude_bend_shift;
        delta_rand_twist = 2*pi*rand-pi; %Changed to be FJC model...
        %delta_rand_twist = (randn-.5)*magnitude_twist_shift;
        bend_temp = bend;
        twist_temp = twist;
        bend_temp(ll) = bend(ll) + delta_rand_bend;
        twist_temp(ll) = twist(ll) + delta_rand_twist;
```

```
        temppositions =
update_position2(lengthDNA,Lb,positions,bend_temp,twist_temp,ll);
        count_while = 0;
        %Check if everything is above z = 0 plane, update if not
        while all(temppositions(:,3)>0)==0
            count_while = count_while+1;
            temppositions(:,3);
            delta_rand_bend = 0.9*delta_rand_bend;
            delta_rand_twist = 0.9*delta_rand_twist;
            bend_temp(ll) = bend(ll) + delta_rand_bend;
            twist_temp(ll) = twist(ll) + delta_rand_twist;
            temppositions =
update_position2(lengthDNA,Lb,positions,bend_temp,twist_temp,ll);
            if count_while > 1000
                delta_rand_bend
                delta_rand_twist
                ll
                kk
                positions
                temppositions
                'While-loop is stuck'
                return
            end

        end

        'done!';
        %Calculate internal bend energy
        del_E_bend = -(Lp/Lb)*(1-cos(bend(ll))) + (Lp/Lb)*(1-
cos(bend_temp(ll)));
        del_E_twist = 0;
        del_E = del_E_bend + del_E_twist;

        %Depending on the energy, update bend/twist
        if del_E < 0 ||  exp(-del_E) > rand

            deltaU_electro = calc_electrostatics(positions,temppositions,-
.25);

                if deltaU_electro < 0 ||  exp(-deltaU_electro) > rand
                    positions = temppositions;
                    twist = twist_temp;
                    bend = bend_temp;
                    delE_total = delE_total + deltaU_electro;
                    'yes';
                    count_yes = count_yes + 1;
                else
                    'no; electrostatics';
                    count_no = count_no +1;
                end

        else
            count_no = count_no +1;

            'no'   ;
```

```
        end

        delE_total = delE_total + del_E;
%             xpos = positions(:,1);
%             ypos = positions(:,2);
        zpos = positions(:,3);
%             figure
%             plot3(xpos,ypos,zpos)
    end

    pos_new = positions(lengthDNA,:);
    diff_dist = norm(pos_old.^2 - pos_new.^2);
    timestep = (diff_dist^2)/(6*diff_const);

    delE_history = [delE_history, delE_total];
    time = time+timestep;
    zMB = positions(lengthDNA,3);
    MBpos(kk) = zMB;
    keT(kk) = 4400*(exp(-(zMB)*(1.2)));
    prob_eT = keT(kk)*timestep;

    %Determine if electron transfer happens
    if prob_eT > rand
        electrons_transfered = electrons_transfered+1
        time
        kk
        'rate (Hz)'
        electrons_transfered/time
        if electrons_transfered > 100
            keT_observed = electrons_transfered/time;
            return
        end
    end


end
%Take z pos of final base and use to calculate keT

keT_observed = electrons_transfered/time;
delE_average_history = delE_average_history + delE_history;
delE_average_history = delE_average_history./(lengthDNA);
%  count_yes
%  count_no




%Function to calculate electron transfer rate of bound-state aptamer
function [keT_observed,count_yes,MBpos,keT,positions] =
MC_aptamer2(nsteps,length_stem,length_tail)
count_yes = 0;
count_no = 0;
T = 300; %Temp in kelvin
```

```
Lb = .676; %length per base in nanometers of ssDNA
Lp = 2.223; %persistence length of ssDNA in nm
MBpos = zeros(nsteps,1);
keT = zeros(nsteps,1);
magnitude_bend_shift = 1;
magnitude_twist_shift = 1;
delE_average_history = zeros(1,nsteps);
time = 0;
electrons_transfered = 0;
lengthDNA = length_stem+length_tail;
diff_const = 2*(((3.096e8)*(lengthDNA)^(-.6))^(-1) + (1.2e8)^(-1))^(-1); %
nm^2/s taken from Lukacs et
                                            % al J. Bio. Chem. 1999
(initial value) and Robertson
                                            % et al. PNAS 2006 (for the
                                            % length dependence) VALUE IS
-.571

temp_top_pos = [0,0,(length_tail+4)*Lb];
time_old = 0;
%Create initial ssDNA complex standing straight up
delE_history = [];
xpos = zeros(lengthDNA,1);
ypos = zeros(lengthDNA,1);
zpos = zeros(lengthDNA,1);

for jj = 1:length_stem
    zpos(jj) = jj*Lb;
end

for jj = 1:length_tail
    ind = length_stem+jj;
    zpos(ind) = zpos(length_stem) - (jj-1)*Lb;
    xpos(ind) = 2;
end

bend = zeros(lengthDNA,1);
twist = zeros(lengthDNA,1);

%start changing the structure
positions = [xpos,ypos,zpos];
kk = 0;

%This keeps the code from taking forever to run but returns slightly
%noisier data...
if lengthDNA < 6
    max_electrons = 100;
elseif lengthDNA < 10
    max_electrons = 75;
elseif lengthDNA < 14
    max_electrons = 50;
else
    max_electrons = 30;
end
```

```
%Main loop
while electrons_transfered < max_electrons
    kk = kk+1;
    pos_old = positions(lengthDNA,:);
    pos_old_top = temp_top_pos;
    delE_total  = 0;
    for ll = 1:lengthDNA

        %Choose random bend/twist
        delta_rand_bend = (randn-.5)*magnitude_bend_shift;
        delta_rand_twist = 2*pi*(rand-.5);
        %delta_rand_twist = (randn-.5)*magnitude_twist_shift;

        bend_temp = bend;
        twist_temp = twist;
        bend_temp(ll) = bend(ll) + delta_rand_bend;
        twist_temp(ll) = twist(ll) + delta_rand_twist;

        [temppositions,temp_top_pos] =
update_position_aptamer(length_stem,length_tail,Lb,positions,bend_temp,twi
st_temp,ll);
        count_while = 0;
        %Check if everything is above z = 0 plane, update if not
        while all(temppositions(:,3)>0)==0
            count_while = count_while+1;
            temppositions(:,3);
            delta_rand_bend = 0.9*delta_rand_bend;
            delta_rand_twist = 0.9*delta_rand_twist;
            bend_temp(ll) = bend(ll) + delta_rand_bend;
            twist_temp(ll) = twist(ll) + delta_rand_twist;
            [temppositions,temp_top_pos] =
update_position_aptamer(length_stem,length_tail,Lb,positions,bend_temp,twi
st_temp,ll);
        end

        'done!';
        %Calculate internal bend energy
        del_E_bend = -(Lp/Lb)*(1-cos(bend(ll))) + (Lp/Lb)*(1-
cos(bend_temp(ll)));
%         del_E_twist = 0;
        del_E = del_E_bend;

        %Depending on the energy, update bend/twist
        if del_E < 0 ||  exp(-del_E) > rand

            deltaU_electro = calc_electrostatics(positions,temppositions,-
.35);

                if deltaU_electro < 0 ||  exp(-deltaU_electro) > rand
                    positions = temppositions;
                    twist = twist_temp;
                    bend = bend_temp;
                    delE_total = delE_total + deltaU_electro;
                    'yes';
                    count_yes = count_yes + 1;
```

```
                else
                    'no; electrostatics';
                    count_no = count_no +1;
                end

            else
                count_no = count_no +1;

                'no'    ;

            end

            delE_total = delE_total + del_E;
%               xpos = positions(:,1);
%               ypos = positions(:,2);
            zpos = positions(:,3);
%               figure
%               plot3(xpos,ypos,zpos)
        end

        pos_new = positions(lengthDNA,:);
        top_pos_new = temp_top_pos;

        diff_dist_top = norm(top_pos_new.^2 - pos_old_top.^2);
        diff_dist = norm(pos_old.^2 - pos_new.^2);

        max_diff_dist = max([diff_dist, diff_dist_top]);
        timestep = (max_diff_dist^2)/(6*diff_const);

        delE_history = [delE_history, delE_total];
        time = time+timestep;
        zMB = positions(lengthDNA,3);
        MBpos(kk) = zMB;
        keT(kk) = 4400*(exp(-(zMB)*(1.2)));
        prob_eT = keT(kk)*timestep;

        %Determine if electron transfer happens
        if prob_eT > rand
            time_new = time;
            time_diff = time_new-time_old;
            if time_diff>.0005
                electrons_transfered = electrons_transfered+1
                time
                time_diff
                kk
                'rate (Hz)'
                electrons_transfered/time
                time_old = time_new;
            end
            if electrons_transfered > 100
                keT_observed = electrons_transfered/time;
                return
            end
        end
```

```
end
%Take z pos of final base and use to calculate keT

keT_observed = electrons_transfered/time;
%delE_average_history = delE_average_history + delE_history;
%delE_average_history = delE_average_history./(lengthDNA);
%  count_yes
%  count_no




%function to calculate electrostatic effects
function deltaU =
calc_electrostatics(positions_before,positions_after,voltage)
%Testing GitHub updates with this comment. Please ignore...
q_star = 38.92; % q/kT in Volts^-1 at 25 Celcius
z_before = positions_before(:,3);
z_after = positions_after(:,3);
num_bases = length(z_before);
u_before = zeros(1,num_bases);
u_after = zeros(1,num_bases);

%Here we model the voltage as an exponential decay with a debye length of
%.785 nm, equivalent to that of a 150 mM electrolyte solution (i.e. 1xPBS
solution)
for ii = 1:num_bases
    u_before(ii) = -voltage*q_star*exp(-z_before(ii)/.785);
    u_after(ii) = -voltage*q_star*exp(-z_after(ii)/.785);
end

deltaU = sum(u_after)-sum(u_before);
% deltaU = 0.1*deltaU;




%Function handling position updates for bound state aptamer
function [positions,temp_position] =
update_position_aptamer(length_stem,length_tail,Lb,positions,bend_temp,twi
st_temp,ll)
lengthDNA = length_stem+length_tail;

if ll > length_stem
    ll = length_stem;
end

if ll <= length_stem
    %Calculate positions of the stem bases first
    for ii = ll:length_stem

        if ii == 1
            position_last = [0,0,0];
```

```
        else
            position_last = positions(ii-1,:);
        end

        current_bend = bend_temp(ii);
        current_twist = twist_temp(ii);

        shiftu = sum(bend_temp(1:ii)) - current_bend;
        shiftw = sum(twist_temp(1:ii)) - current_twist;

        rotated_ref_pos =
[Lb*sin(current_bend)*cos(current_twist),Lb*sin(current_bend)*sin(current_
twist),Lb*cos(current_bend)];
        rotate_u = [cos(shiftu),0,sin(shiftu);0,1,0;-
sin(shiftu),0,cos(shiftu)];
        rotate_w = [cos(shiftw),-
sin(shiftw),0;sin(shiftw),cos(shiftw),0;0,0,1];
        corrected_base_pos = rotate_w*(rotate_u*rotated_ref_pos');

        positions(ii,:) = position_last + corrected_base_pos';
        position_last = positions(ii,:);
    end

    %Calculate the position of the last complementary base
    shiftufinal = sum(bend_temp(1:length_stem));
    shiftwfinal = sum(twist_temp(1:length_stem));
    comp_transformation = [2*cos(shiftufinal), 2*sin(shiftwfinal), 0];
    rotate_u = [cos(shiftufinal),0,sin(shiftufinal);0,1,0;-
sin(shiftufinal),0,cos(shiftufinal)];
    rotate_w = [cos(shiftwfinal),-
sin(shiftwfinal),0;sin(shiftwfinal),cos(shiftwfinal),0;0,0,1];
    corrected_comp = rotate_w*(rotate_u*comp_transformation');
    positions(length_stem+1,:) = positions(length_stem,:) +
corrected_comp';
    positions_last = positions(length_stem+1,:);

    %calculate the position of the top-most complementary base (assuming 5
    %total complementary bases)
    rotated_ref_pos =
[12*Lb*sin(current_bend)*cos(current_twist),12*Lb*sin(current_bend)*sin(cu
rrent_twist),12*Lb*cos(current_bend)];
    rotate_u = [cos(shiftu),0,sin(shiftu);0,1,0;-
sin(shiftu),0,cos(shiftu)];
    rotate_w = [cos(shiftw),-
sin(shiftw),0;sin(shiftw),cos(shiftw),0;0,0,1];
    corrected_base_pos = rotate_w*(rotate_u*rotated_ref_pos');
    temp_position = positions(length_stem,:) + corrected_base_pos';

    %Calculate positions of the tail bases
    for mm = 2:length_tail
        index = length_stem + mm;
        current_bend = bend_temp(index);
        current_twist = twist_temp(index);
```

```
        shiftu = shiftufinal - sum(bend_temp(length_stem+1:index)) +
current_bend;
        shiftw = shiftwfinal - sum(twist_temp(length_stem+1:index)) +
current_twist;

        rotated_ref_pos =
[Lb*sin(current_bend)*cos(current_twist),Lb*sin(current_bend)*sin(current_
twist),Lb*cos(current_bend)];
        rotate_u = [cos(shiftu),0,sin(shiftu);0,1,0;-
sin(shiftu),0,cos(shiftu)];
        rotate_w = [cos(shiftw),-
sin(shiftw),0;sin(shiftw),cos(shiftw),0;0,0,1];
        corrected_base_pos = rotate_w*(rotate_u*rotated_ref_pos');

        positions(index,:) = positions_last - corrected_base_pos';
        positions_last = positions(index,:);
    end
%if ll starts after the complementary base, there is no need to calculate
stem base positions
elseif ll == length_stem+1
    shiftufinal = sum(bend_temp(1:length_stem));
    shiftwfinal = sum(twist_temp(1:length_stem));
    comp_transformation = [2*cos(shiftufinal), 2*sin(shiftwfinal), 0];
    rotate_u = [cos(shiftufinal),0,sin(shiftufinal);0,1,0;-
sin(shiftufinal),0,cos(shiftufinal)];
    rotate_w = [cos(shiftwfinal),-
sin(shiftwfinal),0;sin(shiftwfinal),cos(shiftwfinal),0;0,0,1];
    corrected_comp = rotate_w*(rotate_u*comp_transformation');
    positions(length_stem+1,:) = positions(length_stem,:) +
corrected_comp';
    positions_last = positions(length_stem+1,:);

    %Calculate positions of the tail bases
    for mm = 2:length_tail
        index = length_stem + mm;
        current_bend = bend_temp(index);
        current_twist = twist_temp(index);

        shiftu = shiftufinal - sum(bend_temp(length_stem+1:index)) +
current_bend;
        shiftw = shiftwfinal - sum(twist_temp(length_stem+1:index)) +
current_twist;

        rotated_ref_pos =
[Lb*sin(current_bend)*cos(current_twist),Lb*sin(current_bend)*sin(current_
twist),Lb*cos(current_bend)];
        rotate_u = [cos(shiftu),0,sin(shiftu);0,1,0;-
sin(shiftu),0,cos(shiftu)];
        rotate_w = [cos(shiftw),-
sin(shiftw),0;sin(shiftw),cos(shiftw),0;0,0,1];
        corrected_base_pos = rotate_w*(rotate_u*rotated_ref_pos');

        positions(index,:) = positions_last - corrected_base_pos';
        positions_last = positions(index,:);
    end
else
```

```
    shiftufinal = sum(bend_temp(1:length_stem));
    shiftwfinal = sum(twist_temp(1:length_stem));
        %Calculate positions of the tail bases
    for nn = ll:length_tail

        index = length_stem + nn;
        positions_last = positions(index-1,:);
        current_bend = bend_temp(index);
        current_twist = twist_temp(index);

        shiftu = shiftufinal - sum(bend_temp(length_stem+1:index)) +
current_bend;
        shiftw = shiftwfinal - sum(twist_temp(length_stem+1:index)) +
current_twist;

        rotated_ref_pos =
[Lb*sin(current_bend)*cos(current_twist),Lb*sin(current_bend)*sin(current_
twist),Lb*cos(current_bend)];
        rotate_u = [cos(shiftu),0,sin(shiftu);0,1,0;-
sin(shiftu),0,cos(shiftu)];
        rotate_w = [cos(shiftw),-
sin(shiftw),0;sin(shiftw),cos(shiftw),0;0,0,1];
        corrected_base_pos = rotate_w*(rotate_u*rotated_ref_pos');

        positions(index,:) = positions_last - corrected_base_pos';
    end
end
```